ABSTRACT

Title of Dissertation: SIGNATURE OF MAJORANA MODES AND ASPECTS OF THEIR BRAIDING

Amit Nag, Doctor of Philosophy, 2018

Dissertation Advisor: Professor Jay Deep Sau

Department of Physics

Majorana zero modes are emergent zero-energy quasiparticle excitations in certain superconducting systems that can be viewed as fractionalized or “half” electrons. These quasiparticles obey non-Abelian braiding statistics which is one manifestation of such half-electron character. Due to such non-Abelian braiding property, Majorana zero mode pairs hold promise as potential qubits for topological quantum computation.

It is somewhat surprising that, at least theoretically, ordinary one-dimensional semiconductor systems can be induced to host such esoteric Majorana modes as edge states if some precise experimental conditions are satisfied. Because of the relative simplicity of material and experimental requirements to host Majorana modes, there has been a flurry of experimental effort to realize them in semiconductor nanowire systems. While experimental efforts have produced preliminary evidence for the presence of Majorana zero modes in these systems, a thorough confirmation is lacking. The experimental signature in question is the presence of a zero-bias conductance-peak that, while necessary, is not a sufficient criteria to establish presence of underlying Majorana modes. Given

the importance of Majorana braiding for topological quantum computation and skepticism over presence of Majorana modes in these experimental systems, it would seem natural to attempt braiding these putative Majorana modes in the near future. In that case an observation of non-Abelian statistics would provide the necessary and sufficient condition in favor of Majorana presence in the studied experimental systems.

This thesis has three distinct parts. First we assume perfect Majorana modes as given that can be successfully braided. In this case, we calculate the diabatic error due to finite speed of braiding when the system is coupled to a Bosonic bath. Next, we grant that the mechanism for zero-bias conductance-peak is indeed topological, albeit the underlying Majorana modes may be imperfect (the modes are not precisely at zero energy). We study the interplay of dissipation and finite energy splitting of the Majorana modes and study its consequence regarding the probability of successful braiding. Lastly, we propose studying correlation between independent left and right conductance measurements as a means to distinguish between a topological versus a non-topological mechanism underlying the observed zero-bias conductance-peak.

SIGNATURE OF MAJORANA MODES AND ASPECTS OF THEIR BRAIDING

by

Amit Nag

Dissertation submitted to the Faculty of the Graduate School of the
University of Maryland, College Park in partial fulfillment
of the requirements for the degree of
Doctor of Philosophy
2018

Advisory Committee:
Assistant Professor Jay Deep Sau, Chair
Assistant Professor Maissam Barkeshli
Professor Theodore L. Einstein
Associate Professor Mohammad Hafezi
Professor Christopher Jarzynski

Acknowledgments

First and foremost I would like to thank Professor Jay Deep Sau for constant encouragement and support over the last five years. He has been a very patient advisor who has never got tired of answering the silliest of questions. He has an inimitable knack to reduce the most complicated and esoteric ideas and calculations to simple symmetry arguments and, more often than not, to Fermi's golden rule. On top of that me and my fellow CMTC grads were often astounded how accurately close his quick sketch of a calculation came to the same calculation us grad students would painstakingly carry out over an order of magnitude greater time. I will always cherish my association with him.

I would also like to thank all my other collaborators on various research projects, Professor Sankar Das Sarma, Bitan, Yahya, David and Will. I was fortunate to attend some wonderful courses here at Maryland, the highlight being Prof. Jarzynski's course on non-equilibrium statistical mechanics. Like everyone else in his class, I have admired his clarity of thought and his lucid presentation. Without exaggeration, his class was the best physics course I have ever taken. I am fortunate to have him on the thesis committee.

Over these past years my parents and Juhi have been a steadfast support through ups and downs and this thesis would not have been possible without them. Other than them, there have been simply too many people who have helped and have positively influenced me as friends. Their help and support can not be reduced to a simple token of acknowledgement in a long list of names. All I can say is that I am indebted to all my friends who extended their support while I have tried to adjust to a new life in a different country.

Table of Contents

List of Figures

Abbreviations

BCS	**B**ardeen **C**ooper **S**chrieffer
BdG	**B**ogoliubov **de**-**G**ennes
MZM	**M**ajorana **Z**ero **M**ode
ZBCP	**Z**ero **B**ias **C**onductance **P**eak
LDOS	**L**ocal **D**ensity **O**f **S**tates
BTK	**B**londer **T**inkham **K**lapwijk
NS	**N**ormal-lead **S**uperconductor
TPT	**T**opological **P**hase **T**ransition
PH	**P**article **H**ole
CC	**C**onductance **C**orrelation
ZBPC	**Z**ero **B**ias **P**eak **C**orrelation
TV	**T**opological **V**isibility
TI	**T**opological **I**nvariant

List of Publications

This dissertation is based on two yet unpublished works and the following publication:

1. S Das Sarma, Amit Nag, and Jay D Sau. How to infer non-abelian statistics and topological visibility from tunneling conductance properties of realistic majorana nanowires. Physical Review B, 94(3):035143 (2016).
2. Amit Nag and Jay D Sau. Diabatic errors in Majorana braiding. arXiv:1808.09939 (2018).

Other publication I contributed to:

1. Y. Alavirad, D. Clarke, A. Nag, and J. D. Sau. $\mathbb{Z}_3$ Parafermionic Zero Modes without Andreev Backscattering from the $2/3$ Fractional Quantum Hall State Phys. Rev. Lett. 119, 217701 (2017).

Chapter 1: Introduction

1.1 Majorana Zero Modes

In 1937, in a seminal paper Ettore Majorana introduced the eponymous Majorana equation which describes spin-1/2 charge-neutral relativistic fermions [1]. Essentially, the Majorana equation is a real representation of the Dirac equation and hence admit purely real solutions. Particles described by such purely real solutions are dubbed as 'Majorana fermions'. Since particle and anti-particle wavefunctions are related by complex conjugation, Majorana fermions are said to be its own anti-particle. However, no such elementary particle has been discovered that can be described as a Majorana fermion with certainty. Within the family of all the fermions present in the Standard Model, neutrino remains the only possible candidate that may or may not be a Majorana particle. However beyond Standard Model, the supersymmetric framework requires Majorana fermions as super-partners to spin-0 or spin-1 Bosonic fields. Thus, the search for elementary Majorana fermions is likely to continue within the realm of experimental high-energy physics for conceivable future. More in-depth discussion on Majorana fermions from high-energy physics perspective can be found in Refs. [2, 3].

While the search for mentary Majorana particle remains elusive, the potential to realize an emergent quasiparticle excitation that behaves as a Majorana fermion, in condensed matter systems have generated great excitement in the field in roughly the last 20 years. Majorana quasiparticle excitation often dubbed as 'Majorana Mode' is an emergent quasiparticle state that is a linear supersposition of a particle and a hole excitation. Early pioneering work [4–9], theoretically established the existence of such Majorana modes in various model systems. A unifying property in all such model systems is the existence of *p-wave* pairing that leads to a ground state described by a condensate such as in superconductors and superfluids. To see why superconductors provide an unique laboratory to explore Majoranas, recall that in the mean-field BCS theory of superconductivity, a quasiparticle excitation (say of energy, $E > 0$) is a coherent superposition of particle and hole excitations that in general have the form

$$\gamma_E = \sum_p u_p^E c_p + v_p^E c_p^\dagger, \tag{1.1}$$

where all the degrees of freedom such as spin, spatial etc are subsumed in the subscript p. However, particle-hole symmetry manifest in BCS theory guarantees for every positive energy quasiparticle operator one can always find its negative energy partner γ_{-E} that satisfies,

$$\gamma_E^\dagger = \gamma_{-E}. \tag{1.2}$$

A zero energy excitation described by $\gamma_{E=0} = \gamma_{E=0}^\dagger$ is Hermitian and thus can be viewed as a Majorana mode because such quasiparticle is its own "anti-quaisparticle". Hence the study of Majorana modes is essentially equivalent to the study of zero-energy quasiparticle states of superconductors. We now present more precise arguments demonstrating the emergence of such Majorana modes in one-dimensional superconductors.

1.2 Majorana modes in 1D ideal model systems

1.2.1 A heuristic argument for existence of Majorana modes

Before presenting a more structured argument for existence of Majorana modes in a superconductor, let us indulge in a slightly imprecise but an extremely simple argument

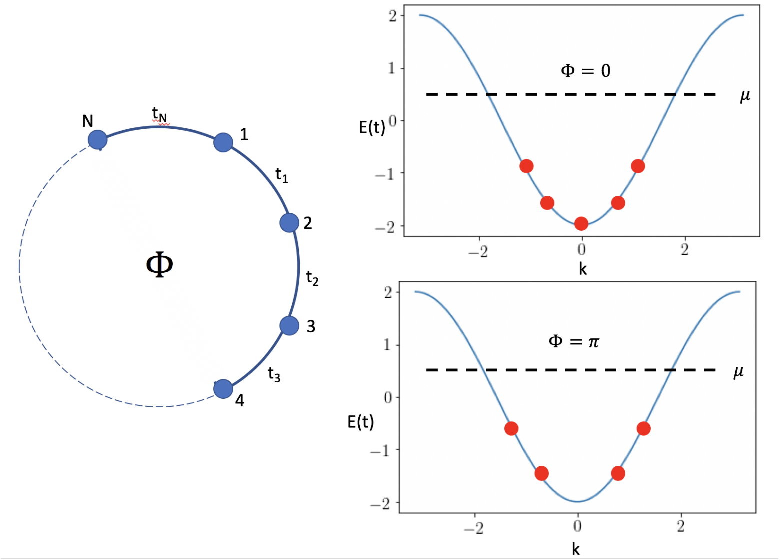

FIGURE 1.1: (Left) A schematic representation of N-site one dimensional chain looped around magnetic flux Φ.The chain is described by the Hamiltonian in Eq. 1.3 where the nearest neighbor hopping amplitudes are represented by t_i's. (Top Right) A schematic plot of band structure restricted to the Brillouin zone for zero magnetic flux. The band is partially filled upto the chemical potential denoted by μ. First few low-energy k states are denoted by solid red discs. (Bottom Left) Same as above but magnetic flux being $\Phi = \pi$. Again, first few low-energy k states are denoted by solid red discs. Note that ground state parity is odd for $\Phi = 0$ versus being even for $\Phi = \pi$.

that points towards existence of Majorana modes in one-dimensional single-band superconductors. Consider a one dimensional chain modeled by a tight-binding Hamiltonian,

$$H_{1D} = -t_n \sum_n c^\dagger_{n+1} c_n + H.c. \tag{1.3}$$

We close this chain in a loop and introduce a magnetic flux Φ (in units of flux quantum h/e) through the loop as shown in Fig. 1.1 (left panel). Assuming a uniform hopping amplitude $t_n = t$ for all n, we solve this system for $\Phi = 0$ and $\Phi = \pi$. For both cases $\Phi = 0, \pi$, the eigenvalues E_k are given by $E_k = -2t\cos(k)$, however, the two cases differ in allowed values k,

$$k = \begin{cases} 2n\frac{\pi}{N} & \text{if } \Phi = 0 \\ (2n+1)\frac{\pi}{N} & \text{if } \Phi = \pi \end{cases} \qquad n \in \{0, \dots N-1\}. \tag{1.4}$$

Restricting the Brillouin zone to $[-\pi, \pi)$, the electronic band defined by E_k is shown in Fig. 1.1 (right panel). If the band is partially filled (i.e. the chemical potential μ lies in the range $-2t < \mu < 2t$), in the ground state, the total number of single-particle occupied states for $\Phi = 0$ ($\Phi = \pi$) is odd (even) as shown in Fig. 1.1 (right panel). This is a simple consequence of $k = 0$ being allowed (disallowed) for $\Phi = 0$ ($\Phi = \pi$) in the spectrum. We say the ground state has odd (even) parity when an odd (even) number of states are occupied. A superconducting term of the form $\Delta \sum_n c_n^\dagger c_{n+1}^\dagger + H.c.$ added to the Hamiltonian in Eq. 1.3 does not change this observation, i.e. the change of ground state parity from odd to even upon flux insertion of π holds because parity is a good quantum number even in presence of superconductivity. However, crucially, the superconductivity term introduces a gap in the spectrum at energy $E = \mu$. The flux Φ can be introduced in a tight-binding Hamiltonian by a transformation $t_N \to t_N e^{i\Phi}$. Therefore, $t_N \to -t_N$) as flux $\Phi = 0 \to \pi$). Now we can imagine t_N being relatively weak with respect to the bulk hopping amplitude t, $t_N/t \to 0$. While in doing so we explicitly break translation invariance, let us overlook such technical subtlety for the time-being. All we have done by making t_N relatively weak compared to the bulk hopping is to ensure that the parity change that follows as $t_N \to -t_N$ (which is equivalent to flux insertion of π) must be caused entirely by the modes at sites 1 and N respectively. Let us call these boundary modes. We now show that such boundary modes can not be Fermionic in nature.

To facilitate a parity change there must be a state that crosses the chemical potential as the infinitesimal amplitude changes sign, $t_N \to -t_N$. Now we analyze the superconducting Hamiltonian in the first-quantized Bogoliubov-DeGennes (BdG) picture. The zero energy in the BdG picture corresponds to the chemical potential. Furthermore, corresponding to each excitation in the second-quantized Hamiltonian, there is a pair of modes related by the particle-hole symmetry in the BdG picture. The state that crosses the chemical potential corresponds to a pair of BdG modes with energy $\pm\delta$ where δ must be infinitesimal on the account of t_N being infinitesimal. Moreover, since this pair of modes exist in the superconducting gap, their wavefunctions must be localized. Precisely at $t_N = 0$, there must be two zero-energy modes in the system and there are two possibilities, either one mode is localized at each end of the wire or both modes are localized at an end. Let us denote the ground state when $t_N = 0$ by $|G\rangle$. For small but finite t_N it follows from first-order perturbation, $\langle G|t_N(c_1^\dagger c_N + H.c.)|G\rangle \approx \delta$. To ensure this finite correction to zero-energy upon switching a finite hopping amplitude t_N between the 1^{st} and the N^{th} site, there must be one mode localized at each of the open chain when $t_N = 0$. From particle-hole symmetry it follows that a non-degenerate end-state, zero-energy mode must be a Majorana mode. Hence, a single-band superconducting chain hosts Majorana edge states, with one Majorana mode being at each end of the wire.

1.2.2 Majorana modes in spinless p-wave 1D superconductors

In this section we will use a more standard and a slightly more rigorous approach to demonstrate presence of Majorana end states in a p-wave superconductor following the original work of Kitaev [4]. Consider a clean one dimensional p-wave superconductor with the lattice Hamiltonian,

$$H = -\mu \sum_{n=1}^{N} c_n^\dagger c_n - \sum_{n=1}^{N-1} \left(t c_n^\dagger c_{n+1} + \Delta c_n c_{n+1} + \text{H.c.} \right) . \tag{1.5}$$

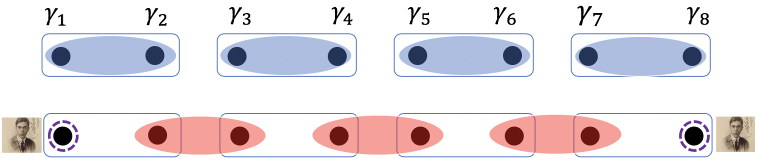

FIGURE 1.2: A schematic representation of a four site p-wave superconducting wire for open boundary condition described Eq. 1.5. (Top) The p-wave wire in the limit $\Delta = t = 0$. In this limit, Majorana pairs at each site are strongly bounded and system in a trivial state. (Bottom) The p-wave wire in the limit $\mu = 0$ and $\Delta = t$. In this limit, each Majorana mode pairs with another Majorana mode of the neighboring site, leaving a single localized Majorana mode at each end of the wire (denoted by the picture of Ettore Majorana). The system is said to be the topological phase due to presence of this unbounded pair of Majorana mode.

On each site, perform a canonical transformation on the n^{th} fermionic excitation operators defined by,

$$c_n = \frac{1}{2}\left(\gamma_{2n} + i\gamma_{2n-1}\right), \tag{1.6}$$

where, the fermionic operators satisfy standard commutation relations,

$$\{c_i, c_j\} = \{c_i, c_j\} = 0, \quad \{c_i^\dagger, c_j\} = \delta_{ij} \tag{1.7}$$

and the real so-called Majorana operators γ satisfy

$$\gamma_i = \gamma_i^\dagger; \quad \{\gamma_i, \gamma_j\} = 2\delta_{ij}. \tag{1.8}$$

In terms of Majorana operators, the Hamiltonian can be re-expressed as

$$H = -\frac{\mu}{2}\sum_{n=1}^{N}\left(1 + i\gamma_{2n}\gamma_{2n-1}\right) - \frac{i}{2}\sum_{n=1}^{N-1}\left[\left(\Delta + t\right)\gamma_{2n}\gamma_{2n+1} + \left(\Delta - t\right)\gamma_{2n-1}\gamma_{2n+2}\right]. \tag{1.9}$$

Here we pause to note that it is clear from the canonical transformation given in Eq. 1.6 that Majorana modes always appear in pairs. In this case, each local fermionic operators can be thought of as a bound state of two Majoranas. However, while the mathematical transform to trade fermionic operators for Majorana operators can always be implemented, a system is said to truly host a pair of Majorana modes when the two modes can be physically separated so as to have no wavefunction overlap among them in the thermodynamic limit. In such case Majorana modes describe zero energy excitation. Now we will demonstrate how this can be achieved within a model of the one dimensional p-wave superconductor given in Eq. 1.9 following the Kitaev's original work [4].

Let us analyze the Hamiltonian in the following two limits. First, consider $\mu_p = 0$ and $t = \Delta$, in which case the Hamiltonian reduces to,

$$H = -it \sum_{n=1}^{N-1} \gamma_{2n}\gamma_{2n+1}. \tag{1.10}$$

In this special limit there are two unpaired Majorana modes at the end of the wire chain as shown in the Fig. 1.2. Since these Majorana modes do not enter the Hamiltonian there is no energy cost in exciting such modes. The excitation is best understood in terms of Fermionic operators that can be formed out of γ_1 and γ_{2N} using the transformation given in Eq.. 1.6,

$$f = \frac{1}{2}\left(\gamma_1 + i\gamma_{2N}\right). \tag{1.11}$$

The degenerate ground state of the system is characterized by the occupation number number of the non-local fermion f, $f^\dagger f = 0, 1$ and the system is said to be in a topological phase.

Now consider the limit $\Delta = t = 0$,

$$H = -i\mu \sum_{n=1}^{N} \gamma_{2n-1}\gamma_{2n} \tag{1.12}$$

In this limit Majorana mode pairs at each site are strongly coupled. There are no unpaired Majorana modes, and the system is said to be in the non-topological phase. The above two limiting cases are schematically described in the Fig. 1.2.

We have seen thus far that in the limiting cases discussed above, $\Delta = t = 0$ ($\mu_p = 0$ and $t = \Delta$) lead to the absence (presence) of unpaired Majorana modes. In presence of the unpaired Majorana modes, the ground state is doubly degenerate. This degeneracy is protected by the superconducting gap (ground state degeneracy can only change by closing the gap), i.e., even though we established two distinct phases at two special points in the parameter space, the respective phases have a finite extent in the parameter space where the phase boundary is marked by superconducting gap-closure. In general, if two Hamiltonians can not be continuously deformed into each other in the parameter space without going through a gap closure, the system represented by the two Hamiltonians are said to be in two distinct topological phases. We compute the superconducting gap below.

With the periodic boundary condition, Hamiltonian 1.9 can be expressed in momentum space as,

$$H = \sum_{k} (-2t\cos(k) - \mu) c_k^{\dagger} c_k + 2\Delta(i\sin(k) c_k c_{-k} + H.c.) \tag{1.13}$$

that can be represented in terms of so-called BdG Hamiltonian $\mathcal{H}_k$,

$$H = \frac{1}{2}\sum_{k\in BZ} C_k^{\dagger}\mathcal{H}_k C_k, \quad \mathcal{H}_k = \begin{pmatrix} \epsilon_k & \tilde{\Delta}^* \\ \tilde{\Delta} & -\epsilon_k \end{pmatrix} \tag{1.14}$$

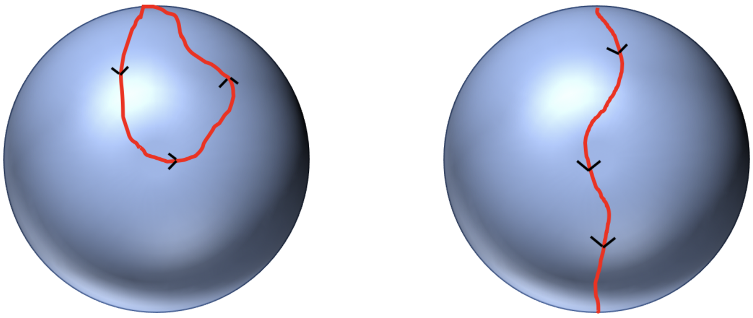

FIGURE 1.3: Two types of allowed trajectories that $\overrightarrow{h}(k)$ (assuming $\|\overrightarrow{h}(k)\| = 1$) can sweep as k is varied from 0 to π. The right (left) panel corresponds to a path for the system in the topological (non-topological) phase.

where $\epsilon_k = (-2t\cos(k) - \mu)$ and $\tilde{\Delta} = -i2\Delta\sin(k)$ and $C_k^\dagger = [c_k^\dagger, c_{-k}]$. $\mathcal{H}_k$ can be diagonalized to get the quasi-particle energy spectrum

$$E(k) = \pm\sqrt{(2t\cos(k) + \mu)^2 + (2\Delta\sin(k))^2}. \tag{1.15}$$

We find that the superconducting gap closes at $2t = \pm\mu$. Thus we conclude that the system is in topological phase (with unpaired Majorana modes) when $-2t < \mu < 2t$ and in non-topological phase otherwise. This is precisely the same conclusion we drew from our heuristic argument where we deduced that as long as the chemical potential is in the band, a single-band superconductor must be in the topological phase.

1.3 Topology and braiding of Majorana modes

In this section we hope to convey why Majoranas are intriguing. So far we have seen topological phase as a ground state property in 1D systems where in the topological phase, Majorana modes are protected by a superconducting gap. And the only way to push the system out of this phase is to close the gap. We will see that this is closely related to the mathematical notion of topology where in 1D the topological classification can be studied using homotopy of curves. Relatedly, we will also see that Majorana modes obey non-Abelian statistics which is the reason why Majorana modes have potential application for topological quantum computation. A more detailed discussion of the topics discussed in this section can be found in Refs. [10–14].

Let us expand BdG Hamiltonian (see Eq. 1.14) as a linear combination of Pauli matrices,

$$\mathcal{H}_k = \overrightarrow{\sigma} \cdot \overrightarrow{h}(k) \tag{1.16}$$

where, $\overrightarrow{\sigma} = \sigma_x \hat{x} + \sigma_y \hat{y} + \sigma_z \hat{z}$ and $\overrightarrow{h} = h_x \hat{x} + h_y \hat{y} + h_z \hat{z}$, $\sigma_{i=x,y,z}$ being the three Pauli matrices. Note that particle-hole symmetry obeyed by the BdG Hamiltonian, $\mathcal{H}_k = -\sigma_x \mathcal{H}^*_{-k} \sigma_x$ induces following constraints,

$$h_{x,y}(k) = -h_{x,y}(-k) \quad h_z(k) = h_z(-k). \tag{1.17}$$

This property guaranteed by particle-hole symmetry ensures $h(k)$ need to be specified on just one half of the Brillouin zone. Let us restrict ourselves to $k \in [0, \pi]$. The particle-hole symmetry constraints in Eq. 1.17 strongly restricts $\overrightarrow{h}$ at $k = 0, \pi$,

$$\overrightarrow{h}(k = 0, \pi) = h_z^{0,\pi} \hat{z}. \tag{1.18}$$

If we scale $\overrightarrow{h}$ such that $\|\overrightarrow{h}(k)\| = 1$, we must have $h_z^0, h_z^\pi \in \{-1, 1\}$. Thus there are two distinct topological paths that $\overrightarrow{h}(k)$ is allowed to trace on the unit sphere as k is varied from 0 to π in the Brillouin zone, as shown in Fig. 1.3. Either $\overrightarrow{h}$ maps to the same pole for the two end points at $k = 0$ and $k = \pi$ ($h_z^0 = h_z^\pi$) or it maps to two distinct (opposite) poles for each end point ($h_z^0 = -h_z^\pi$). In the case $h_z^0 = h_z^\pi$, $\overrightarrow{h}$ traces out a contractible path as opposed to $h_z^0 = -h_z^\pi$. These two topological distinct paths can be characterized by a topological index,

$$Q_H = \mathrm{sgn}(h_z^0 \cdot h_z^\pi). \tag{1.19}$$

Physically, Majorana modes are absent(present) in the system when $Q = 1(-1)$ and such a phase is called topologically trivial(non-trivial). Also note this argument breaks down if gap closes at some k ($\|\overrightarrow{h}(k)\| = 0$). Thus, this topological phase change must be accompanied by gap closure consistent with our earlier arguments.

Now, we will study the exchange statistics of Majorana modes. In order to do that, first we formally introduce Fermionic parity. We have seen that Majorana modes are zero energy excitations of a superconductor. While the mean-field superconducting Hamiltonian (which has been used to introduce Majorana modes so far) does not conserve the total number of electrons, the Fermionic parity, that distinguishes odd versus even total electrons in the superconductor, is a well-defined quantum number. Abstractly, consider a superconducting ground state with N pairs of Majorana-zero-modes (MZMs) where the Majorana modes are denoted by $\gamma_1, \gamma_2, \dots, \gamma_{2N-1}, \gamma_{2N}$. These Majorana modes can be pairwise combined to form Fermionic operators c_n's using Eq. 1.6. The eigenvalue $1(-1)$ of the operator P_n defined by $P_n \equiv 1 - 2c_n^\dagger c_n$ corresponds to n^{th} Fermionic state being unoccupied(occupied). Therefore, the ground-state parity can be defined by,

$$P = \prod_{n=1}^{N} P_n = i^N \prod_{n=1}^{N} \gamma_{2N-1}\gamma_{2N}. \tag{1.20}$$

For $2N$ Majorana modes, the ground state is 2^N degenerate. However, since parity must be conserved the physical degeneracy is 2^{N-1}.

The notion of parity conservation is useful to understand Majorana exchange. Consider Majorana modes γ_n, γ_m that are to be adiabatically exchanged. The exchange must be represented by a unitary operator U, such that,

$$U\gamma_m U^\dagger = s_1\gamma_n; \quad U\gamma_n U^\dagger = s_2\gamma_m \tag{1.21}$$

where, s_1, s_2 are real numbers satisfying $s_1^2 = s_2^2 = 1$ (this follows from reality of Majorana operator). Furthermore, U must commute with parity

$$i\gamma_m\gamma_n = -s_1 s_2 i\gamma_m\gamma_n, \tag{1.22}$$

which implies $s_1 s_2 = -1$. A unitary operator that satisfies these properties and only depends on γ_m and γ_n is

$$U_{m,n} = e^{\frac{\pi}{4}s\gamma_m\gamma_n} = \frac{1}{\sqrt{2}}(1 + s\gamma_n\gamma_m) \tag{1.23}$$

with $s = \pm 1$. Physically, the two s values distinguish clockwise versus counter-clockwise braiding. Indeed, using this unitary Majorana exchange operator, one can demonstrate the non-Abelian braiding statistics that are obeyed by Majorana modes. In order to study non-Abelian braiding, the physical ground state must be at least doubly degenerate. Therefore, we consider a set of four Majorana modes. The exchange operator, U can be represented as,

$$U = e^{i\frac{\pi}{4}\sigma_z} \tag{1.24}$$

where the Pauli matrix σ_z acts on the Fermionic parity qubit formed by the Majoranas being exchanged (this can be easily seen by representing the two Majoranas that are exchanged by σ_x and σ_y, respectively). Let the subspace consisting of four Majorana

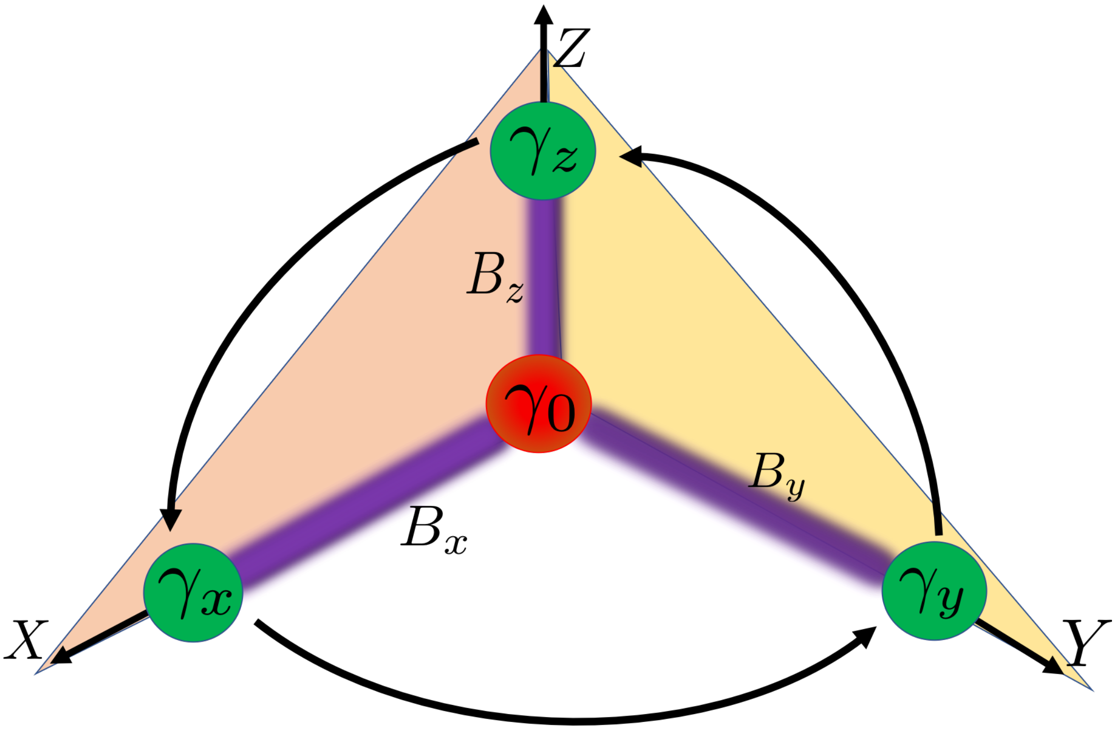

FIGURE 1.4: A schematic description of time-dependence of the braiding Hamiltonian given in Eq. 1.25. A specific protocol that exchanges γ_z and γ_y is initialized by coupling γ_0 and γ_x at $t = 0$ while γ_z and γ_y are free. We denote the coupling by $\overrightarrow{B}$. The braiding protocol involves three back-to-back sequences, where each sequence is a rotation of the coupling field $\overrightarrow{B}$ by $\pi/2$ about an axis while $\|\overrightarrow{B}\| = 1$ is held fixed. The first, second and the third sequence rotations in $\overrightarrow{B}$ field are about z, x and y axes as denoted by the arrows. In this example $\overrightarrow{B}$ points along $\hat{x}$ initially and returns to this initial configuration after three rotation sequences.

operators γ_{1-4} be represented in the Fermionic qubit basis $|00\rangle, |01\rangle, |10\rangle, |11\rangle$, where the first (second) qubit is formed using $\gamma_{1,2}$ ($\gamma_{3,4}$). It can be checked using Eq. 1.24 that $U_{1,2}U_{2,3} \neq U_{2,3}U_{1,2}$. In this example, this inequality highlights the non-Abelian nature of Majorana braiding.

While the quantum information stored in the distinct topological states of MZMs is topologically protected from decoherence, topological quantum computation relies on

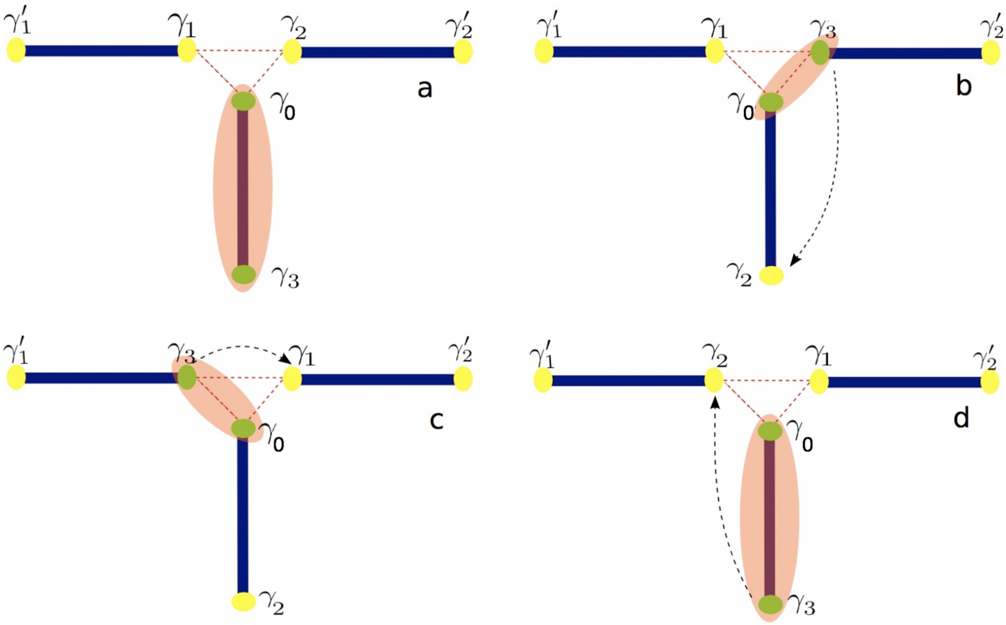

FIGURE 1.5: A schematic diagram for braiding a pair of Majoranas using a tri-junction (also called Y-junction). The system is initialized (a) such that γ_1', γ_1, γ_2' and γ_2 are four localized Majorana modes and (γ_0,γ_3) Majorana pair is paired into a Dirac fermion. Paired Majorana modes are depicted as green discs where the non-zero pairing strength B_k in Eq. 1.25 (subscript k here is denoted by $1, 2, 3$ instead of x, y, z) is represented by pink oval. At every move an unpaired Majorana mode is moved from one position to another. The movement of the Majorana resulting from the move resulting in each configuration (b-d) is shown by a dashed arrow.

manipulating the quantum information by exchanging Majorana modes with each other. Experimental demonstration of such non-Abelian statistics using Majorana modes is a major milestone that lies ahead in the path towards practical topological quantum computation. Several theoretical proposals have been put forward to exchange Majorana-zero-modes emergent in one-dimensional systems [15–18]. We have already seen that Majorana-zero-modes demonstrate non-Abelian braiding statistics upon exchange. The exchange statistics is independent of details of the protocol of exchange, as seen from

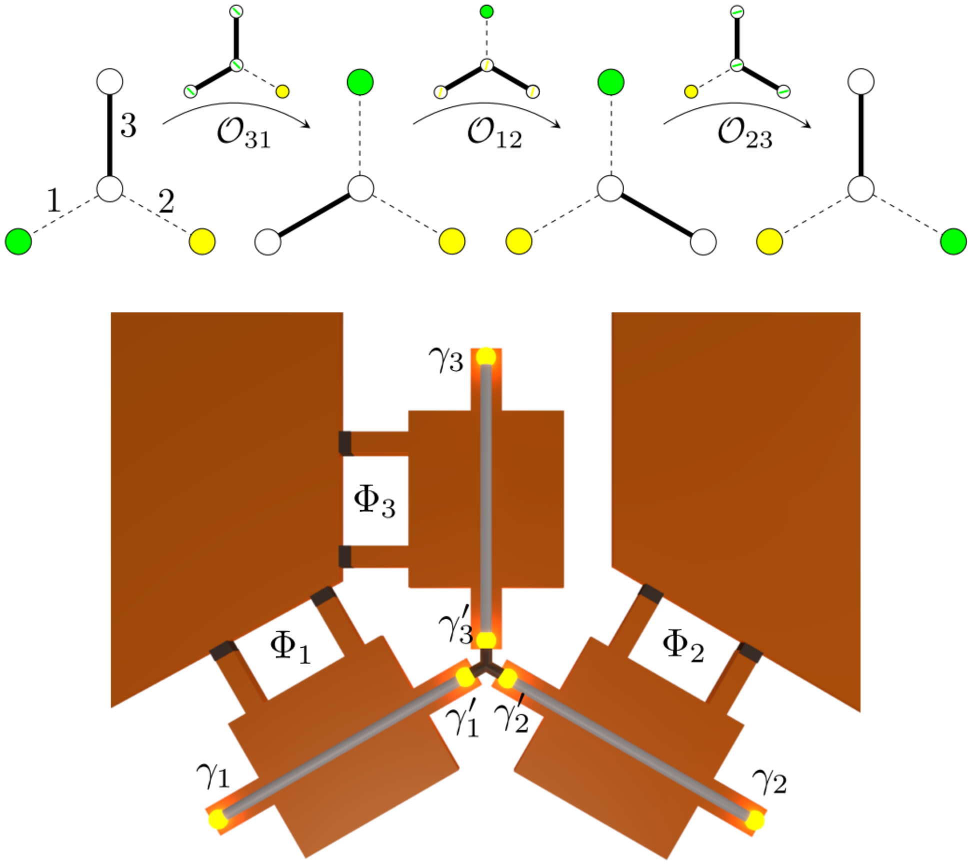

FIGURE 1.6: (Bottom) Tri-junction (also called Y-junction) of three Cooper-pair boxes where three overlapping Majoranas effectively create a single zero mode γ_0 where $\gamma_0 = \frac{1}{\sqrt{3}}(\gamma_1' + \gamma_2' + \gamma_3')$. (Top) Schematic of representation for Majorana exchange in three steps. Colored circles represent free Majorana modes whereas strongly coupled Majorana modes are denoted by white circles. The system is governed by Hamiltonian in Eq. 1.25. Non-zero values of Majorana coupling B_k in Eq. 1.25 (the Majorana subscript here is denoted by $1, 2, 3$ instead of x, y, z as in Eq. 1.25) is denoted by solid line. Intermediate configuration is represented by smaller diagram above each arrow where a single Majorana is delocalized over three coupled sites. Figure adapted from Ref. [15]

Eq. 1.24. The dynamics of Majorana exchange can be studied using the prototypical Y-junction (also called tri-junction) architecture of four Majorana modes that is governed by the Hamiltonian,

$$H = i\gamma_0(\overrightarrow{B}(t).\overrightarrow{\gamma}), \tag{1.25}$$

with $\overrightarrow{\gamma} = (\gamma_x, \gamma_y, \gamma_z)$. $\overrightarrow{B}$ describes coupling among Majoranas such that there is at least one uncoupled Majorana γ_i for $i \in \{x, y, z\}$ at all times. The braiding protocol is based on the tunneling induced transport of MZMs [16] (see Fig. 1.5) where the splitting between pairs of MZMs is used to exchange the decoupled MZMs $\gamma_{y,z}$ (see Fig. 1.4) that are used to store quantum information. Fig. 1.4 describes a particular example of a braiding protocol that leads to exchange of γ_y and γ_z. Since the system is isolated (apart from the Bosonic bath), the total Fermion parity of the system is conserved throughout the braiding protocol. Using the fact that at least one of the MZMs $\gamma_{x,y,z}$ are isolated from the rest of the MZMs at any time in the protocol, it can be shown [19] that the two Fermion parity states remain topologically degenerate. Both the initial and final state leave $\gamma_{y,z}$ decoupled from everything else. Therefore, the conservation of Fermion parity equates the conservation of the MZM parity $i\gamma_y\gamma_z$, which is used to store quantum information, to the conservation of the of the Fermion parity of the coupled pair $\gamma_{0,x}$. The latter is associated with excitations of the system, so that the bit-flip error is directly related to the rate of exciting the system out of the ground state into the excited state. The ground and excited states are the only states in a fixed Fermion parity sector.

It must be noted that while $\overrightarrow{B}$ in Eq. 1.25 describe tunnel coupling in the protocol described in Fig. 1.5, it might as well describe Coulomb coupling [15] tunable through a Josephson junction flux as described in Fig. 1.6.

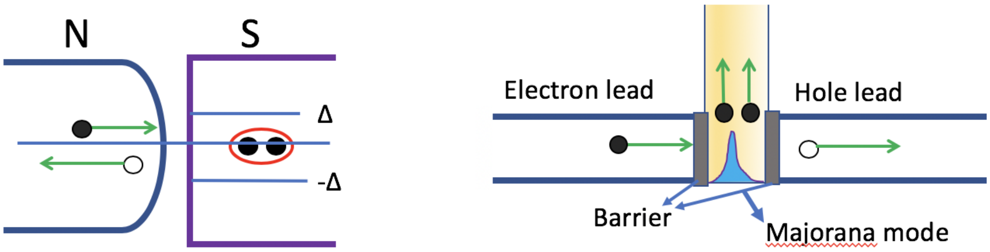

FIGURE 1.7: (Left) A schematic representation of Andreev reflection. An electron incident on the superconductor with energy E less than the superconducting gap Δ is reflected as a hole with energy $-E$. Physically, it can be understood as two electrons with energy E and $-E$ from the normal lead enter the superconductor by forming a zero-energy Cooper pair. (Right) Schematic representation of Andreev reflection understood as a transmission phenomenon from the electron-channel to the hole-channel of the normal lead through a double barrier. For ordinary superconductors probability of Andreev reflection sensitively depends on the normal lead-superconductor-contact-barrier. However, a Majorana-zero-mode at the superconductor edge acts as a zero energy bound state that between the two barriers and hence an electron is resonantly transmitted as hole, i.e. it allows for perfect Andreev reflection.

1.4 Experimental signature of Majorana modes

Now we would want to understand the phenomenology of emergent Majorana modes in 1D especially with regards to quasiparticle transport. A defining characteristic property of Majorana-zero-modes is perfect resonant Andreev reflection. First, let us understand the phenomenon of Andreev reflection in ordinary superconductors. Consider a superconducting Hamiltonian,

$$H_{BdG}^{cont} = \left(\frac{\hat{p}^2}{2m} - E_F \right) \sigma_z + \Delta \sigma_x \tag{1.26}$$

where E_F is the Fermi energy. Let the superconductor be a semi-infinite chain with one end at $x = 0$ and extending over $x > 0$. To understand low-energy quasiparticle scattering we will consider scattering of a right moving electron at energy E_F impinging the superconductor at $x = 0$,

$$\Psi^{in}_{x<0} = e^{ik_F x} \begin{pmatrix} 1 \\ 0 \end{pmatrix}. \tag{1.27}$$

Let the scattered wavefunction in superconductor be written as $\Psi^{out}_{x>0} = e^{ik_F x}\psi$. Approximating the above Hamiltonian by linearizing the momentum close the right Fermi point (with momentum along positive x axis), we solve for ψ that satisfies $H^{cont}_{BdG,R}\psi = 0$, where

$$H^{cont}_{BdG,R} \approx v_F \left(-i\frac{\partial}{\partial x}\right)\sigma_z + \Delta\sigma_x, \tag{1.28}$$

to get

$$\psi(x) = e^{\frac{\Delta}{v_F}x\sigma_y}\psi(0). \tag{1.29}$$

Normalization of ψ restricts $\psi(0)$ to be proportional to negative eigenvalue of σ_y and thus,

$$\Psi^{out}_{x>0} \propto e^{ik_F x} e^{-\frac{\Delta}{v_F}x} \begin{pmatrix} 1 \\ -i \end{pmatrix}. \tag{1.30}$$

This dictates the reflected wave must be of the form,

$$\Psi^{out}_{x<0} \simeq e^{ik_F x} \begin{pmatrix} 0 \\ -i \end{pmatrix}. \tag{1.31}$$

We observe that an incident electron is reflected back as a hole with the same momentum but opposite velocity. This phenomenon is known as Andreev reflection. It is easy to extrapolate that in general, when an incident electron energy is within the superconducting gap, due to absence of propagating states in the superconductor, Andreev reflection must generically occur. In practice a normal lead is brought in proximity to the superconductor separated by a tunnel barrier, and the Andreev process is physically understood as extraction of two electron from the normal lead into the superconducting condensate as shown in Fig. 1.7 (left panel).

The analytical description of Andreev reflection presented above is an idealization. In practice, the potential barrier between the normal lead and the superconductor sensitively affects the probability of Andreev reflection. This can be understood in the following way: Andreev reflection is essentially a transmission process of a particle from the electron channel to the hole channel in the normal lead through a potential double barrier. In general the probability of transmission though potential barrier is less than one and decreases with the increase in barrier potential strength. However, a Majorana mode presents itself as a zero-energy bound state that allows resonance transmission from the electron to the hole lead. In other words, a MZM facilitates perfect Andreev reflection at zero energy. This argument is schematically depicted in Fig. 1.7 (right panel). This fact has been rigorously demonstrated in a number of theoretical investigations such as [20–23].

Such resonant Andreev reflection can be used as probe to detect MZMs. Experimentally, conductance spectroscopy is a powerful tool to measure and characterize transport properties of one-dimensional superconductors. Typically, it involves measuring differential conductance across a normal lead-nanowire tunnel junction. The measured differential conductance is defined as

$$G = \frac{\partial I}{\partial V}, \tag{1.32}$$

where I is the current through the normal lead and V is the voltage bias of the normal-lead with respect to the nanowire, respectively. A useful relation derived by Blonder, Tinkham and Klapwijk [24] relates the differential conductance G to the reflection matrix amplitudes for a single channel transport,

$$G = \left[1 - |r_{ee}|^2 + |r_{eh}|^2\right] G_0. \tag{1.33}$$

where r_{ee} (r_{eh}) is normal (Andreev) reflection amplitudes and $G_0 = e^2/h$ is the conductance quantum, respectively. This relation is extremely useful as particle-hole symmetry of the Hamiltonian can be used to deduce quite general relation that must be satisfied by reflection matrix amplitudes and thereby imposes certain universal constraints on G. For voltage bias within the superconducting gap, the reflection matrix,

$$r = \begin{pmatrix} r_{ee} & r_{eh} \\ r_{he} & r_{hh} \end{pmatrix}. \tag{1.34}$$

is unitary on account of the absence of extended states in the superconductor. As an aside, note that we have represented the reflection matrix in the so-called particle-hole basis. Unitarity of the reflection matrix implies

$$(r_{ee} r_{he}^* + r_{eh} r_{hh}^*) = 0. \tag{1.35}$$

For finite voltage bias V, the particle-hole constraint on the voltage-dependent reflection matrix $r(V)$ takes the form $\tau_x r(V) \tau_x = r(-V)^*$. For bias $V = 0$, we get

$$r = \begin{pmatrix} r_{hh}^* & r_{he}^* \\ r_{eh}^* & r_{ee}^* \end{pmatrix}. \tag{1.36}$$

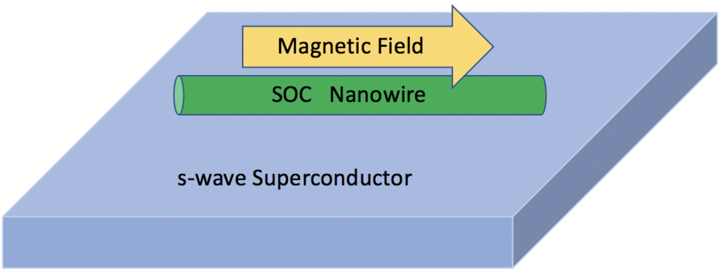

FIGURE 1.8: Schematic representation of nanowire heterostructure to engineer a spinless superconductor. Superconductivity in induced in a semiconductor nanowire endowed with spin-orbit coupling by a proximate s-wave superconductor. Band degeneracy is broken by an applied magnetic field parallel to the nanowire.

Combined with the unitarity condition we arrive at the relation,

$$r_{ee}r^*_{eh} = 0. \tag{1.37}$$

Thus, at exactly zero voltage, a normal lead-superconductor junction exhibits either perfect normal reflection or perfect Andreev reflection. We have already seen that perfect Andreev reflection is associated with the presence of Majorana modes, therefore, the above criterion can be exploited to deduce a scattering matrix invariant to diagnose topological phase. In fact a basis-independent formulation of Eq. 1.37 was suggested in Ref. [25],

$$Q_0 = \mathrm{sgn}(\det(r)) \tag{1.38}$$

where, $Q_0 = -1$ ($Q_0 = 1$) corresponds to topological (non-topological) phase.

1.5 Majorana modes in nanowire heterostructure

Thus far we have explored the existence of Majorana modes in one-dimensional p-wave superconductiors. The crucial property that allowed Majorana modes was the presence of a single superconducting band at the Fermi level- a requirement easily satisfied by model 1D spinless systems, However, progression from a theoretical demonstration to a laboratory realization of Majorana modes is hampered by one practical and one fundamental problem. The practical problem is that one-dimensional superconductors are hard to engineer. Secondly there is the fundamental fact that electrons are endowed with spin. However, one-dimensional or rather quasi one-dimensional semiconductors can be easily grown in a laboratory. Given this, the first problem can be overcome by inducing superconductivity in a one-dimensional semiconductor wire using a proximate s-wave (spinful) superconductor. Now given a one-dimensional spinful superconductor, one can effectively simulate spinless superconductivity by separating the two spin-bands by some energy gap. In general, even when spin is not a good quantum number, Kramers's theorem guarantees that every eigenstate in a system endowed with time-reversal symmetry is doubly degenerate. This problem can be overcome by introducing a magnetic field. This so-called Zeeman (magnetic) field lifts the spin degeneracy (and in general lifts the Kramer's degeneracy since the introduced magnetic field breaks the time-reversal symmetry). The resulting nanowire Hamiltonian can be expressed as

$$H_{BdG}^{NW}(k) = (k^2/2m - \mu + k\alpha\sigma_y)\tau_z + V_z\sigma_z + \Delta\tau_x \tag{1.39}$$

The topological transition can be understood by tracking gap closure in $H(k = 0)$ as a function of parameters. The four eigenenergies at $k = 0$ are $E = \pm V_z \pm \sqrt{\mu^2 + \Delta^2}$. Since for $V_z = 0$ the system must be in the non-topological phase based on the above arguments, we conclude that the topological transition takes place when,

$$V_z > \sqrt{\Delta^2 + \mu^2}. \tag{1.40}$$

Indeed, the existence of Majorana modes were predicted in one-dimensional heterostructures schematically represented in Fig. 1.8, where spin-orbit-coupled nanowire in a magnetic (Zeeman) field is endowed with proximity-induced superconductivity, by several several groups [26–29]. Further details can be found in the reviews [14, 30].

1.5.1 Experimental status of Majorana modes in nanowire proposal

There has been tremendous experimental progress towards realization of Majorana modes using nanowire heterostructure proposal in the last 6 years [31–38]. A watershed moment in this direction was the experimental results published by the Kouwenhoven group at Delft in 2012. In the experiment differential conductance is measured across a tunnel barrier separating a normal lead and a semiconductor nanowire. The (semiconductor) nanowire-superconductor heterostructure (as shown in Fig. 1.8) is realized by depositing indium-arsenide (InAs) on the surface of a niobium-titanium-nitride (NbTiN) superconductor. The scanning electron microscope image of the experimental setup is shown in Fig. 1.9a. The key result in the work is the differential conductance measurement plot shown in Fig 1.9b. The plot shows a trace of $\frac{dI}{dV}$ as function of bias voltage V for various values of Zeeman field strength. In accordance with the theoretical expectation, a zero-bias-conductance-peak (ZBCP) appears as the Zeeman field is increased beyond a critical value. While this is encouraging we immediately see that there are several critical deviations from the ideal theoretical expectations. Some key such deviations are as follows. First and foremost, the ZBCP peak is nowhere close to the quantized value of $2e^2/h$ expected from perfect Andreev reflection. In fact, the

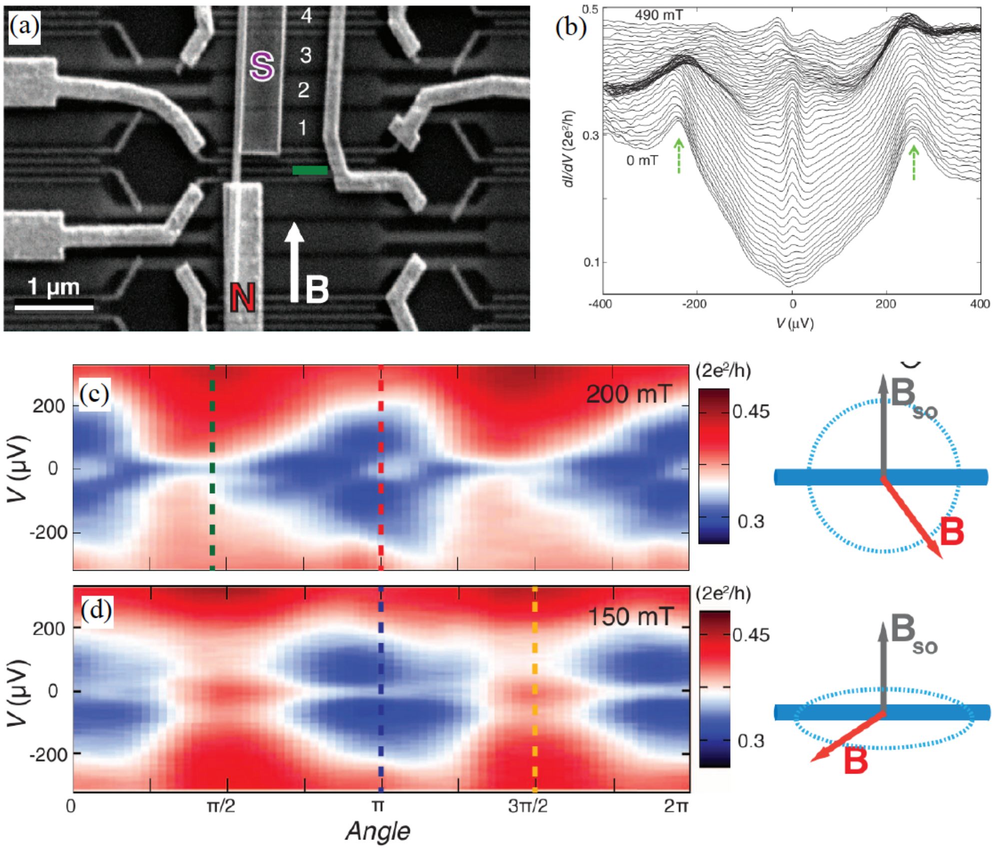

FIGURE 1.9: Experiment by Kouwenhoven group at Delft based on the nanowire proposal. (a) Scanning electron microscope image of the experimental setup. An InAs semiconductor nanowire is placed in contact with normal-metal (denoted by N) and superconducting (denoted by S) electrodes as shown. The gates labelled 1-4 are used to tune chemical potential in the nanowire. The tunnel-barrier is shown in green. (b) Differential conductance ($\frac{dI}{dV}$) as a function of bias voltage for varying magnetic field strengths (0-490 mT). The traces for different magnetic fields are offset for clarity. (c) $\frac{dI}{dV}$ vs V as a function of angle of the magnetic field where the magnetic field is perpendicular to the spin-orbit-coupling (SOC) direction at angle=$0, \pi$ and parallel to the SOC direction at angle=$\frac{\pi}{2}$, $\frac{3\pi}{2}$. (d) Differential conductance as a function of angle of the magnetic field while magnetic field is restricted in the plane perpendicular to the SOC direction. Figure adapted from Ref. [31]

.

suppression is close to a factor of 10 from the expected value. Second, the induced superconducting gap is not reflected in the conductance plot. This feature which is universally present in all subsequent experiments to some degree is commonly known as the “soft gap” problem. Theoretically, when the voltage bias is within the superconducting gap, the conductance is expected to be extremely suppressed in the tunneling regime and as the bias is increased further, the differential conductance attains finite values once the bias voltage is within the bulk superconducting spectrum. This feature is manifestly absent in the experimental result. Third, as a function of the Zeeman field, the ZBCP disappears again as the magnetic field field is increased beyond 400 mT.

Various theoretical studies have connected the observed deviations from the ideal expectations in the topological phase to certain practical imperfections of an experimental setup [39–43]. The finite length of nanowire means that the Majorana modes are separated over finite distance. The resulting wavefunction overlap splits the Majorana modes away from ideal zero energy. Absence of such Majorana splitting signature in the experimental results suggest that the dissipative broadening is greater than the Majorana splitting. Indeed, in theoretical simulations, dissipative and thermal broadening effects have been shown to affect the height and width of the ZBCP [41]. On the other hand, the “soft gap” feature (“V” shaped region in Fig. 1.9b) can be understood by invoking the fact that disorder (which must invariably be present in any realistic system) induces subgap states. However, disorder alone can not be a satisfactory explanation because the soft gap feature is present at zero magnetic field as well. Since time-reversal symmetry is restored at zero magnetic field, Anderson’s theorem protects the clean gap against the effects of disorder [44]. As an alternative, hybridization between the nanowire and the metallic was posited as a mechanism for the soft gap feature in Ref. [42].

On the other hand, non-topological mechanisms have been put forward to explain the appearance of ZBCP [45–50]. In the presence of strong disorder, it was shown in

Ref [40] that a ZBCP can be induced even when the system is in the non-topological regime. Another possible alternative candidate for producing zero bias conductance peaks is conventional zero-energy Andreev states. In fact, in superconducting systems where spin rotation symmetry is broken by spin-orbit coupling and time-reversal symmetry is broken by the magnetic field are in symmetry class D [51] and show a zero energy peak in the disorder-averaged density of states [49]. For superconducting systems with a large number of channels in contact with a lead, this peak in the disorder averaged density of states evolves into a weak anti-localization ZBCP [52, 53]. The states that contribute to the zero-energy peak in class D [54] superconductors arise from the absence of avoided crossings between Andreev states crossing each other at zero energy. Such states split in energy linearly as a function of magnetic field, leading to an X-type resonance as opposed to MZMs that remain at zero energy over a range of magnetic field forming a Y-type resonance [55]. Unfortunately, coupling to a normal lead can cause conventional Andreev states to show a Y-type behavior as a function of magnetic field similar to the ZBCP from MZMs [55]. Liu et al [48] have used detailed transport calculations for realistic parameters corresponding to disordered InSb nanowires to argue that a ZBCP, which is qualitatively as robust as the ZBCP seen in experiments [31], can occur in the non-topological regime. In another study, by computing the topological invariant in the presence of disorder Adagidelli et al [56] have shown that disorder can transform non-topological regions of parameter space into topological regions. In the wake of such competing mechanisms to interpret the experimental results, we require an experimental protocol that can truly distinguish whether or not the experimental signature and particularly the zero-bias peak is due to presence of underlying Majorana modes. We propose one such protocol in chapter 4.

If indeed the ZBCP signature in the nanowire heterostructure is associated with the topological phase, the underlying Majorana modes are expected to be imperfect (Majorana modes may be split) because of various non-idealities in the system (e.g. disorder, temperature, tunnel coupling to the environment, finite wire length, Majorana splitting, etc.) and thus produce a ZBCP which is highly suppressed (and broadened) compared to the canonically quantized value of $2e^2/h$ [21, 42, 43, 57, 58]. Due to potential application of non-Abelian braiding properties of Majorana modes in topological quantum computation, the immediate question then is whether (or perhaps, to what extent) such imperfect almost-MZMs would have intrinsic non-Abelian braiding properties possibly showing up in a (future) experiment. In the absence of a braiding experiment to directly observe non-Abelian statistics for Majorana exchange at present, we are left to speculate on the extent to which non-Abelian statistics would be observed when nanowire MZMs are braided based on the only available experimental signal for their existence, i.e., ZBCP. It is then prudent to ask if we can relate the observed (non-ideal) characteristics of the ZBCP, i.e. height and width of the peak, to the topological content of the approximate MZMs. We address this question in chapter 3.

1.6 Outline of the thesis

Majorana mode based topological qubits are potentially subject to diabatic errors that in principle can limit the utility of topological quantum computation. In chapter 2, diabatic errors in Majorana-based topological Y-junction that are coupled to a Bosonic bath are studied in the Markovian approximation. From the study it is found analytically that in the absence of a bath, the error rate can be made exponentially small in the braiding time only for completely smooth pulse shapes. Thus, pristine topological systems can reach exponentially small errors even for finite braid times. The presence of a Markovian bath is found to eliminate this exponential scaling of error to a power-law scaling as T^{-2} with T being the braiding time. Thus, coupling of topological systems to Bosonic baths can lead to powerlaw in braiding time diabatic errors that might limit the speed of topologically protected operations.

In chapter 3, we consider a simple conceptual question with respect to Majorana zero modes in semiconductor nanowires: Can the measured non-ideal values of the zero-bias-conductance-peak in the tunneling experiments be used as a characteristic to predict the underlying topological nature of the proximity induced nanowire superconductivity? In that chapter, we define and calculate the topological visibility, which is a variation of the topological invariant associated with the scattering matrix of the system as well as the zero-bias-conductance-peak heights in the tunneling measurements, in the presence of dissipative broadening, using precisely the same realistic nanowire parameters to connect the topological invariants with the zero bias tunneling conductance values. This dissipative broadening is present in both (the existing) tunneling measurements and also (any future) braiding experiments as an inevitable consequence of a finite braiding time. The connection between the topological visibility and the conductance allows us to obtain the visibility of realistic braiding experiments in nanowires, and to conclude that the current experimentally accessible systems with non-ideal zero bias conductance peaks may indeed manifest (with rather low visibility) non-Abelian statistics for the MZMs. It turns out that a large (small) superconducting gap (Majorana peak splitting) is essential for the manifestation of the non-Abelian braiding statistics, and in particular, a zero bias conductance value of around half the ideal quantized Majorana value should be sufficient for the manifestation of non-Abelian statistics in experimental nanowires. We will find that the topological transition associated with the emergence of MZMs in finite nanowires is always a crossover (akin to a quantum phase transition at finite temperature) requiring the presence of dissipative broadening (which must be larger than the Majorana energy splitting in the system) in the system. For braiding, this dissipation is supplied by the finite speed of the braiding process itself which must be diabatic in any real experiment.

We have already discussed that the mere presence of a zero bias conductance peak in tunneling conductance experiments on nanowire heterostructure is not sufficient to establish presence of Majorana modes even though it is a necessary signature for their presence. However, in such experiments, the zero bias conductance peak, similar to that predicted to arise from Majorana modes, appears above a critical strength of magnetic field. It is shown in chapter 4 that the appearance of this zero bias peak from Majorana modes should be correlated between the ends of the wire. Such correlation is not likely to occur in non-topological one dimensional systems and can be used to distinguish Majorana modes from conventional zero energy peaks arising due non-topological mechanisms.

Chapter 2: Diabatic errors in braiding with Bosonic bath

Most of the studies regarding the possibility of exponentially small error in topological qubits realized from MZMs have been in the equilibrium phase. A less studied question is the protection of quantum information stored in MZMs to diabatic errors resulting from the finite speed of operations [59–62]. Specifically, one might worry that since the topological phase of matter is a ground state property, finite gate speed might have an effect of taking the system out of the ground state in a way that introduces errors. This issue has been raised in some studies of the dynamics of braiding [62] that suggest the use of a measurement based protocol as a possible way to avoid such diabatic errors. In contrast key-board based braiding protocols [17] seem to reduce some of the diabatic errors and find error rates that scale exponentially in the rate of the process [18, 63]. Another potentially critical ingredient in MZM braiding is the interaction of the MZMs with a Bosonic bath. While the effects of a Bosonic bath on stationary MZMs have been studied [64–67], its effect of diabatic braiding have been not been investigated until recently [63] (also see Ref. [68]) where the combined effect of (Bosonic) environmental noise and diabatic braiding is found to result in powerlaw scaling errors even for the keyboard-like braiding schemes [63].

In this chapter we focus on the question of diabatic errors in nominally the simplest braiding protocol in a Y-junction type Majorana architecture coupled to a Bosonic bath. We introduced the Y-junction and the associated Majorana braiding Hamiltonian in Sec. 1.3 (see Fig. 1.4). We will show that the system in Fig. 1.4 is topologically protected against dephasing errors in the Fermion parity basis. Therefore the problem of bit-flip errors in the system in Fig. 1.4 can be mapped entirely to the relatively well-studied problem of diabatic errors for a spin in a time-dependent magnetic field (see for e.g. [69, 70]).

Despite the mapping of the system in Fig. 1.4 to a spin in a magnetic field, the topological nature of the set-up leads to certain unique features when considering interactions of the system with a Bosonic bath. Microscopically, we assume the Bosonic bath couples to the spin as a magnetic field noise similar to the classic spin-Boson model [71, 72]. To simplify our treatment, we assume that the coupling to the Bosonic bath is weak compared to temperature (much smaller than the gap) so that the bath can be modeled within the Markovian approximation using the Davies prescription [73, 74]. However, unlike a conventional spin, the vanishing of a component of the magnetic field also implies a vanishing of the noise. This is because such a vanishing of a component of the magnetic field is assumed to occur because of isolation of one of the MZMs from the rest of the system. This leads to conservation of the associated MZM operator, which in turn leads to conservation of the associated excitation. Specifically, this means that for the setup in Fig. 1.4, the Bosonic bath is forced to decouple from the topologically protected quantum information at the end of the process. However, this also means that any excitation generated during the dynamics of the effective magnetic field cannot relax away at the end of the process. This is in contrast to the dynamics in the spin-Boson model, where the system in contact with a zero-temperature Bosonic bath would always relax back to the ground state once the magnetic field becomes static at the end of the process. The absence of such relaxation leads to the a finite excitation probability in the braiding set-up in Fig. 1.4, which leads to the possibility of the bit-flip error.

Motivated by the mapping of the set-up of Fig. 1.4 to a spin in a magnetic field, in this chapter we study the probability of excitation of a spin in a time-dependent magnetic field that is coupled to a Bosonic bath. The coupling to the Bosonic bath is assumed to be small enough so that it can be studied within the Markovian approximation using the Davies prescription [73, 74]. This leads to a time-dependent master equation which is further reduced to a Bloch equation describing spin-1/2 particles with relaxation and dephasing [74, 75]. To simplify the parameter space of possibilities, we assume that the temperature is low enough so that thermal excitation can be ignored. We show analytically that the excitation probability in such as spin-system (corresponding to the error rate in Fig. 1.4) vanishes only polynomially as the time, T, within which the braid in completed.

2.1 Braiding Hamiltonian and Bosonic bath

Given a system coupled to heat bath, the master equation relates time evolution of the system density matrix to the system Hamiltonian and a set of operators commonly known as *jump* operators [75]. We begin this section with the description of the Majorana braiding Hamiltonian followed by an outline of the master equation that describes the dynamics of the Majorana (braiding) system coupled to a bath. We conclude this section by writing the master equation in its equivalent Bloch equation form that simultaneously describes dynamics of a spin-1/2 system coupled to thermal bath.

2.1.1 Braiding Hamiltonian

Let us rewrite the braiding Hamiltonian introduced in Eq. 1.25,

$$H = i\gamma_0(\overrightarrow{B}(t).\overrightarrow{\gamma}), \tag{2.1}$$

where, $\overrightarrow{\gamma} = (\gamma_x, \gamma_y, \gamma_z)$. $\overrightarrow{B}$ describes coupling among Majoranas such that there is at least one uncoupled Majorana γ_i for $i \in \{x, y, z\}$ at all times.

It is convenient to express Majorana operators in terms of Pauli matrices. Using the definitions,

$$\begin{aligned} \gamma_x &= \sigma_x \tau_x \quad ; \quad \gamma_y = \sigma_y \tau_x \\ \gamma_z &= \sigma_z \tau_x \quad ; \quad \gamma_0 = \tau_y, \end{aligned} \tag{2.2}$$

(where τ and σ are two sets of Pauli matrices) the Hamiltonian in Eq. 2.1 can be rewritten as,

$$H = \overrightarrow{B}(t).\overrightarrow{\sigma}\tau_z. \tag{2.3}$$

The Hamiltonian commutes with the fermionic parity operator $\hat{P}$, $[H, \hat{P}] = 0$ with $\hat{P} = \gamma_0\gamma_x\gamma_y\gamma_z = \tau_z$. If some component B_a of $\overrightarrow{B}$ is zero, then $\sigma_a\tau_x$ commutes with the Hamiltonian but anti-commutes with $\hat{P}$, which in turn commutes with H. Therefore there is a two-fold degeneracy for the two values of $\hat{P}$. Since parity is conserved, the closed-system Hamiltonian dynamics is effectively captured by the reduced *2-level* Hamiltonian,

$$H_{2Level} = \overrightarrow{B}(t).\overrightarrow{\sigma}. \tag{2.4}$$

The general time-dependence is visualized in Fig. 1.4. The geometric arrangement of the Majoranas depicted in the cartoon is solely for elucidation and has no bearing on actual arrangement of Majoranas in a braiding experiment. The time evolution involves a series of three back-to-back sequences with $||\overrightarrow{B}|| = 1$ throughout. Initially, $\overrightarrow{B}$ points along positive-x axis, $\overrightarrow{B}(t = 0) = (1, 0, 0)$. In the first sequence $\overrightarrow{B}$ is rotated about the z-axis until $\overrightarrow{B}$ points along positive y-axis at time $t = T$, $\overrightarrow{B}(t = T) = (0, 1, 0)$. In the second sequence $\overrightarrow{B}$ is rotated about the x-axis until time $t = 2T$ such that, $\overrightarrow{B}(t = 2T) = (0, 0, 1)$. and finally $\overrightarrow{B}$ is rotated about the y-axis until time $t = 3T$ such that, $\overrightarrow{B}(t = 3T) = (1, 0, 0)$. A time-cycle represented by these three sequences, $H(t = 0) = H(t = 3T)$, results in exchange of Majoranas γ_y and γ_z. Note that γ_z, γ_x and γ_y commute with the Hamiltonian during first, second and the third sequence, respectively.

For each sequence, the diabatic drive must be slow to prevent undesired excitations in the system. If the diabatic drive is infinitely slow, the adiabatic theorem ensures that system remains in the ground state. For a diabatic drive over a finite T, typically, these undesirable excitations are small as long as T is much greater than the ground state energy gap. However, for fixed T, the deviation from the adiabatic result or the diabatic correction depends on precise time-dependence of the diabatic drive. A sensible requirement for the diabatic drive is the absence of discontinuities as a function of time. In other words, we require the diabatic drive to be completely smooth as a function of time (known as C^∞ function in the mathematics literature). To be specific, let us focus on the diabatic drive of the first sequence of the braiding protocol as discussed above. The $\overrightarrow{B}$ field rotates about z-axis, from pointing along x-axis to ending along y-axis in time, $t \in [0, T]$. The C^∞ conditions impose all derivatives of $\overrightarrow{B}(t)$ to vanish at end points, i.e. at $t = 0, T$. Since the time dependence just involves rotation of the $\overrightarrow{B}$ field, it can be captured by an angular variable. Specifically, consider

$$\theta(s) = \frac{\pi \int_0^s ds' e^{-1/[s'(1-s')]}}{2 \int_0^1 ds' e^{-1/[s'(1-s')]}}, \quad s \in [0, 1] \tag{2.5}$$

where s is the dimensionless time parameter,

$$s \equiv t/T. \tag{2.6}$$

The coupling field is given by

$$
\begin{aligned}
B_x &= \begin{cases} \cos(\theta(s)), & 0 \leq s < 1 \\ 0, & 1 \leq s < 2 \\ \sin(\theta(s-2)), & 2 \leq s \leq 3 \end{cases} \\
B_y &= \begin{cases} \sin(\theta(s)), & 0 \leq s < 1 \\ \cos(\theta(s-1)), & 1 \leq s < 2 \\ 0, & 2 \leq s \leq 3 \end{cases} \\
B_z &= \begin{cases} 0, & 0 \leq s < 1 \\ \sin(\theta(s-1)), & 1 \leq s < 2 \\ \cos(\theta(s-2)), & 2 \leq s \leq 3. \end{cases}
\end{aligned} \tag{2.7}
$$

The three components of the coupling $\overrightarrow{B}(t)$ (i.e. B_x, B_y and B_z) are plotted as a function scaled-time for s in the Fig. 2.1. Note that for each drive-sequence all time-derivatives of $\overrightarrow{B}$ vanish at the end points owing to functional form of θ given in Eq. 2.5.

Next, we couple our system to a Bosonic bath and introduce the master equation governing the dynamics of density matrix of the system.

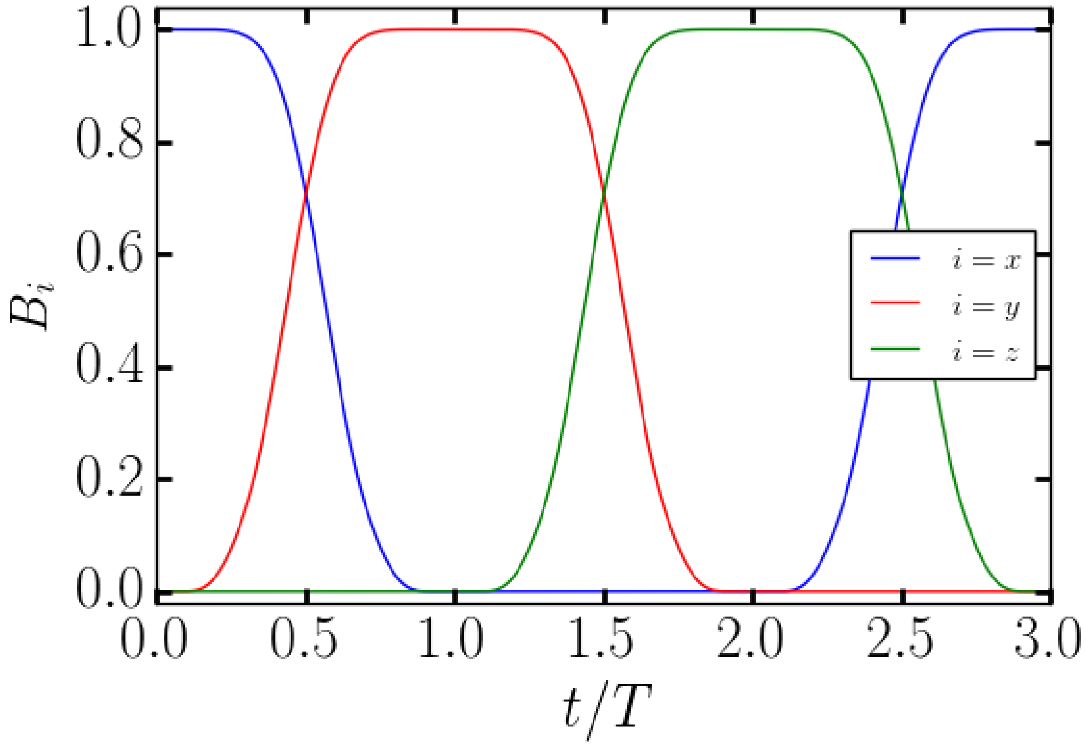

FIGURE 2.1: Plot of different components of Majorana coupling field (B_i ; $i \in \{x, y, z\}$) appearing in Eq. 2.1 as a function of scaled-time for $s = t/T$ as described by Eq. 2.7

2.1.2 Master Equation

We couple the system to a thermal Bosonic bath and allow for the most general parity-conserving system-bath interaction. In the previous section we showed that as a consequence of parity conservation, the dynamics under the influence of the braiding Hamiltonian (Eq. 2.3) is captured by a two-level Hamiltonian (Eq. 2.4). We expect a similar simplification to hold for the master equation provided the system, the bath and system-bath interaction preserves parity. This is indeed the case as discussed in Appendix A. Therefore, henceforth in the manuscript we solely use on Eq. 2.4 to describe the system Hamiltonian in lieu of Eq. 2.3.

Following the prescription introduced by Davies [73] we assume weak system-bath coupling (*Born* approximation) and that the bath is memory-less (*Markov* approximation). The memory-less assumption means that the time scales of interest are much larger than time scales over which bath correlations decay. With the above assumptions, the master equation can be expressed in the *Lindblad* form, i.e. as a time-local differential equation that preserves positivity of the density matrix [73, 74]. Let the total Hamiltonian describing a system interacting with a Bosonic bath be written as,

$$H_T = H_{2level} + H_{SB} + H_B, \tag{2.8}$$

where H_{2level}, H_B, H_{SB} are system Hamiltonian, Bosonic-bath Hamiltonian and Hamiltonian describing system-bath coupling, respectively. Let the system-bath Hamiltonian be given by,

$$H_{SB} = \sum_k \hat{A}_k \hat{\Gamma}_k, \tag{2.9}$$

where $\hat{A}_k$ and $\hat{\Gamma}_k$ are system and bath operators, respectively, satisfying $\hat{A}_k^\dagger = \hat{A}_k$ and $\hat{\Gamma}_k^\dagger = \hat{\Gamma}_k$. Represent the projection operator to an eigenspace spanned by eigenstates of H_S with eigenvalues e by $\Pi(e)$. Define

$$J_k(\nu) \equiv \sum_{e'-e=\nu} \Pi(e)\hat{A}_k\Pi(e'), \tag{2.10}$$

where, the sum runs over all energy eigenvalues e and e'. With this definition it follows that

$$\begin{aligned} [H_{2level}, J_k(\nu)] = -\nu J_k(\nu); \quad [H_{2level}, J_k^\dagger(\nu)] = \nu J_k(\nu) \\ [H_{2level}, J_k^\dagger(\nu)J_k(\nu)] = 0; \quad J_k^\dagger(\nu) = J_k(-\nu) \end{aligned} \tag{2.11}$$

and

$$\sum_{\nu} J_k(\nu) = \hat{A}_k$$
$$\implies H_{SB} = \sum_{k,\nu} J_k(\nu)\hat{\Gamma}_k. \tag{2.12}$$

Clearly, the jump-operators induce transitions among the energy levels of the system Hamiltonian. For a two-level system the *jump operators* generically act as agents of

- Excitation: transitioning the system from the ground state to the excited state.
- Relaxation: transitioning the system from the excited state to the ground state.
- Dephasing: system decoheres neither gaining nor loosing energy.

Note that the *jump operators* are time dependent, where the time dependence is inherited from the time-dependence of $\Pi(e)$ (projection operator is time-dependent because H_{2level} is time-dependent) and $\hat{A}_k$ operators in Eq. 2.10. Thus, let us denote the *jump operators* by $J_k^{\nu}(t)$, where time dependence is shown explicitly. Using Eq. 2.12, the master equation within the Born-Markov approximation reduces to,

$$\dot{\rho}_S(t) = -i[H_{2level}, \rho_S(t)] + \mathcal{D}(\rho_S(t)), \tag{2.13}$$

where,

$$\mathcal{D}(\rho_S(t)) = \sum_{\nu,i} J_i^{\nu}(t)\rho(t)J_i^{\nu\dagger}(t)\eta_i(\nu) - \frac{1}{2}\eta_i(\nu)\{J_i^{\nu}(t)^{\dagger}J_i^{\nu}(t), \rho_S(t)\}, \tag{2.14}$$

with $\eta_k(\nu) = \mathrm{Re}\int_{-\infty}^{\infty} ds e^{-i\nu s}\left\langle \hat{\Gamma}_k^{\dagger}(s)\hat{\Gamma}_k(0)\right\rangle$, where, $\langle\cdots\rangle$ stand for $\mathrm{tr}_B(\cdots\rho_B)$.

Now we specify the system-bath coupling. Let $\hat{A}_i = s_i B_i \sigma_i$ in Eq. 2.9, where, s_i, B_i, σ_i is the coupling-strength, i^{th} component of $\overrightarrow{B}$ and the i^{th} Pauli matrix, respectively for $i \in \{x, y, z\}$. This form of system-bath coupling ensures that the bath-induced relaxation and excitation vanish whenever two Majoranas are decoupled in the braiding scheme (this happens whenever $\overrightarrow{B}$ is parallel to either x, y or z axis, e.g. when $\overrightarrow{B} = \hat{x}$, γ_y and γ_z are free). Using Eq. 2.10, *jump operators* are expressed as ,

$$\begin{aligned} J_i^{\nu}(t) &= s_i a_i(t) B_i(t) |1(t)\rangle\langle 0(t)|; \quad J_i^{-\nu} = J_i^{\nu\dagger} \\ J_i^{\nu=0} &= s_i B_i(t)(a_i^0(t)|0(t)\rangle\langle 0(t)| + a_i^1(t)|1(t)\rangle\langle 1(t)|), \end{aligned} \tag{2.15}$$

where

$$\begin{aligned} a_i(t) &= \langle 1(t)|\sigma_i|0(t)\rangle \\ a_i^0(t) &= \langle 0(t)|\sigma_i|0(t)\rangle \\ a_i^1(t) &= \langle 1(t)|\sigma_i|1(t)\rangle, \end{aligned} \tag{2.16}$$

s_i being the time-independent system-bath coupling strength with $i \in \{x, y, z\}$ and $|0\rangle$ and $|1\rangle$ denote the ground and the excited state, respectively.

We wish to focus on only those bath effects that arise due to time dependence of the Hamiltonian. In other words we want to explicitly avoid any bath-induced effect that does not vanish in the adiabatic limit, provided the system is initialized in the ground state. The only such environmental effect is thermal excitation associated with $J^{\nu=2}$ (energy gap above ground state is 2 for $||\overrightarrow{B}|| = 1$) operator. We explicitly set temperature to zero to completely suppress these thermal excitations or equivalently set the *jump operator* coefficient η (see Eq. 2.14) with excitation energy $\nu = 2$,

$$\eta(\nu = 2) = 0. \tag{2.17}$$

Since the braiding process involves a sequence of three identical clockwise $\pi/2$ rotations of $\overrightarrow{B}$ along $\hat{z}, \hat{x}$ and $\hat{y}$, axes respectively, as shown in Fig. 1.4, we focus on the first sequence, where $\overrightarrow{B}$ is restricted to XY plane without loss of generality, setting $B_z = 0$. The influence of the bath is captured by the strength of the system-bath couplings (captured by s_x and s_y), the relaxation strength governed by $\eta(\nu = -2)$ (since the gap in the system is 2) and dephasing strength governed by $\eta(\nu = 0)$. Since the time-dependence of the Hamiltonian does not affect the gap in the system $\eta(\nu = -2)$ and $\eta(\nu = 0)$ are fixed parameters determined by entirely by the microscopic properties of the bath Hamiltonian. Henceforth, for the sake of brevity, we relabel the relaxation strength, $\eta(\nu = -2)$ and the dephasing strength, $\eta(\nu = 0)$ with new symbols, $\eta(\nu = -2) \equiv \eta$ and $\eta(\nu = 0) \equiv \eta_0$.

2.1.3 Bloch equation

The master equation (Eq. 2.13) describing the time evolution of ρ_S (which is a density matrix of a two-level system) can be exchanged in favor of a differential equation describing time evolution of the vector $R \equiv (r_x, r_y, r_z)$ defined by

$$\rho_S(t) = \frac{1}{2}[r_x(t)\sigma_x + r_y(t)\sigma_y + r_z(t)\sigma_z + \mathbb{1})] \tag{2.18}$$

The resulting Bloch equation, in terms of the scaled time parameter (Eq. 2.6), is given by,

$$\epsilon\dot{\overrightarrow{R}} = 2[\overrightarrow{B} \times \overrightarrow{R} + (\alpha - \beta)\overrightarrow{B} \times (\overrightarrow{B} \times \overrightarrow{R}) - 2\beta(\overrightarrow{B} + \overrightarrow{R})] \tag{2.19}$$

where,

$$\begin{aligned} \beta(s) &= \frac{1}{4}F(s)\eta; \quad \text{(effective relaxation)} \\ \alpha(s) &= F^0(s)\eta_0; \quad \text{(effective dephasing)} \end{aligned} \tag{2.20}$$

with,

$$\begin{aligned} F &= s_x^2 B_y^2(s) B_x^2(s) + s_y^2 B_x^2(s) B_y^2(s) \\ F^0 &= s_x^2 B_x^4(s) + s_y^2 B_y^4(s) \end{aligned} \tag{2.21}$$

and $\epsilon = 1/T$. Equivalently, the Bloch equation can be expressed as,

$$\epsilon\frac{d}{ds}R = MR + 4\beta(R_0 - R) \tag{2.22}$$

with, $R_0(s) \equiv -\overrightarrow{B}(s)$ being a null vector of M, $M = 2(A + S)$ and $S = (\alpha - \beta)A^2$, where

$$A = \begin{pmatrix} 0 & 0 & B_y \\ 0 & 0 & -B_x \\ -B_y & B_x & 0 \end{pmatrix} \tag{2.23}$$

2.2 Adiabatic expansion for Bloch Equation

We focus on the first sequence of the braiding process and calculate the diabatic error incurred in the process which involves rotating $\overrightarrow{B}$ along $\hat{z}$ axis by $\pi/2$ in the clockwise direction from the initial orientation along $\hat{x}$ to final orientation along $\hat{y}$. The system is initialized in the ground state of H_{2Level} to which the corresponding Bloch vector is $R(s=0) = -\overrightarrow{B}(s=0) = (-1,0,0)$. For $\epsilon = 0$,

$$R(s) = R_0(s) \tag{2.24}$$

is the solution to the Bloch equation consistent with the initial condition. Clearly, for small but finite ϵ, the solution to the Bloch equation can be expressed as an ϵ-dependent correction to R_0. Since the system is initialized with $R(0) = R_0(0)$, let us call its time-evolution $R(s)$ (satisfying the Bloch equation), the *time-evolved Bloch zero-vector* (TBZV). Given that $R(0) = R_0(0)$, the diabatic error $\mathcal{E}$ is defined as the deviation of TBZV, R from the vector R_0 corresponding to the instantaneous ground state of H_{2Level} at the end of the diabatic drive at $s = 1$,

$$\mathcal{E} \equiv \|R(1) - R_0(1)\|. \tag{2.25}$$

We now show that the Bloch vector $R(s)$, can be solved perturbatively in powers of ϵ in the absence of relaxation (Eq. 2.20), $\eta = 0$. We defer our analysis for finite relaxation to Sec. 2.4. The equation of motion for R in absence of relaxation (but potentially finite dephasing) is written as

$$\epsilon\dot{R} = MR. \tag{2.26}$$

This equation can be solved by a power series ansatz,

$$R(s) = R_0(s) + \epsilon R_1(s) + \epsilon^2 R_2(s) \dots \tag{2.27}$$

Substituting the above ansatz in Eq. 2.26 and equating both sides of the equation at each order in ϵ, we formally solve for j^{th} order correction to $R_0(s)$ for $R(s)$ (see App. B for details),

$$R_j = f_{j-1} R_0 + M^{-1} \dot{R}_{j-1}, \tag{2.28}$$

with $f_{j-1}(s)$ given by

$$f_{j-1}(s) = \int_0^s ds\ \dot{R}_0^T M^{-1} \dot{R}_{j-1}. \tag{2.29}$$

The convergence of the series for R_j is shown in App. B.

Before discussing the solution to Bloch's equation in presence of system-bath coupling contributing finite dephasing, we pause to study a limiting case. We study our system in absence of system-bath coupling, $\eta = \eta_0 = 0$ (consequently $\alpha = \beta = 0$), described by the the Bloch equation (Eq. 2.22). Note that in this limit, Eq. 2.26 reduces to $\epsilon \dot{R} = 2AR$. Therefore, in this limit we use Eq. 2.27 and 2.28 to compute a convergent power-series of R provided we set $M = 2A$. By considering the power-series to any power of epsilon, we can show an error bound related to the residual terms (Eq. B.16 in App. B),

$$\begin{aligned} \mathcal{E} \equiv \|R(1) - R_0(1)\| \leq 2\epsilon^M \int_0^1 ds' \left\| \dot{R}_M \right\| \\ \implies \mathcal{E}(\epsilon)/\epsilon^n = 0\ as\ \epsilon \to 0 \forall n \in \mathbb{N}. \end{aligned} \tag{2.30}$$

This result suggests an exponential dependence of $\mathcal{E}$ on total diabatic time T. In Fig. 2.2, we obtain $\mathcal{E}$ as a function T by numerically solving Eq. 2.22 for $\eta = \eta_0 = 0$. Furthermore, the numerical result obtained here illustrates the precise dependence of $\mathcal{E}$ on T,

$$\mathcal{E} = \|R(1) - R_0(1)\| \sim e^{-\sqrt{T}}. \tag{2.31}$$

This is completely consistent with the analytical result in Eq. 2.30, originally derived in Ref. [76], which suggests an exponential-like dependence of diabatic error $\mathcal{E}$ on T. In the remaining sections we consider how this error $\mathcal{E}$ is modified in the presence of a bath.

2.3 Purely decohering system-bath coupling

Consider the case of vanishing relaxation, $\eta = 0$ (consequently $\beta = 0$) but finite dephasing $\eta_0 \neq 0$. The Bloch vector $R(s)$ is solved using the identification $M = 2(A+\alpha A^2)$ in Eq. 2.28. As shown in App. B, the smoothness criterion on the diabatic drive that translates to all derivatives of M vanishing at $s = 1$ can be exploited to show $R(1) \parallel R_0(1)$ up to exponentially small deviations of the order $e^{-\sqrt{T}}$ (this precise exponential dependence follows from the numerical result of the previous section). This together with unitarity was sufficient to constrain the result for the isolated system. However, in the presence of decoherence one needs to consider the change in magnitude of $R(1)$. Projecting $R(1)$ on $R_0(1)$ (see Eq. 2.28) gives

$$R(1) = f^{\beta=0}(1)R_0(1) \tag{2.32}$$

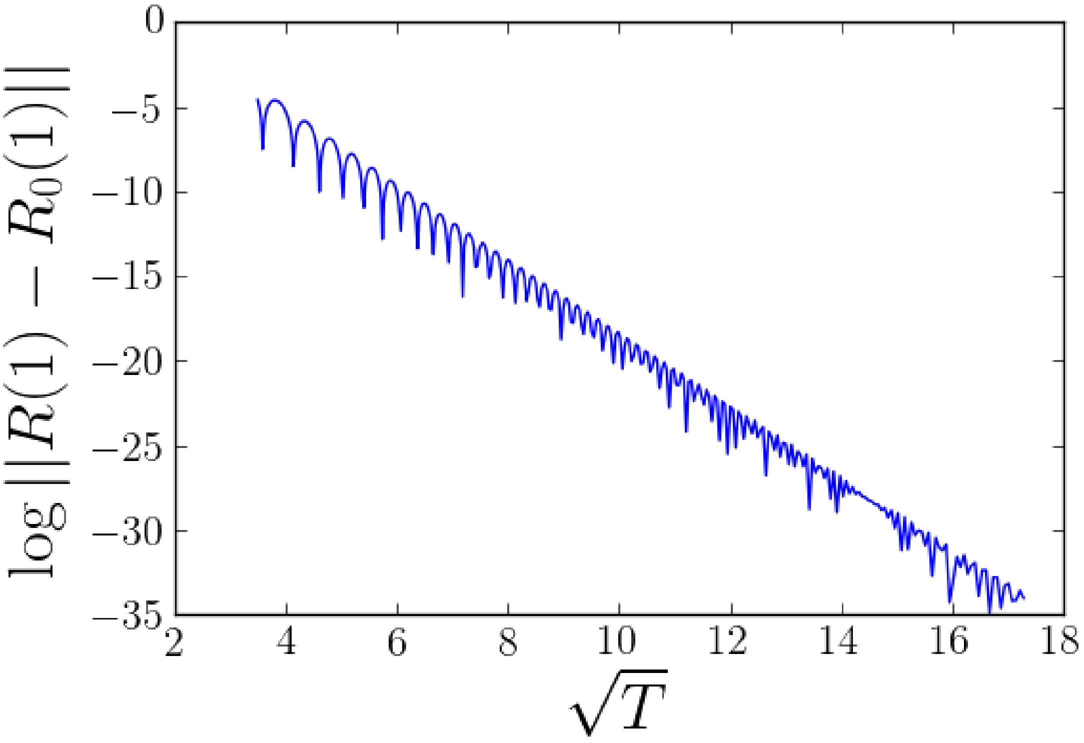

FIGURE 2.2: Numerical plot of log of norm of difference between time evolved and instantaneous Bloch zero-vector at scaled time $s = 1$ as a function of $\sqrt{T}$ for strength $s_x = s_y = 0$ obtained using Eq. 2.22. The system is initialized in the ground state of H_{2Level} or equivalently the initial value of $R(s = 0)$ in the Bloch equation is set as $R_0(0) = -\overrightarrow{B}(0)$. The plot shows exponential decay in $\mathcal{E}$ as a function of total time T when system-bath coupling is zero consistent with the result derived in Appendix B. Specifically, $\mathcal{E} = \|R(1) - R_0(1)\| \sim e^{-\sqrt{T}}$.

where $f^{\beta=0}(1) \equiv f(s=1)|_{\beta=0}$ is given by a series expansion

$$f(s) = 1 + \epsilon f_0(s) + \epsilon^2 f_1(s) + \dots\,, \tag{2.33}$$

and $f_j(s)$ is evaluated using Eq. 2.29 assuming $\beta = 0$. We now compute the diabatic error:

$$\mathcal{E} = \|R_0(1)\| \left|(1 - f^{\beta=0})\right| \approx -\epsilon f_0^{\beta=0}(1), \tag{2.34}$$

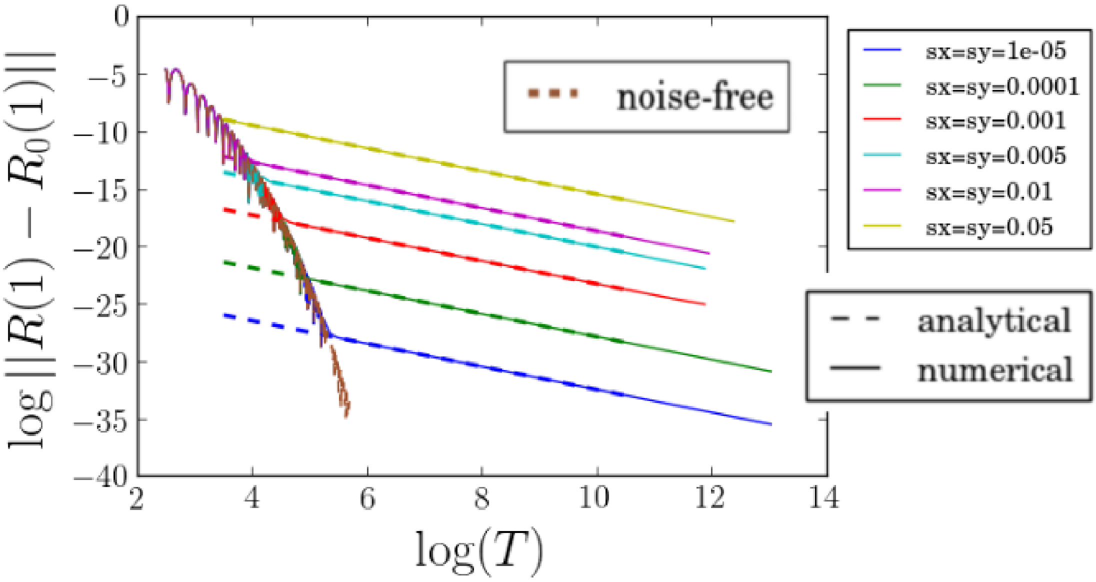

FIGURE 2.3: Plot of $\mathcal{E}$ as a function of time T for different values of effective dephasing strength α characterized by values of $s_x = s_y$ and absence of effective relaxation, $\beta = 0$ (see Eq. 2.20). Relaxation and dephasing parameters, η and η_0, that solely depend on bath Hamiltonian are both set to $\eta = \eta_0 = 1$. The solid line is obtained by solving the Bloch equation (Eq. 2.26) and is compared against (dashed curve) theoretical bound given by Eq. 2.34,2.35, i.e., dashed curve is calculated value of $\log[(1/T)f_0^{\beta=0}(1)]$ using the expression given in Eq. 2.35. The low-T region characterized by the oscillatory section of the curves are independent of system-bath coupling strength and follows closely the numerical values obtained by solving the Bloch equation (Eq. 2.22) in absence of bath denoted by the dashed-brown-colored curve.

where using Eq. 2.29 one can calculate

$$f_0^{\beta=0}(1) = -\int_0^1 \frac{\alpha\omega^2}{2(1+\alpha^2)} \tag{2.35}$$

Note that this term (as well as the other powers of ϵ) would vanish in the absence of a bath ($\alpha = 0$), restoring the exponential estimate in the previous section.

In Fig. 2.3, we plot $\log \epsilon |f_0^{\beta=0}(1)|$ as a function of $\log(T)$ for different system-bath coupling strengths and compare it to the numerical curve obtained by solving Eq. 2.26.

We find that numerically exact calculation of $\mathcal{E}$ is well captured (in the asymptotic limit of large T) by the approximate diabatic error (Eq. 2.34) obtained for truncation at first-order in ϵ, as Fig. 2.3 clearly shows. The small-T region is marked by the highly oscillatory section of the curves, where $\mathcal{E}$ appears to be independent of the system-bath coupling strength, as evidenced by complete overlap of the curves in the oscillatory region. Indeed, this is precisely the exponential behavior obtained in the absence of a thermal bath. For a given system-bath coupling strength, the transition from an exponential behavior to a power-law occurs rather abruptly at the intersection of the curve representing $\log \mathcal{E}$ calculated in absence of bath (using Eq. 2.31) and the curve representing analytically calculated diabatic error for purely decohering bath given by the logarithm of the formula in Eq. 2.34.

2.4 General system-bath coupling

We now consider the error $\mathcal{E}$ in the presence of finite relaxation. In order to solve for R in Eq. 2.19 for the case of finite β, we switch to a new vector-variable $\overrightarrow{\Pi}$,

$$R(s) = U_0(s)(-\hat{x} + \overrightarrow{\Pi}(s)) \tag{2.36}$$

where $U_0(s)$ is the rotation matrix such that $R_0(s) = U_0 R_0(0)$ ($R_0(0) = -\hat{x}$ being the initial condition on R) given by

$$U_0 = \begin{pmatrix} \cos\theta & \sin\theta & 0 \\ -\sin\theta & \cos\theta & 0 \\ 0 & 0 & 1 \end{pmatrix}. \tag{2.37}$$

From Eq. 2.36 it follows, the initial condition on $\Pi(s)$ is $\Pi(0) = (0, 0, 0)$. Since $R_0(s)$ is the solution to the Bloch equation in $\epsilon \to 0$ limit, $\Pi(s)$ must have perturbatively small norm in ϵ.

The equation of motion for $\Pi(s)$ is found to be

$$\epsilon\left(\dot{\overrightarrow{\Pi}} + \dot{\theta}\hat{z} \times \overrightarrow{\Pi} - \dot{\theta}\hat{y}\right) = 2\hat{x} \times \overrightarrow{\Pi} + 2(\alpha - \beta)\hat{x} \times (\hat{x} \times \overrightarrow{\Pi}) - 4\beta\overrightarrow{\Pi}. \tag{2.38}$$

On the right hand side of the equation, the operator acting on Π can be diagonalized along the basis unit vectors $\{\hat{x}, \hat{j}_+, \hat{j}_-\}$ with $\{-4\beta, 2\lambda_+, 2\lambda_-\}$ being the corresponding eigenvalues where we have defined,

$$\hat{j}_\pm = \frac{1}{\sqrt{2}}(\hat{y} \pm i\hat{z}) \tag{2.39}$$

$$\lambda_\pm = \mp i - (\alpha + \beta). \tag{2.40}$$

Representing $\overrightarrow{\Pi}$ in this basis set,

$$\overrightarrow{\Pi} = \pi_x\hat{x} + \pi_+\hat{j}_+ + \pi_-\hat{j}_- \tag{2.41}$$

leads to the following coupled-differential-equation,

$$\epsilon\left[\dot{\pi}_x - \frac{\dot{\theta}}{\sqrt{2}}(\pi_+ + \pi_-)\right] = -4\beta\pi_x \tag{2.42a}$$

$$\epsilon\left[\dot{\pi}_\pm + \frac{\dot{\theta}}{\sqrt{2}}\pi_x - \frac{\dot{\theta}}{\sqrt{2}}\right] = 2\lambda_\pm\pi_\pm \tag{2.42b}$$

Now, to lowest order in ϵ,

$$\pi_\pm \approx -\frac{\dot{\theta}\epsilon}{2\sqrt{2}\lambda_\pm}. \tag{2.43}$$

This implies $\pi_+(1) = \pi_-(1) \approx 0$ as $\dot{\theta}|_{s=1} = 0$ (see Eq. 2.5). Therefore, we conclude $\mathcal{E} = \|R(1) - R_0(1)\| \approx \pi_x(1)$. Substituting $\pi_\pm$ expressions in Eq. 2.42a, it can be solved for π_x resulting in

$$\mathcal{E} \simeq \pi_x(1) = -\epsilon \int_0^1 \dot{f}_0 e^{-\frac{4}{\epsilon}\int_s^1 \beta ds'} ds. \tag{2.44}$$

where we have defined

$$f_0(s) = -\int_0^s \frac{(\alpha+\beta)\dot{\theta}^2}{2(1+(\alpha+\beta)^2)}. \tag{2.45}$$

The behavior of $\mathcal{E}$ in the large-T limit is analyzed using the saddle-point method detailed in the App. C to obtain the following asymptotic form for the diabatic error,

$$\mathcal{E} \sim e^4 T^{-2}. \tag{2.46}$$

Note that Eq. 2.44 reduces to Eq. 2.34 in absence of relaxation, i.e. $\beta \to 0$, showing that the approach in this section is not inconsistent with that in the previous section for the case without relaxation. An examination of the exponential factor in Eq. 2.44 tells us that for the case where relaxation is weak compared to dissipation (i.e. $\beta \lesssim \alpha$), we should expect an intermediate regime of ϵ where β might still be ignored so that the error would scale as $\mathcal{E}(T) \sim T$ as concluded in the previous section.

Therefore as T is increased we expect the error rate $\mathcal{E}$ to crossover from the isolated system limit (Eq. 2.31) to the dominantly dissipative system(Eq. 2.34) to the asymptotics with relaxation (Eq. 2.46). The numerical plot of the error rate $\mathcal{E}$ in the general case, Fig. 2.4 indeed shows this expected pattern of crossovers. These expectations turn out to be quite accurate as seen from the numerical simulations in Fig. 2.4, which shows the numerical estimate of $\mathcal{E}$ vs total time T in log-log scale for dephasing strength η_0, and relaxation strength η, both set equal to 1. It is interesting that the crossover behavior expected for the limit $\eta_0 \gg \eta$ seems to apply even to $\eta_0 = \eta = 1$ chosen for Fig. 2.4. Finally, we see in Fig. 2.4 that as we decrease the bath coupling strength $s_x \sim s_y$, the crossover scale modes to higher T as expected. While Eq. 2.45 predicts the correct crossover behavior, it turns out to be off by a T-independent scale factor in the pre-asymptotic dissipation dominated regime. We have remedied this by adapting the analysis in Sec. 2.2 to finite (but small η) as described in App. C. This analysis leads to a somewhat different approximation for $f_0(s)$ which is written as

$$f_0(s) = -\int_0^s \frac{(\alpha - \beta)\dot{\theta}^2}{2(1 + (\alpha - \beta)^2)}. \tag{2.47}$$

This more exact theoretical form, which is the analytic approximation used in the dashed lines in Fig. 2.4, can be seen from the figure to fit the numerical results very well in both the dissipative and relaxation dominated regimes.

2.5 Summary

In this chapter we have studied the diabatic error rate $\mathcal{E}(T)$ as a function of braiding time T (in units of inverse gap) of the Y-junction braiding protocol (shown in Fig. 1.4) by mapping it to the problem of excitation probability of a spin in a time-dependent magnetic field. Consistent with previous work [76] we find (see Eq. 2.31) that one can reduce diabatic errors [62] to be exponentially (scaling as $\mathcal{E}(T) \sim e^{-\sqrt{T}}$) small in the braiding time T (in units of inverse gap) by choosing the time-dependence of the Hamiltonian to be completely smooth (including the beginning and end of the protocol). This analytic result can be considered an explanation of recent obeservation of exponentially suppressed diabatic errors apparent from numerical simulation of some

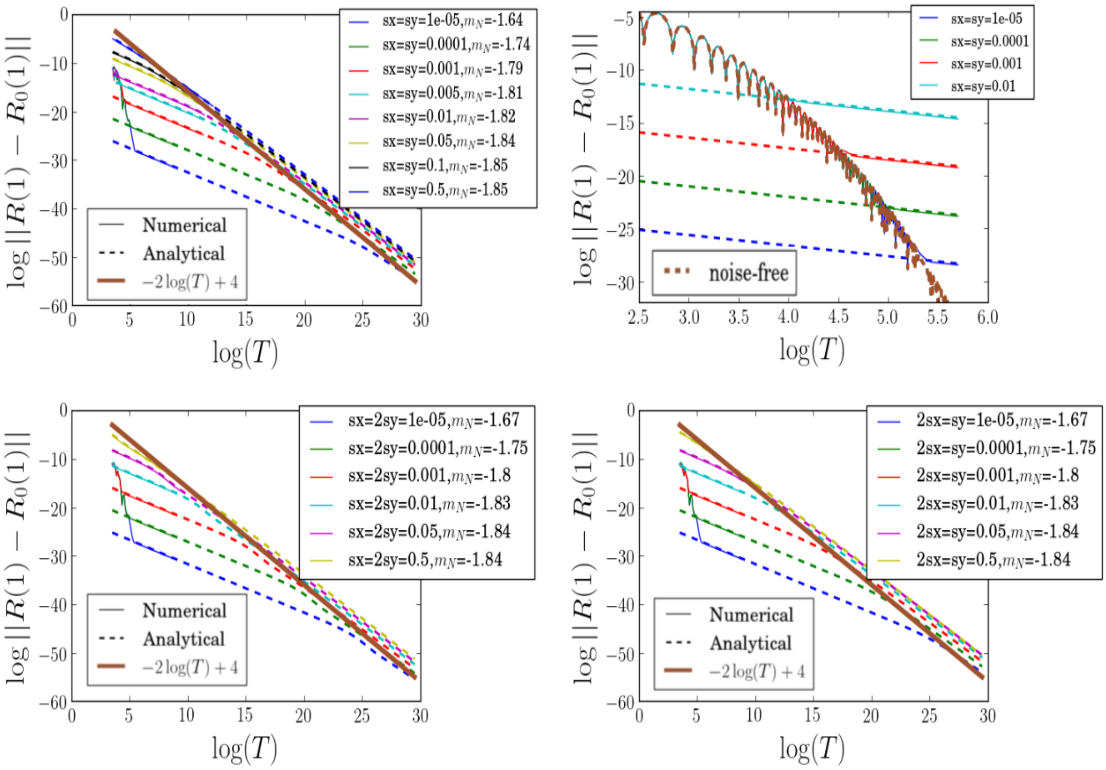

FIGURE 2.4: (Top left) Plot of $\mathcal{E}$ as a function of total-time taken by the diabatic drive T for different values of effective dephasing, α and relaxation strength, β characterized by the shown values of $s_x = s_y$ (see Eq. 2.22-2.21). Relaxation and dephasing parameters, η and η_0, that solely depend on bath Hamiltonian are both set to $\eta = \eta_0 = 1.$ for all panels in this figure. For each set of parameters, the analytical curve (dashed line) is obtained by plotting the expression in Eq. 2.44 with f_0 given by Eq. 2.47 and the numerical curve (solid line) is obtained by numerically solving the Bloch equation in Eq. 2.22. The slope m_N (given in legend) is calculated using the data in the neighborhood of log(T) = 29.5 on the X axis for each curve. The asymptotic dependence on T is given by e^4T^{-2} (Eq. 2.46), represented in the figure by the solid (thick) brown curve. (Top right) Magnified view of the top left panel in the small-T-region. The values obtained for the special case of zero dephasing and relaxation is plotted using (thick) brown dashed curve. For each coupling strength and sufficiently small values of T, the $\mathcal{E} = \log(R(1)x)$ behavior is independent of system bath coupling strength and is well captured by the exponential dependence on T (see Fig.2.2). The abrupt change from the exponential to a polynomial dependence on T occurs when the analytic estimate of $\mathcal{E}$ coincides with its value under zero system-bath coupling assumption. (Bottom panels) Similar to the top panels, log norm of difference between time evolved and instantaneous Bloch vector at scaled time $s = 1$ $(t/T \mod 3 = 1)$as a function of log of total time T. However, unlike the top panels $s_x = 2s_y$ and $s_y = 2s_x$ for bottom left and right panels respectively. The qualitative behavior is similar to ones observed in the top panels.

braiding protocols [18]. In fact, while the requirement of a completely smooth time-dependent Hamiltonian of the form of Eq. 2.3 (also see Eq. 2.7) seems fine-tuned as we demanded the diabatic drive to be perfectly smooth, it is quite natural in a topoogical system where MZM splitting is tuned either by chemical potential [17, 18, 77] or by Coulomb energy through tunable Josephson junctions [78, 79]. In both these cases, the tunneling is exponentially suppressed as one tunes the Majorana wire deep into the topological phase or introduces a strong Josephson coupling between the Majorana wire and a bulk superconductor. The main focus in this chapter is to consider the effect of a Fermion parity conserving Bosonic bath, such as phonons or plasmons on the diabatic error rate for braiding. Similar to previous work [63], we assume the bath to be weakly coupled so that we can treat the bath within the Markovian approximation. We describe the dynamics of this system within the Markovian approximation by a Bloch equation. We find that the coupling to such a Bosonic bath generically changes the asymptotic of the diabatic error from exponential in the braiding time T to power law (i.e. error scaling as $\mathcal{E}(T) \sim e^4 T^{-2}$ (see Eq. 2.46). More specifically the analytic derivation of this result (see Sec. 2.4) applies in the limit of weak relaxation. Interestingly, as expected, the general result including relaxation leads to much lower excited state state probability then in the absence of relaxation. We find from a controlled analytic solution that the error rates in the presence of dephasing from the bath but no relaxation decreases the slowest scaling as $\mathcal{E}(T) \sim T^{-1}$.

In addition to the asymptotic forms we study the dependence of the diabatic error rate on the system-bath coupling strength through direct numerical simulations. For purely dephasing bath (i.e. no relaxation), we find (see Fig. 2.3) that the dephasing strength determines the cross-over from the $e^{-\sqrt{T}}$ scaling error rate that is expected in the absence of a bath to the T^{-1} scaling of the error rate expected for a purely dephasing bath. Increasing the dephasing strength leads to the crossover occuring at shorter braiding time T, in turn leading to error rates that increase with increasing dephasing. As seen from our results in Fig. 2.4, adding weak relaxation in addition to dephasing leads to an additional relaxation strength dependent cross-over time-scale beyond which the error rate $\mathcal{E}(T)$ changes its scaling from T^{-1} to $\mathcal{E}(T) \sim e^4 T^{-2}$.

Chapter 3: Non-Abelian statistics and topological invariants from tunneling conductance properties.

In this chapter we study the interplay of Majorana splitting present in the topological regime due to the finite size of the nanowire and dissipation that must invariably be present in any realistic Majorana nanowire experiment. We define a quantity- 'topological visibility' (TV) to diagnose the topological nature of such split Majorana modes in presence of dissipation. We explore the connection between conductance and the TV and calculate their dependence on the Majorana splitting and the energy gap. We posit that TV is a measure of the success of observing non-Abelian statistics in a braiding experiment using such split Majorana modes where the speed of the braiding plays the role of phenomenological dissipation that we introduce. We connect the outcome of a braiding experiment in relation to the measurement of the tunneling conductance in the same sample, answering the question whether a given value of a measured (in our case, numerically) ZBCP value is consistent or not with a topological value for the (numerically calculated) TV. In general, the non-Abelian character in a Majorana braiding experiment will be observed for fast enough braiding operation so that the energy uncertainty associated with the braiding time is larger than the Majorana splitting, which will entail approximate Majorana modes to appear to be roughly degenerate (as opposed to being well-split). However the experiment must distinguish the Majorana modes from the continuum set of (above-gap) bulk states. Therefore, the braiding operation should be slow with respect to the inverse topological gap, but fast compared with the Majorana splitting. We argue that this is in complete analogy to how dissipative broadening, which is likely present in a tunneling conductance set-up, must be larger than Majorana splitting but smaller than the topological gap to realize a nearly quantized conductance

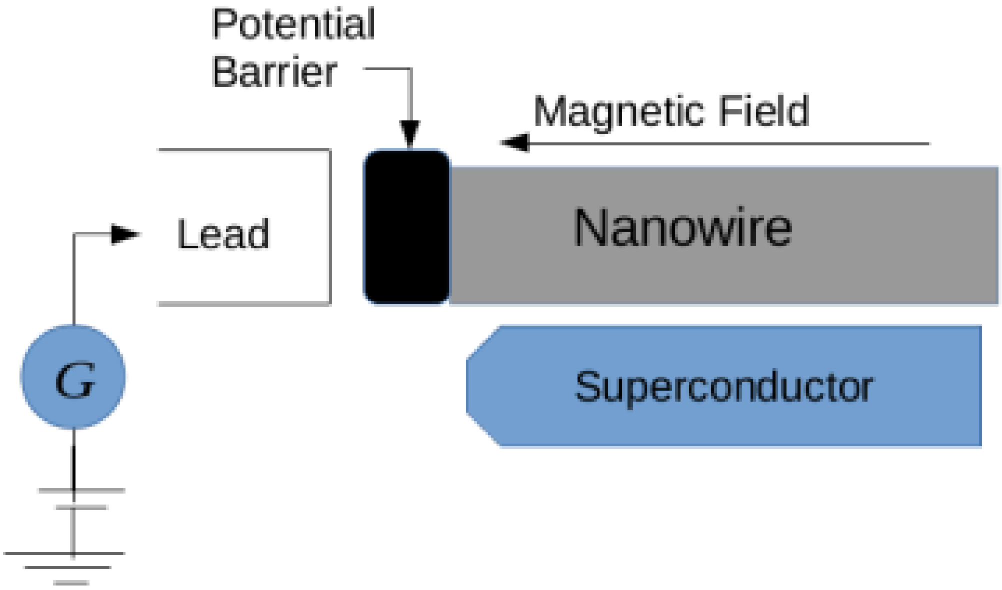

FIGURE 3.1: A schematic diagram for measuring the tunneling conductance. One end of the Rashba nanowire is shown attached to a normal lead. The lead is connected to the nanowire through a potential barrier. The magnetic field is parallel to the nanowire. A proximate s-wave superconductor is responsible for the superconducting order parameter in the nanowire.

peak and also a topologically non-trivial value for the TV. These effects are studied for a specific Majorana hosting semiconductor Rashba nanowire (e.g. InSb or InAs nanowire with strong Rashba spin-orbit coupling) model proposed by Lutchyn *et al.* and Oreg *et. al.* [26, 29]. We study the competition between the strength of dissipation and the finite size splitting of Majorana modes. First, we establish the quantitative connection between having a ZBCP strongly suppressed from the quantized $2e^2/h$ value and the topological content of the associated almost-MZMs. Second, we investigate the deleterious effects of MZM splitting on the braiding properties (or more precisely, on the value of the TV which distinguishes topological and trivial phases).

3.1 Model Hamiltonian

A schematic representation for an experimental setup to measure tunneling conductance is shown in Fig. 3.1. A semiconductor nanowire with Rashba spin-orbit coupling (SOC) is attached to a normal lead through a potential barrier localized at the end. A magnetic field is applied parallel to the wire (perpendicular to the SOC direction) and an s-wave superconductor is placed in proximity to the nanowire to facilitate Cooper pair tunneling into the semiconductor effectively endowing the nanowire with an s-wave superconducting order parameter through proximity coupling. A voltage bias V is applied to the lead, and the tunneling current I is measured to obtain the differential conductance

$$G = dI/dV. \tag{3.1}$$

As discussed in more detail in the App. D, for N conducting channels in the lead, the conductance G can be computed from the normal reflection matrix r_{ee} and the Andreev reflection matrix r_{eh} through the relation,

$$G = N - \mathrm{Tr}(r_{ee}r_{ee}^{\dagger} - r_{eh}r_{eh}^{\dagger}) \tag{3.2}$$

To characterize the topological phase we can not use the usual definition of the topological invariant (TI) $Q_0 = \mathrm{sgn}[\det(r)]$, where r is the reflection matrix from the end, because it requires us to ignore transmission of quasiparticles in-between the ends of the wire [25, 56, 80]. Such transmission of quasiparticles always exist for the finite wires we consider in this chapter. In fact, as we will discuss in more detail, for finite wires the TI Q_0 is always trivial when one uses the exact reflection matrix (as opposed to the effectively semi-infinite approximation used in Refs. [25, 56]). Instead of ignoring transmission across the wire, we circumvent this problem by introducing dissipation into the system. While some form of dissipation has been important in previous calculations of the scattering matrix TI [56, 80], dissipation for our purpose here represents the finite rate of braiding. As pointed out in previous works [53, 81] dissipation can change the qualitative behavior of Majorana modes and the TI. The standard scattering TI Q_0 is not sensitive to imperfections of the topological phase such as transmission of quasiparticles through the wire. Such transmission through the wire would interfere with topological signatures of Majorana modes such as conductance quantization and non-Abelian statistics. To remedy this, we define a variant of the TI, $Q = \det(r)$, which we refer to as topological visibility (TV), as a measure of the topological character of the system. Thus, TV is better suited to determining the visibility of signatures of the Majorana fermion such as quantized conductance peak and non-Abelian statistics than the TI, which is just the sign of the TV. In the limit that we ignore transmission through the wire so that r is unitary, which is the case considered in Refs. [25, 56, 80], this quantity is identical to Q_0. One might be concerned that the topological visibility, Q, is not quantized as Q_0. However, Q is quantized as long as the system is properly gapped so that r is unitary. Whenever Q is not quantized, which is near a topological phase transition, whether Q_0 is trivial or not depends on non-universal details of the system which determine whether $\det(r)$ is slightly positive or slightly negative. To keep our terminology consistent with previous works [25, 56, 80], we will refer to $Q < 0$ to be topological (i.e. $Q_0 = \mathrm{sgn}(Q) = -1$) and $Q > 0$ to be non-topological. The presence of dissipation eliminates the discreteness of the topological visibility Q by relaxing the unitarity of the theory, leading to the possibility of the TV being any number between +1 and -1 instead of having a magnitude precisely equal to unity. Only when Q is close to it's extreme values ± 1 can Q_0 be reliably determined to be topological or not. The TV can be computed from the zero-frequency reflection matrices [25] as

$$Q = Det[r_{ee}r_{ee}^{*} - r_{ee}r_{eh}r_{ee}^{-1}r_{eh}^{*}]. \tag{3.3}$$

The reflection matrices can be computed given the system and lead Hamiltonian, which we discuss in the remainder of the section.

Let us consider a particular semiconductor Rashba nanowire model introduced by Lutchyn *et. al.* [26]— see also Refs. Sau *et al.* [27] and Oreg *et al.* [29]— which was shown to support MZMs at the two ends in the clean limit. These theoretical works directly motivated the nanowire Majorana experiments of Refs. [31–35, 82, 83]. The BdG Hamiltonian describing the 1D nanowire in the presence of Rashba SOC, Zeeman splitting, and superconducting proximity effect, is given by

$$H_{sys} = \left(-\frac{1}{2m^{*}}\partial_x^2 + i\alpha_R\sigma_y\partial_x - \mu\right)\tau_z + \mu_0 B\sigma_x + \Delta_0\tau_x, \tag{3.4}$$

where, m^*, α_R, μ and Δ_0 are the effective mass, the strength of Rashba SOC, the chemical potential and the proximity induced superconducting gap, respectively. Throughout this chapter we set $\hbar = 1$. Here and henceforth $\tau_{x,y,z}$ and $\sigma_{x,y,z}$ are Pauli matrices acting on particle-hole and spin space, respectively. $\mu_0 = g\mu_B$ is the usual gyromagnetic ratio times the Bohr magneton defining the Zeeman field strength $\mu_0 B$. To make it amenable to numerical techniques, we discretize the continuum Hamiltonian as

$$\begin{aligned} H_{sys}^{dis} = \sum_{\boldsymbol{n}} [&-t\left(|n+1\rangle\langle n| + \text{H.c.}\right)\tau_z + i\alpha\left(|n+1\rangle\langle n| - \text{H.c.}\right)\sigma_y\tau_z + \Delta_0|n\rangle\langle n|\tau_x \\ &+ (-\mu + 2t)|n\rangle\langle n|\tau_z + V_Z|n\rangle\langle n|\sigma_x], \end{aligned} \tag{3.5}$$

where $t = \frac{1}{2m^* a^2}$ with a being the lattice constant for the discretized tight-binding model in Eq. (3.5). The length of the nanowire is given by $L = aN$ where N is the number of unit cells in the wire, the SOC strength is given by $\alpha = \frac{\alpha_R}{2a}$, and we have defined the Zeeman field strength, $V_Z \equiv \mu_0 B$ giving the spin splitting. The nondiagonal terms in the site index arise from nearest neighbor hopping. This system has been shown to support MZMs [26, 29]. In fact, for a clean nanowire it is now well-known that MZMs exist as stable localized zero energy excitations at the ends of the nanowire whenever $V_Z > \sqrt{\Delta_0^2 + \mu^2}$.

Before we describe the normal leads that attach to the nanowire to create the normal-superconductor (NS) junction (see Fig. 3.1) for tunneling measurements, we first comment on an important quantity that can be calculated from the system Hamiltonian. It is known that MZMs contribute a local density of states (LDOS) zero bias peak in the topological phase [40]. LDOS not only probes the presence of zero energy modes, but also whether the zero energy mode is localized close to the edge of the wire. In fact, computing or measuring the LDOS is the simplest probe to test the presence or absence of MZMs in the system. LDOS at a given energy ϵ and site i is given by

$$\mathrm{LDOS}(\epsilon, i) = \sum_n \left(|u_{n\uparrow}(i)|^2 + |u_{n\downarrow}(i)|^2 + |v_{n\uparrow}(i)|^2 + |v_{n\downarrow}(i)|^2\right) \delta(\epsilon - \epsilon_n), \tag{3.6}$$

where $\psi_n(i) = \left(u_{n\uparrow}(i), u_{n\downarrow}(i), v_{n\uparrow}(i), v_{n\downarrow}(i)\right)^T$ is the i-th component of eigenvector ψ_n of the Hamiltonian matrix H_{sys}^{dis} with eigenvalue ϵ_n. u's and v's are eigenvector components in particle and hole space, respectively. To calculate the tunneling conductance, we must attach leads to the Rashba nanowire. We assume the leads to be translationally invariant semi-infinite normal leads. The lead Hamiltonian is given by

$$H_{\mathrm{lead}} = \left(-\frac{1}{2m^*}\partial_x^2 + i\alpha_R \sigma_y \partial_x - \mu_{lead}\right)\tau_z + \mu_0 B_{lead} \sigma_x. \tag{3.7}$$

The above lead Hamiltonian is discretized as

$$H_{sys}^{lead} = \sum_{\boldsymbol{n=0}}^{\boldsymbol{N}} [-t\left(|n+1\rangle\langle n| + \text{H.c.}\right)\tau_z + i\alpha\left(|n+1\rangle\langle n| - \text{H.c.}\right)\sigma_y\tau_z$$
$$+ (2t - \mu_{lead})|n\rangle\langle n|\tau_z + \mu_0 B_{lead}|n\rangle\langle n|\sigma_x]. \tag{3.8}$$

Following the Delft experiment [31], a finite applied magnetic field B_{lead} is assumed to exist so as to have two non- degenerate conducting channels because of the spin splitting induced by B_{lead}. Having a finite magnetic field in the lead also helps us to avoid the numerical challenge to identify and separate various channels to compute the S-matrix. We emphasize, however, that our keeping a finite B_{lead} is actually consistent with the experimental situation (and not just a matter of computational convenience).

The potential barrier defining the NS junction at the lead-nanowire interface (see Fig. 3.1) is simulated by modulating the hopping amplitude t' between the nanowire and the lead. For higher(lower) tunnel barrier, the hopping amplitude t' is lower(higher). The new system Hamiltonian $H_{sys}^{dis} \longrightarrow H_{sys}^{'dis}$ has the form,

$$H_{sys}^{'dis} = \sum_{\boldsymbol{n}=2}^{\boldsymbol{N}} [-t\left(|n+1\rangle\langle n| + \text{H.c.}\right)\tau_z + i\alpha\left(|n+1\rangle\langle n| - \text{H.c.}\right)\sigma_y\tau_z + (-\mu + 2t)|n\rangle\langle n|\tau_z$$
$$+ V_Z|n\rangle\langle n|\sigma_x + \Delta_0|n\rangle\langle n|\tau_x] - \left(t'|2\rangle\langle 1| + \text{H.c.}\right)\tau_z + i\alpha'\left(|2\rangle\langle 1| - \text{H.c.}\right)\sigma_y\tau_z$$
$$+ (2t - \mu_{lead})|1\rangle\langle 1|\tau_z + \mu_0 B_{lead}|1\rangle\langle 1|\sigma_x. \tag{3.9}$$

In this setup, $t' << t$ would correspond to a high tunnel barrier or weak lead-nanowire coupling. When $t' \sim t$, the tunnel barrier is low or equivalently, the lead-nanowire coupling is strong (i.e. the barrier is almost transparent). The lead-nanowire tunneling t' introduces a broadening (Γ_L) to be discussed later in this chapter (cf. Eq. (3.11)). A strongly coupled (i.e. large t') lead-nanowire system will have strongly broadened conductance peaks, whereas a weakly coupled lead-nanowire system will have weakly broadened sharp peaks. Narrow resonances appearing from states that are weakly coupled to the lead (as a result of being localized far away from the end) are removed by broadening the energy eigenstates by introducing an on-site imaginary term in the Hamiltonian, i.e., $H'^{dis}_{sys} \longrightarrow H'^{dis}_{sys} + b$ where

$$b = \sum_{\boldsymbol{n}=2}^{\boldsymbol{N}} (-Ji)|n\rangle\langle n|. \tag{3.10}$$

Here J is the parameter controlling the intrinsic broadening, Γ, in the conductance profile. The two are related by $\Gamma = 2J$. We note that this intrinsic broadening is again incorporated in the theory to be consistent with the experimental situation (and not just for computational efficacy) since the measured tunneling conductance spectra do not reflect sharp resonant structures even at the lowest temperatures. Obviously, an environment-induced dissipative broadening (parametrized by Γ in our theory) plays a role in the experiment. We emphasize that broadening plays a key role in our theory, converting the topological quantum phase transition into a crossover and providing a visibility for the braiding measurements.

LDOS is calculated by numerically diagonalizing the system Hamiltonian. Throughout all our calculations, the following set of parameters (unless specified otherwise) is used: $\alpha = 1.79$K, $\mu = 0$K, $t = 12.5$K, $\Delta_0 = 3$K, $L = 1.5\,\mu$m, $a = 54$ nm. For reasons motivating the choice of the parameter set, we refer the reader to Ref. [40]. We believe these parameters to be a reasonably realistic description of the experimental situation in Ref. [31], at least at a qualitative level. As discussed in Appendix D, the conductance and TV are calculated from the scattering matrix that is obtained using 'KWANT'—a quantum transport and simulations package in Python developed principally by Groth *et al.* [84].

3.2 Results: Conductance and topological visibility

3.2.1 Role of broadening versus splitting

While the TV and conductance will be determined by all the microscopic parameters discussed in the last section, we now argue that the qualitative behavior can be understood in terms of a few effective parameters, which in turn are determined by the full set of microscopic parameters in a simple way. For example, as seen from the calculated local density of states plotted in Fig. 3.2, one of the relevant scales that affects the topological properties, the splitting of the MZMs (δ), is relatively independent of the other scales such as lead coupling, but sensitively determined by small variations in the microscopic Zeeman field V_Z in an oscillatory fashion [85–88]. We note that δ is a key parameter determining the topological content of the system in the sense that when this quantity is (exponentially) small, the system is by definition non-Abelian, whereas by contrast, when δ is comparable to the superconducting energy gap, the system is manifestly not topological.

The topological properties of a one dimensional superconductor such as a semiconductor nanowire crucially depend on the various relevant sources of broadening, such as the lead coupling and inelastic scattering, of the quasiparticle excitations. The width of the ZBCP, which is a key signature of topological superconductivity, depends on the broadening, Γ_L, which is controlled by tuning the lead tunneling t' discussed in the previous section. Furthermore, the TV, Q, [25], which characterizes the topology of nanowires with open boundary conditions, is necessarily non-topological (i.e. $Q = 1$) [25] because any calculation of TV in the presence of finite δ (which must always be true in any finite wire) and no broadening must necessarily give Q=1 (i.e. a non-topological trivial system) since the MZM is not located precisely at zero energy for any finite length wire! Typically, this is circumvented by computing the TI at an energy arbitrarily shifted slightly away from zero by the splitting of the MZM, δ. A similar behavior is noticed [43] in the low-bias conductance $G(V) = dI/dV$, which characterizes MZMs through a quantized value $G(V \to 0) = G_0 = 2e^2/h$ [9, 20–22]. For a finite system, the conductance $G(V \gtrsim \delta)$ approaches the quantized value $G(\Gamma_L \gg V \gtrsim \delta) \to G_0$. On the other hand, as V truly approaches zero (i.e. $|V| \ll \delta$), the conductance in the tunneling limit approaches zero [43], giving a vanishing ZBCP (since the Majorana is not located precisely at zero energy in a finite length wire).

Therefore, both the TV (Q) and the zero-bias conductance (G) cannot be evaluated strictly at zero energy for a finite wire to determine the topological phase of the wire. Motivated by the goal of understanding finite rate dynamical processes such as braiding, we avoid this problem by introducing an intrinsic quasiparticle decay rate (i.e. dissipative broadening), Γ, which we believe to be the realistic experimental situation. The broadening Γ is controlled in our calculations by choosing the parameter J discussed in Sec. 3.1. The introduction of such a scale allows us to discuss the conductance (G) and TV (Q) in a meaningful way at exactly zero energy. The intrinsic decay rate, Γ, apart from representing the uncertainty in energy resulting from the finite braiding rate, likely also exists in semiconductor wires from interactions and phonons (and unknown dissipative coupling to the environment invariably present in all solid state systems). Moreover, since the conductance and the TV are determined by the scattering properties of electrons from an external lead, the coupling to the lead, which is parametrized by the broadening Γ_L, quantitatively affects these topological properties. Finally, the superconducting gap Δ that protects topological properties themselves must play a role in determining the topological properties. In the following subsections, we will study

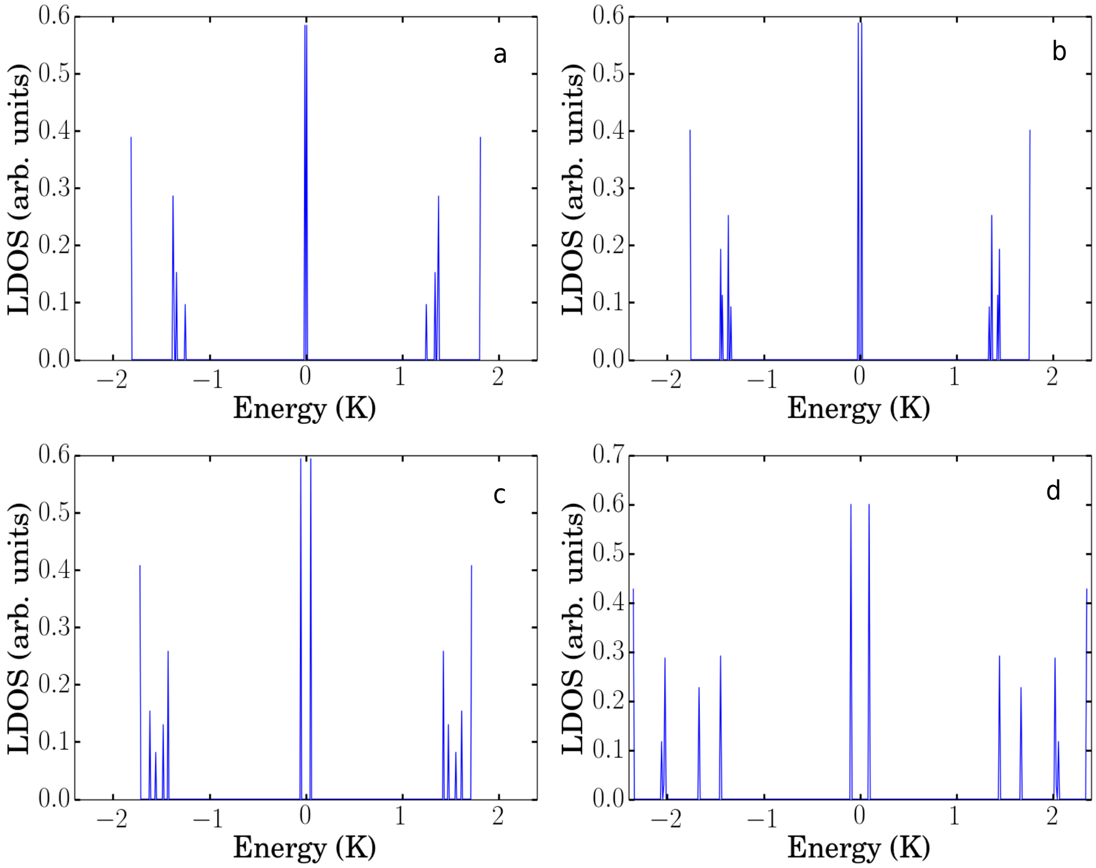

FIGURE 3.2: LDOS for clean nanowire with $L = 1.5 \mu m$ and Zeeman field strengths (a-d), V_Z = 4.2, 4.3, 4.5 and 5.0 K. The corresponding Majorana splitting (a-d) are δ = 0.012, 0.036, 0.094 and 0.18 K respectively clearly vary strongly with V_Z.

the inter-dependence of the conductance and the TV on these energy-scales namely δ, Γ, Γ_L and Δ. We emphasize that the problem is highly complex because these are four completely independent energy scales (and in real experimental systems there are at least two additional energy scales associated with finite temperature and disorder, that we neglect here).

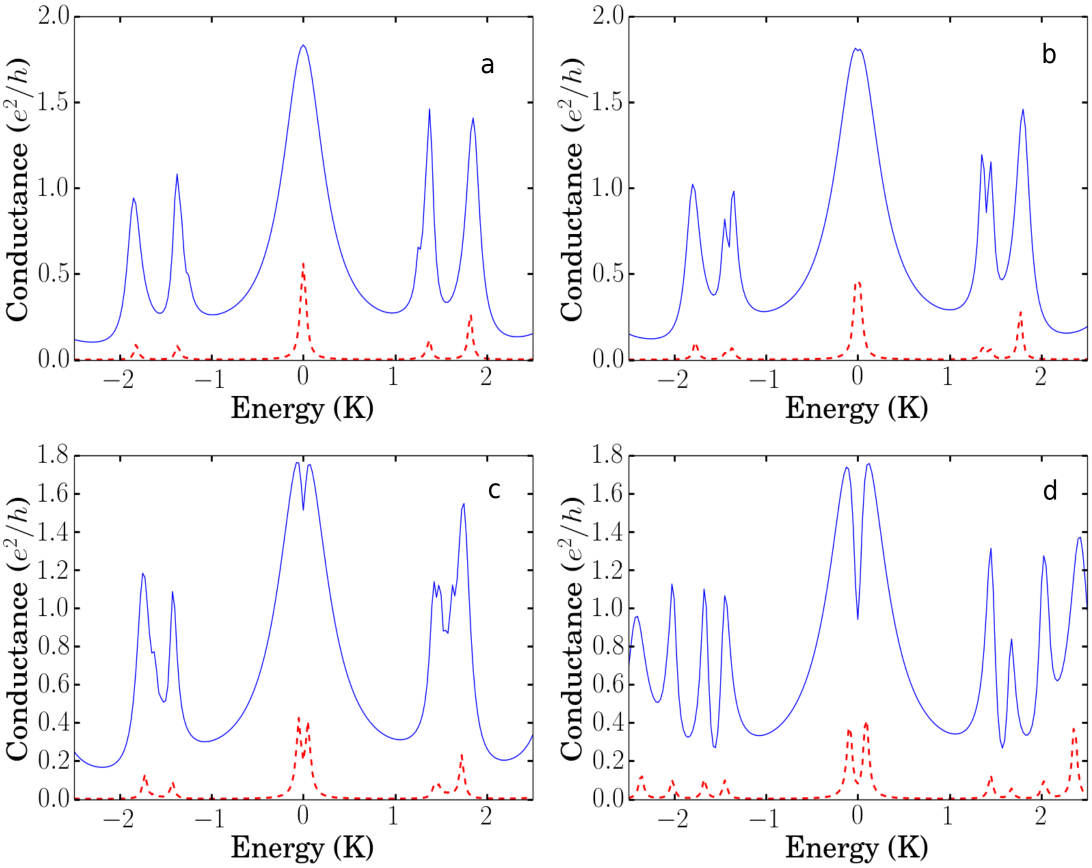

FIGURE 3.3: Conductance plot corresponding to the LDOS splittings for Γ_L/Γ = 10 (blue solid curve) and Γ_L/Γ = 0.25 (red dashed curve). The parameter δ/Γ (a-d) = 0.27 , 0.71 , 1.74 and 3.27 respectively. The TV (Q) values (a-d) are (-0.80,-0.75,-0.46,0.12) and (0.44,0.58,0.82,0.93) for blue solid curve and red dashed curve, respectively. The conductance peaks split for large δ/Γ and the conductance decreases for small Γ_L/Γ.

3.2.2 Topological phase

We start by discussing the zero-bias conductance and TV deep in the topological phase where the intrinsic quasiparticle broadening Γ is much smaller than the topological gap $\Delta \gg \Gamma$ so that the gap Δ is well-defined. We choose the nanowire to be sufficiently long, in this subsection, so that the Majorana splitting δ and the broadening of the MZMs from the lead are much smaller than the gap (i.e. $\delta, \Gamma_L \ll \Delta$).

Since the topological gap Δ is much larger than the parameters relevant to the MZMs namely, the splitting δ, the broadening of the MZM due to coupling to the lead, Γ_L, and the (intrinsic) broadening of the far end MZM (away from the lead), Γ, both the zero-bias conductance $G(V=0)$ and the TV Q, is a function only of δ, Γ_L and Γ. Note that the broadening of the MZM at the far end is the same as the intrinsic quasiparticle broadening Γ, since it is not coupled to the lead. Since the absolute energy scale cannot matter, the conductance $G(V=0)$ and the TV, Q, can be studied as a function of dimensionless parameters Γ_L/Γ and δ/Γ (in this large Δ limit).

Consider first the limit where $\delta/\Gamma \gg 1$, i.e., the broadening is much smaller than the Majorana splitting. As seen from the conductance plot in Fig. 3.3(c,d) (red dashed curve), if the lead coupling also weak i.e. $\Gamma_L \ll \delta$, the conductance profile $G(V)$ shows a pair of resonances at energies $E = \pm\delta/2$ with broadening of order $(\Gamma + \Gamma_L)$. The height of these peaks would be substantially below the quantized value. As seen from the solid blue curve in Fig. 3.3(c,d) and consistent with previous work [43], increasing the lead coupling so that $\Gamma_L \gg \delta$, increases the height of the zero energy peak so as to approach the quantized value $G(V\sim 0) \sim G_0$. However the splitting δ now appears as a dip in the conductance which reduces the conductance $G(V=0)$ at strictly zero-bias. Thus, the zero-bias conductance $G(V=0)$ is suppressed from the quantized value, and as expected from the connection between conductance and TV [22] , we find the TV Q to be non-topological (i.e. positive in this parameter regime).

The conductance $G(V)$ in the opposite limit, where $\delta/\Gamma \ll 1$, is shown in Fig. 3.3(a,b) and shows an unsplit ZBCP. The conductance in the $\Gamma_L \gg \Gamma$ (blue curve) shows a nearly quantized conductance, while the conductance is suppressed in the opposite limit. However, this limit (i.e. $\Gamma_L \ll \Gamma$) (red dashed curve) still shows a ZBCP, albeit substantially smaller than the quantized value even though the corresponding TV is non-topological. On a technical note, varying the Zeeman field between the different panels in Fig. 3.3

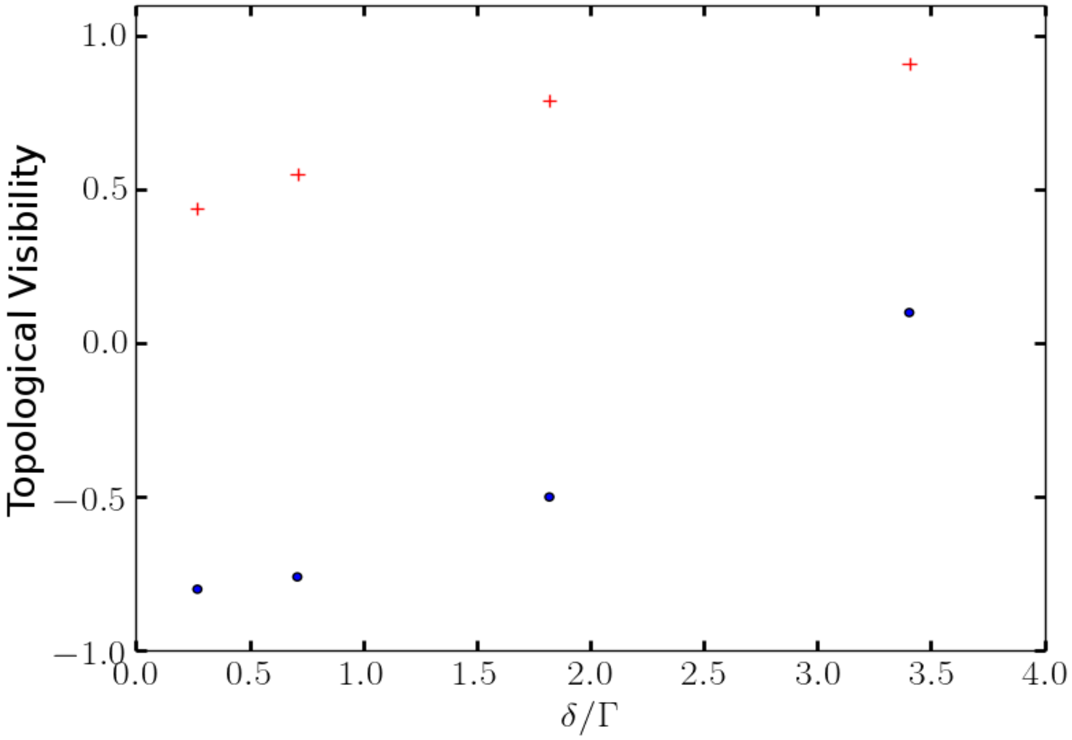

FIGURE 3.4: TV for δ/Γ values corresponding to Fig. 3.3 for coupling parameter $\Gamma_L/\Gamma = 10$ (blue dots) and $\Gamma_L/\Gamma = 0.25$ (red plus). The TV is an increasing function of δ/Γ, i.e., the system tends to become non-topological as δ/Γ increases.

changes Δ. To mitigate any parametric dependence of the calculated ZBCP and TV on Δ, in this subsection the broadening Γ is adjusted in each case to hold $\Delta/\Gamma = 52$ fixed (remembering that the gap Δ depends on the Zeeman field). The lead broadening Γ_L is varied through varying t' (see Eq. (3.11) below) to keep the ratio Γ_L/Γ fixed.

The TV is strongly affected by the splitting of the MZMs δ relative to the broadening Γ. In Fig. 3.4, we find that the TV is an increasing function of δ/Γ. The nanowire effectively becomes non-topological if the MZM splitting δ exceeds the broadening Γ, even when the wire parameters and the strong lead coupling Γ_L favor the topologically non-trivial phase. Furthermore, consistent with the conclusion in Fig. 3.3, the small

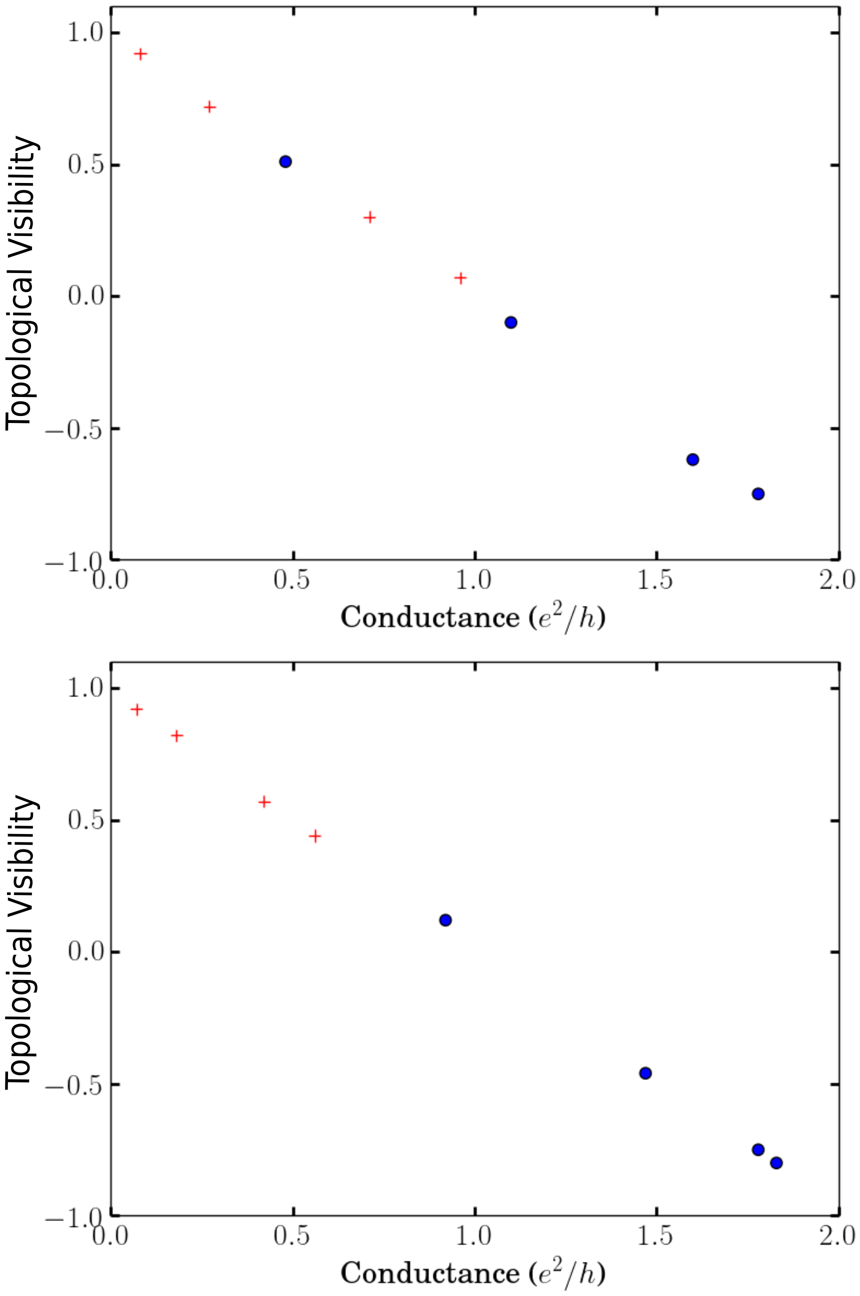

FIGURE 3.5: (Top) Plot of the TV as a function of ZBCP for $\delta/\Gamma = 0.16$ (blue dot) and $\delta/\Gamma = 2.43$ (red plus). Conductance is varied by varying Γ_L/Γ. (Bottom) TV vs ZBCP for $\Gamma_L/\Gamma = 10$ (blue dot) and $\Gamma_L/\Gamma = 0.25$ (red plus). Conductance is varied by varying δ/Γ. The TV is a decreasing function of the ZBCP.

values of Γ_L/Γ lead to non-topological values for the TV.

The combination of Figs. 3.3, 3.4 suggests a correlation between the presence of a quantized ZBCP and a topologically non-trivial value of the TV close to $Q = -1$. This correlation between TV and conductance suggested by Figs. 3.3,3.4 is made explicit in Fig. 3.5. We find that TV is a decreasing function of the ZBCP value. The TV approaches -1(+1) as ZBCP approaches $2e^2/h(0)$. Note that the decreasing behavior of TV with increasing ZBCP is independent of the tuning parameter chosen to vary the zero bias conductance, evidenced by the fact that both top and bottom plots in Fig. 3.5 manifest a decreasing behavior for the TV as a function of ZBCP regardless of whether Γ_L/Γ (top subfigure Fig. 3.5) or δ/Γ (bottom subfigure Fig. 3.5) is tuned to vary ZBCP.

3.2.3 Topological phase transition

Let us now consider the behavior of conductance and TV as we approach the TPT by tuning the Zeeman field V_Z. In this case, when the intrinsic broadening Γ and the lead-induced broadening Γ_L are small, sufficiently close to the phase transition, the topological gap Δ will become smaller than $\Delta \ll \Gamma$ (since at the TPT, the gap must vanish). Therefore, for infinite length systems, the ratio Δ/Γ can be used to determine the distance to the quantum critical point. For conventional quantum critical points [89], there are two dimensionless parameters that characterize the distance to a quantum critical point, which are L/ξ and Δ/T characterizing spatial and imaginary time correlations in the system. Here ξ is the coherence length of the system, Δ is an energy scale, T is the temperature and L is the length of the system. In our discussion, Γ is analogous to temperature T in the quantum critical phase (although we are actually at $T = 0$ throughout). Since Γ is always finite in our system, the TPT is always a crossover even at zero temperature! The fact that our calculated TV value in Figs. 3.4 and 3.5 is continuous between $Q = +1$ (trivial phase) and $Q = -1$ (topological phase) is a clear indication that the presence of dissipative broadening in the theory (and the associated non-unitarity) has rendered the TPT into a crossover with $Q > (<) 0$ defining the non-topological (topological) phase with finite visibility. The presence of dissipation makes some additional changes to the topological transition that we mention in passing. Traditionally in disordered systems the topological transition is often accompanied by a Griffiths like phase populated by weakly split low-energy Majorana modes [90]. The presence of dissipation could change some of these weakly split Majorana modes into poles of the now non-unitary S-matrix with exactly zero energy but different imaginary parts [53]. Such physics, which is exactly included in our theory, would alter the nature of the low-energy density of states near the transition.

The relationship between Γ_L and Δ is not straightforward because as the system approaches the TPT, the bound states become delocalized away from the lead due to the diverging coherence length ξ. In the limit of small lead-tunneling, t', the broadening Γ_L induced by the lead is related to the imaginary part of the lead self-energy [91] and can be written as

$$\Gamma_L \sim t'^2 |\psi(0)|^2, \tag{3.11}$$

where $\psi(0)$ is the value of the nanowire wavefunction at the lead-nanowire NS contact at the given tunneling energy. The localized Majorana wavefunction can be approximated by,

$$\psi(x) \approx \frac{1}{\sqrt{\xi}} e^{-x/\xi}, \tag{3.12}$$

where ξ is the superconducting coherence length. This implies,

$$\Gamma_L \sim t'^2 \Delta. \tag{3.13}$$

Therefore, in the vicinity TPT, $\Delta/\Gamma_L \propto t'^2$ (with the proportionality factor related to the normal phase density of states) approaches a constant and can be used as a parameter to characterize the TPT. Note that although Γ_L is in some sense proportional to the gap Δ, the two quantities are still independent parameters of the theory by virtue of the lead tunneling matrix element t'.

As seen in Fig. 3.6, the TPT is approached by tuning the Zeeman field V_Z, which leads to the variation of both the Majorana splitting δ (lowest Andreev bound state energy) in the upper panel and the bulk gap Δ (next highest Andreev boundstate energy) in the lower panel. The minimum in the gap Δ occurs at $V_Z = 3\mathrm{K}$ indicating a transition at this value of the Zeeman potential. For a finite system, the minimum gap is determined by the length of the system L. In the case where the wires are shorter than the dephasing length $l_\varphi \sim v_F/\Gamma$ (for the chosen Γ), where v_F is the Fermi velocity of the system, the MZMs split before entering the TPT region $\Delta \lesssim \Gamma$. As a result, the system enters a non-topological phase with a TV close to $Q = 1$ similar to the $\delta \gtrsim \Gamma$ case discussed in the last subsection. Therefore, in this section we focus on a broadening Γ that is larger than the finite size gap, i.e. $\Gamma \gtrsim v/L$.

Let us now consider the conductance shown in Fig. 3.7 as the Zeeman field is varied towards the topological transition. Fig. 3.7(a) shows a nearly quantized peak (blue solid) deep in the topological phase where the MZM splitting δ is also small relative to the broadening Γ. The corresponding TV is also seen to be nearly topological in Fig. 3.8 as expected. As the Zeeman field is decreased, the height of the ZBCP (above the background) decreases as one approaches the topological transition where $\Delta/\Gamma \to \delta/\Gamma$ becomes small in Fig. 3.7(c). However, it should be noted that the peak remains unsplit in contrast to the short wire case with $L \lesssim l_\varphi$. Despite the presence of a small zero bias peak in Fig. 3.8(b,c), the corresponding TV values in Fig. 3.8 are positive (non-topological). This is consistent with Figs. 3.3 and 3.4 from the previous

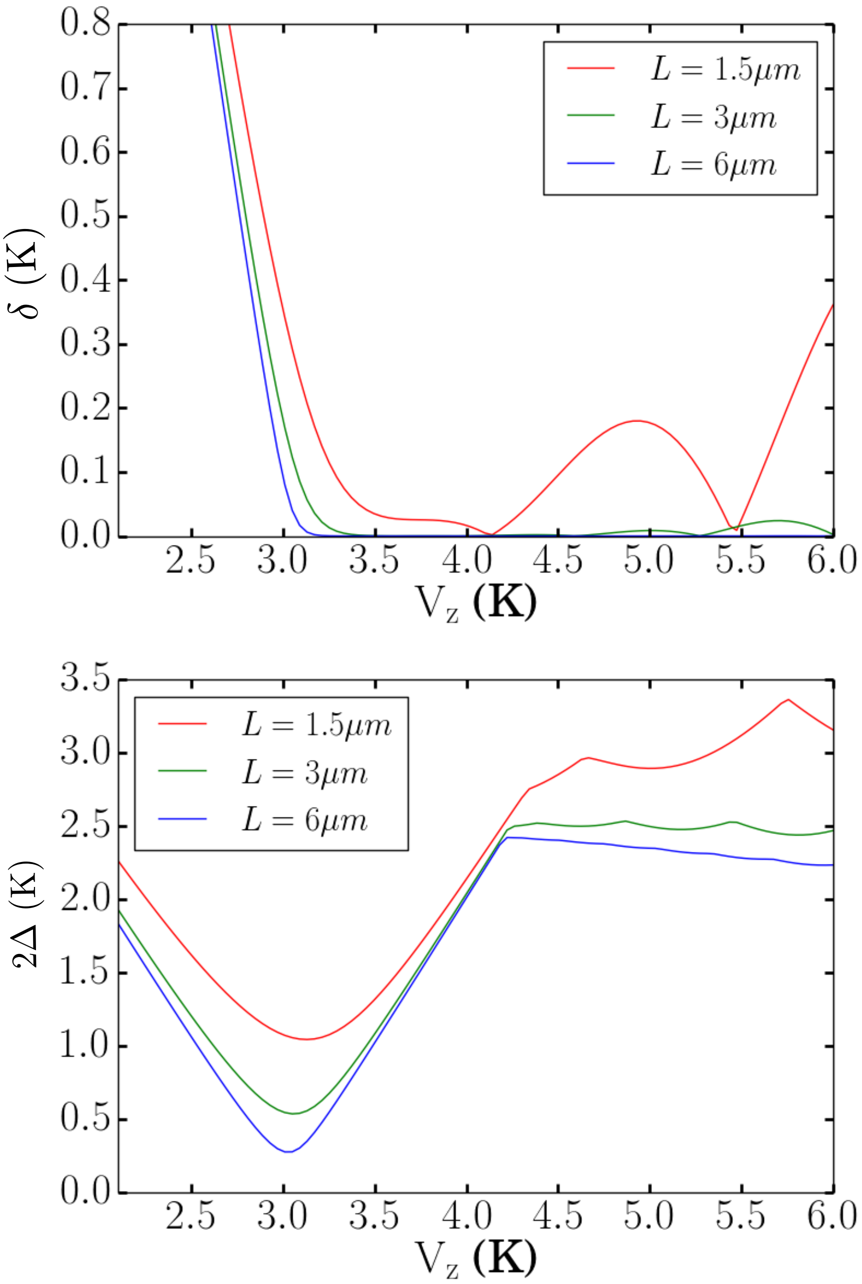

FIGURE 3.6: Plot of Lowest Andreev bound state energy (top) and bulk quasiparticle energy gap (bottom) as a function of Zeeman field strength for different physical lengths of Majorana nanowire. The bulk TPT is at $V_Z = 3$K. In the topological phase, ($V_Z > 3$K), lowest Andreev bound state energy is the Majorana splitting.

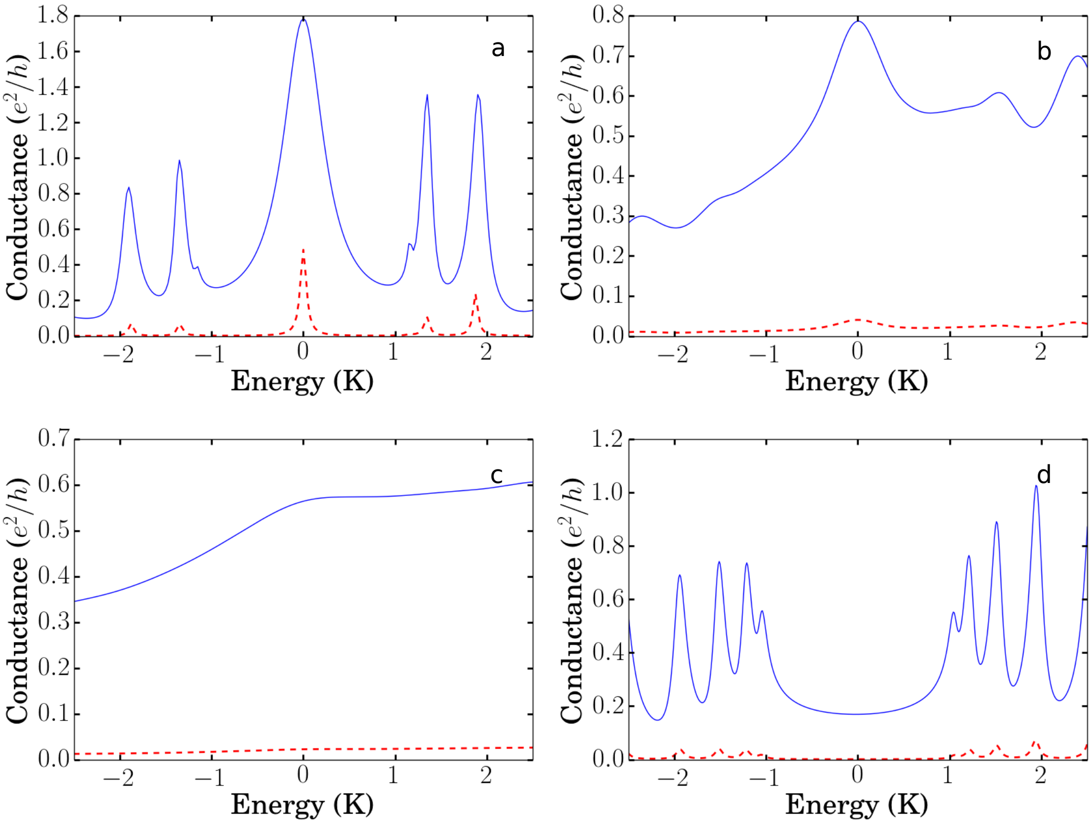

FIGURE 3.7: Conductance plot for Γ_L/Δ = 0.20 (blue solid curve) and Γ_L/Δ = 0.005 (red dashed curve). Broadening Γ is chosen so that δ/Γ= 0.16 is held fixed for all panels with Δ/Γ (a-d) being 19.33, 0.90, 0.28, -12.1, respectively. The TV (Q) values (a-d) are (-0.75,0.34,0.56,0.98) and (0.51,0.95,0.97,1.0) for blue solid curve and red dashed curve, respectively.

subsection where a small coupling $\Gamma_L \ll \Gamma$ led to small non-topological ZBCP. Finally, as one crosses over to the non-topological regime, a non-topological gap appears in the conductance. As mentioned before, the TPT is parameterized by Γ_L/Δ, which remains relatively constant near the phase transition. The red dashed plots in Fig. 3.7 show that the conductance is systematically suppressed in the regime of small Γ_L/Δ. The corresponding TVs are seen to be positive (non-topological) in Fig. 3.8.

Before concluding this section, we comment on an obvious point which might confuse a non-alert reader. One may think that the TV can have only unit magnitude with

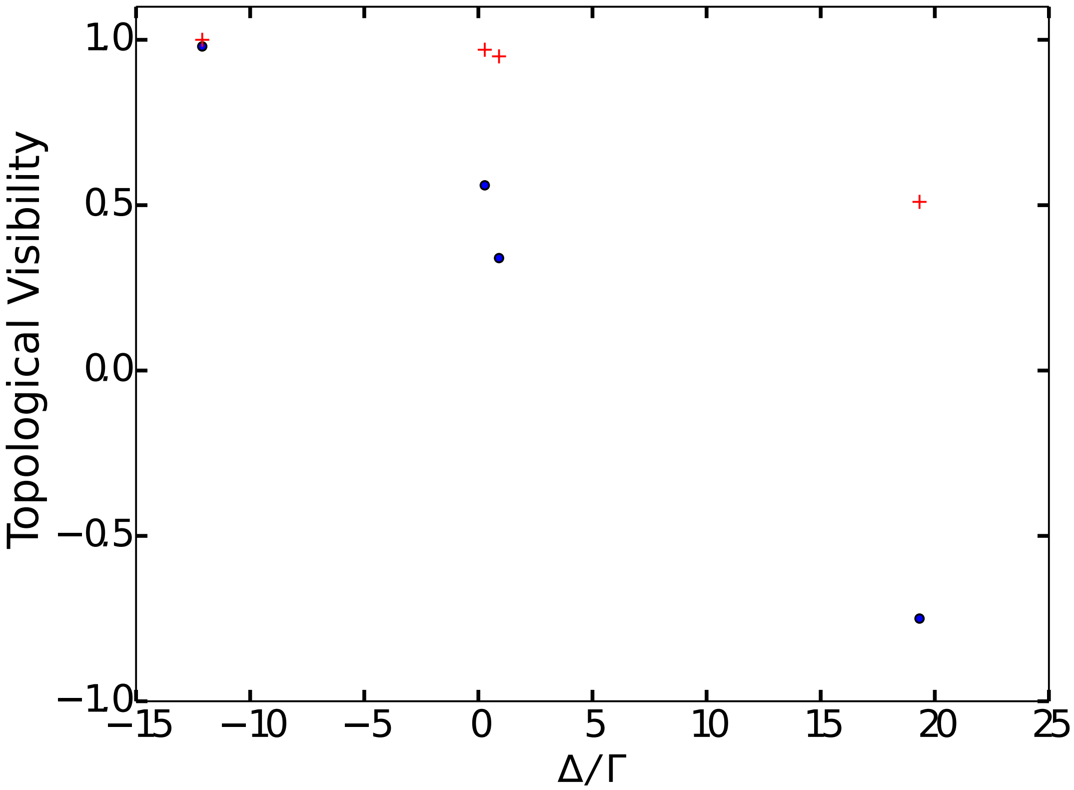

FIGURE 3.8: TV for Δ/Γ values corresponding to Fig. 3.7 for coupling parameters near TPT with Γ_L/Δ = 0.20 (blue dots) and 0.005 (red plus), respectively. $\delta/\Gamma = 0.16$ is held fixed. The TV is an decreasing function of Δ/Γ with $Q \longrightarrow 1$ as $\Delta/\Gamma \longrightarrow 0$, i.e., the system tends to become non-topological (topological) as the system tends to small (large) topological gap and the TV tends to +1 as the gap completely closes (system approaches TPT).

Q=-1 (+1) characterizing the topological (trivial) phase. This is indeed so in the infinite system as originally introduced by Kitaev [4]. But our finite system must have a broadening (otherwise the TV calculated at zero energy is always +1 because of Majorana splitting), and this broadening allows the TV (i.e. Q) to be a continuous function of system parameters going from +1 deep in the trivial phase to -1 deep in the topological phase. This continuous evolution of Q between +1 and -1 is the finite system crossover transition whereas the corresponding infinite system would have a sharp transition from

+1 to -1 precisely at the TPT (with the ZBCP value changing from zero to $2e^2/h$ sharply at the TPT too). We connect this crossover transition to braiding experiments with the claim that our finding a value of $Q < 0$ corresponds to a topological phase with the visibility of the braiding measurements being large (small) depending on whether the magnitude of Q is close to unity (zero). We believe that our finding a negative (positive) value of Q corresponds to the corresponding braiding experiment manifesting (not manifesting) non-Abelian statistics.

3.3 Braiding and tunneling conductance

Consider a specific braiding protocol described in Sec. 1.3 illustrated by Fig. 1.5 where the dynamics is governed by the Hamiltonian in Eq. 1.25. There, we assumed ideal Majorana modes at precisely zero energy being exchanged with each other under unitary adiabatic time-evolution. However, any realistic braiding experiment must take into account a few prominent departures from the idealized set of implicit assumptions made above in our schematic description of perfect Majorana braiding. First, any finite system hosting MZMs will have a finite Majorana wavefunction overlap, splitting the Majorana modes by an energy δ, away from zero energy due to the hybridization between the two MZM wavefunctions from the two wire ends [43]. Obviously, a large overlap (as would happen in shorter nanowires or in systems with small superconducting gaps leading to large coherence lengths) would completely destroy all non-Abelian topological properties since the Majorana excitations in that situation are simply the electron-hole quasiparticle excitations of the superconducting nanowire with the Majorana splitting being comparable to the superconducting energy gap. Including this Majorana splitting in the formalism is an important ingredient of our theory. Second, "adiabatic" braiding process takes place over a finite time scale δt_B i.e. with a finite braiding velocity) , which is associated with the energy uncertainty of the system δE_B

estimated by

$$\delta t_B \delta E_B \sim \hbar. \tag{3.14}$$

We note that this braiding-induced energy uncertainty δE_B must be much larger (smaller) than the Majorana splitting (superconducting gap) for the braiding operation to manifest any topological non-Abelian behavior. One can loosely identify this energy uncertainty as an effective dissipation term arising from the finite velocity braiding process. Including an energy broadening or a dissipative term is a key ingredient of our theory. Such dissipation could arise from the energy uncertainty associated with braiding as discussed above, but in the specific context of the tunneling conductance measurements, it arises from intrinsic dissipation of strength Γ, which might be present in the experimental situation.

While one might argue that braiding experiments differ fundamentally from conductance experiments since the latter depends on Γ_L and the former doesn't, the braiding proposals [15–17, 77, 78, 92–101] to date require the presence of Majorana fermion tunneling in a key way. The Majorana tunneling enters the through the tri-junctions in the Majorana braiding proposals. In fact, the magnitude of the gap generated between Majorana modes at the tri-junction limits the speed of braiding. Analogous to the tunneling case, the proper topological movement of MZMs requires that the velocity-induced broadening of Majoranas satisfies $\delta \ll \Gamma$ since any braiding must involve an actual physical movement of MZMs around each other. Furthermore, to ensure the presence of MZMs at the ends of the topological set-up, the spurious finite-size Majorana splitting δ must be smaller than $\Gamma_L \gg \delta$. Thus, inclusion of energy broadening $\delta E_B \sim \Gamma$ (to represent finite braiding velocity), tunneling broadening Γ_L, and Majorana splitting δ are essential ingredients of the braiding process as much as they are in the tunnel conductance and the TV calculations discussed in the last section. We therefore see a one-to-one correspondence between braiding and tunneling measurements with the TV showing up in both measurements as the key quantity determining the topological behavior of the circuit.

The braiding properties of a system might be quantified by P_{braid}, which we define to be the probability of success of non-Abelian braiding. The probability of successful non-Abelian braiding, similar to the TV discussed in the last section, is a function of the amount of non-universal broadening Γ present in the braiding experiment (i.e. the sum of the energy uncertainty δE_B and the intrinsic broadening due to coupling to the environment Γ'), the Majorana splitting (δ), the tunnel coupling Γ_L and the topological gap (Δ). Furthermore, since braiding is presumably a topological property, we expect the probability of success of braiding to be related to the TV. Based on this argument we conjecture that the success rate of non-Abelian braiding for a given braiding speed in an experiment (P_{braid}) is related to the probability of TV being -1, i.e.,

$$P_{\mathrm{braid}}(\delta E_B + \Gamma', \Gamma_L, \delta, \Delta) \sim \frac{1 - \langle Q(\Gamma, \Gamma_L, \delta, \Delta)\rangle}{2}, \tag{3.15}$$

where $\langle Q\rangle$ is the average of TV over disorder realizations for a given disorder strength, where Γ' is the environment-induced intrinsic broadening in the braiding experiment. Γ_L in a tunneling conductance experiment represented in the RHS of Eq. (3.15) is the lead broadening as discussed in the previous sections. However, Γ_L appearing in the LHS of Eq. (3.15) represents the induced tunnel gap as a result of strongly coupled adjacent Majorana modes forming a Dirac fermion (strong Majorana pairing regions depicted by pink ovals in Fig. 1.5). The fundamental role played by lead induced broadening for conductance experiment is same as that of gap induced by coupling adjacent nanowire edge modes forming a Dirac fermion in a braiding experiment and therefore for the sake of brevity we have chosen to represent it with the same symbol Γ_L on both sides of Eq. (3.15).

From the previous section, we know that whether the average TV $\langle Q \rangle$ is nearly topological, which (according to our conjecture Eq. (3.15)) would correspond to successful braiding, is directly correlated with the presence of a ZBCP value close to the topological value $G(V \sim 0) \sim G_0$. Such a nearly quantized ZBCP, which can be tested for through existing experimental set-ups [31, 33–35, 82, 83], can only occur in much smaller parameter regime $\Delta \gg \Gamma_L \gg \Gamma \gg \delta$. Furthermore, temperature, which provides a fifth independent energy scale through the thermal energy $k_B T$ (which we take to be zero— in principle, one could assume that $k_B T$ is included in the intrinsic broadening term Γ) must be small as well. It is only in this parameter regime that one expects braiding to be reasonably successful. We believe that this parameter regime can be diagnosed from the much simpler conductance quantization measurements.

Our results (see Fig. 3.5) in section 3.3 indicate that a ZBCP value around half of the quantized value (i.e. ZBCP $\sim e^2/h$) should be adequate to produce a negative TV value. The negative TV would correpond to the topologically non-trivial phase with a TI of -1. Based on this we conclude that braiding experiments would succeed (perhaps with rather low visibility) as long as the corresponding ZBCP is around e^2/h in the same nanowire sample with identical system parameters. We believe that for systems with ZBCP much lower than e^2/h, the braiding experiments are unlikely to succeed in manifesting a purely topological phase with a TV value of -1. This is an important predicted experimental consequence of our theory.

3.4 Summary

We establish a theoretical connection between the tunneling conductance and the topological visibility of realistic spin-orbit coupled semiconductor nanowires. The new important concept introduced in this chapter is topological visibility, which is essentially the 'nonunitary' version of the well-known 'topological invariant' extensively used to characterize topological superconductivity. Whereas the topological invariant is a topological index, being +1 or -1 corresponding to trivial and topological superconductors, respectively, the topological visibility by contrast corresponds to a continuous variable (varying between +1 and -1) relevant for finite systems where a naive computation of the topological invariant will always indicate a trivial phase by virtue of the Majorana energy splitting always being finite in finite systems. The topological visibility is a physical (and practical) generalization of the mathematical concept of topological invariant to realistic finite nanowires in the laboratory, where some Majorana splitting is inevitable because of the wavefunction overlap between the Majorana zero modes localized at the two ends of the finite wire. The physical mechanism enabling the existence of topological visibility is dissipation or level broadening invariably present in all real systems. In particular, this broadening must exceed the Majorana energy splitting for the system to behave 'topologically' (i.e. for the topological visibility to be negative). But this dissipative broadening also suppresses the value of ZBCP below the canonically quantized value of $2e^2/h$ in the topological phase and reduces the magnitude of the topological visibility below unity. For braiding experiments of the future, a part of this dissipation arises from the finite speed of braiding itself which gives rise to an energy broadening, and this broadening must exceed the Majorana splitting energy for the system to behave as a non-Abelian system.

We have also shown that the topological quantum phase transition separating the trivial phase (a TV value of 1 and a ZBCP value of zero) from the topological phase (a TV value of -1 and a ZBCP value of $2e^2/h$) is a crossover in real systems (even at zero temperature) because of the presence of the broadening terms Γ, tunneling Γ_L and the Majorana splitting (δ). The inclusion of the dissipative broadening processes, which must invariably be present in real systems, is a key ingredient of our theory— in fact, without any broadening, the ZBCP is always zero at zero energy by virtue of the Majorana splitting in all finite wires. We find that the ZBCP evolves from a quantized peak deep in the topological phase into a much smaller peak on a large background near the transition, quite similar to some of the experimental results [31, 33–35, 82, 83]. We find that it is possible for the system to be topological (i.e. negative value for the TV) even when the corresponding zero bias conductance value is suppressed from $2e^2/h$— in particular, a factor of 2 suppression of the ZBCP would still lead to the existence of non-Abelian braiding statistics (with somewhat low visibility). On the other hand, we believe that systems with ZBCP values suppressed by factors of 10 (or more) from $2e^2/h$ are unlikely to ever manifest non-Abelian statistics, and such systems are better considered as non-topological systems because of the very large Majorana splitting in spite of there being a small ZBCP peak. Our most important qualitative conclusion is the finding that it is indeed possible for a finite wire with split MZMs (and a correspondingly suppressed ZBCP value compared with $2e^2/h$) to manifest non-Abelian braiding statistics with the visibility of braiding (averaged over many runs) decreasing with decreasing value of the corresponding ZBCP.

Chapter 4: Correlated zero bias conductance as Majorana signature

In this chapter we propose to use the fact that the zero-bias-conductance-peak (ZBCP) associated with a topological phase must appear at both ends at the same value of magnetic field to propose that ZBCP can serve as a probe for topological superconductivity. The appearance of the ZBCP is a property associated with the topological phase transition from the conventional superconducting phase to the topological superconducting phase [5]. Our model system is a quasi-1D weakly disordered Majorana nanowire model. Several proposals [102–104] for detecting topological superconductivity in the one dimensional nanowire systems already involve detecting the topological phase.

4.1 Model Hamiltonian

A schematic representation of an experimental setup to measure left and right tunneling conductance (denoted by G_L and G_R) at a bias voltage V is shown in Fig. 4.1. A semiconductor nanowire with Rashba spin-orbit coupling is connected to the leads at the two ends of the nanowire through a potential barrier. A magnetic field is applied parallel to the nanowire and the proximate s-wave superconductor induces a superconducting order parameter in the nanowire. Experimentally, the conductance for a lead at a given voltage V is calculated by measuring the differential conductance, $G = dI/dV$ (Eq. 1.32).

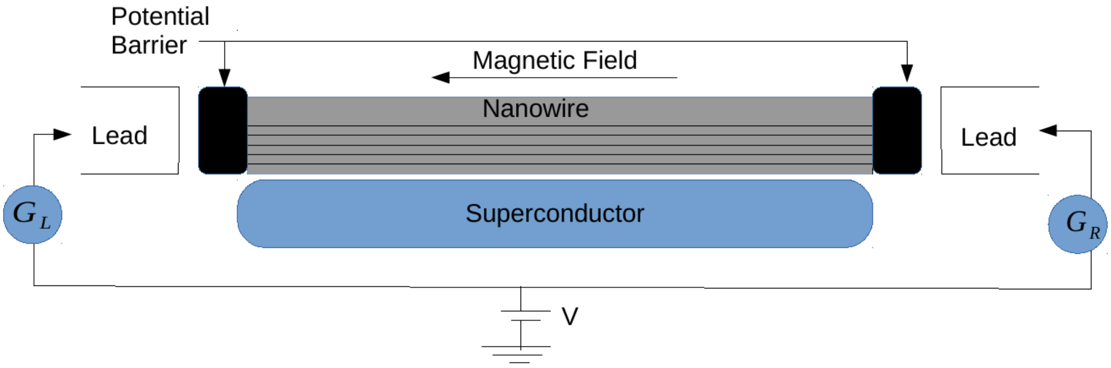

FIGURE 4.1: A schematic representation of an experimental setup for measurement of tunneling conductance at the two ends of the nanowire for voltage bias V. The normal leads are attached to the nanowire system through a potential barrier region shown in black. Magnetic field is applied parallel to the nanowire and S-wave superconducting order parameter is induced in the nanowire by the proximate superconductor.

Theoretically, conductance through a junction separating a normal lead and a class D superconductor [51, 54] is expressed as (see Appendix E for details)

$$G = N - \mathrm{Tr}(r_M \tau_y r_M^\dagger \tau_y), \tag{4.1}$$

with N being the number of conducting channels for electrons in the lead and r_M being the reflection matrix of the system in the Majorana representation (see Appendix E). In terms of zero-frequency reflection matrices, topological visibility (TV) is expressed as [105]

$$Q = \det(r_M). \tag{4.2}$$

A spin-orbit coupled semiconductor nanowire in proximity to S-wave superconductor has been theoretically shown to support MZMs in the presence of magnetic field

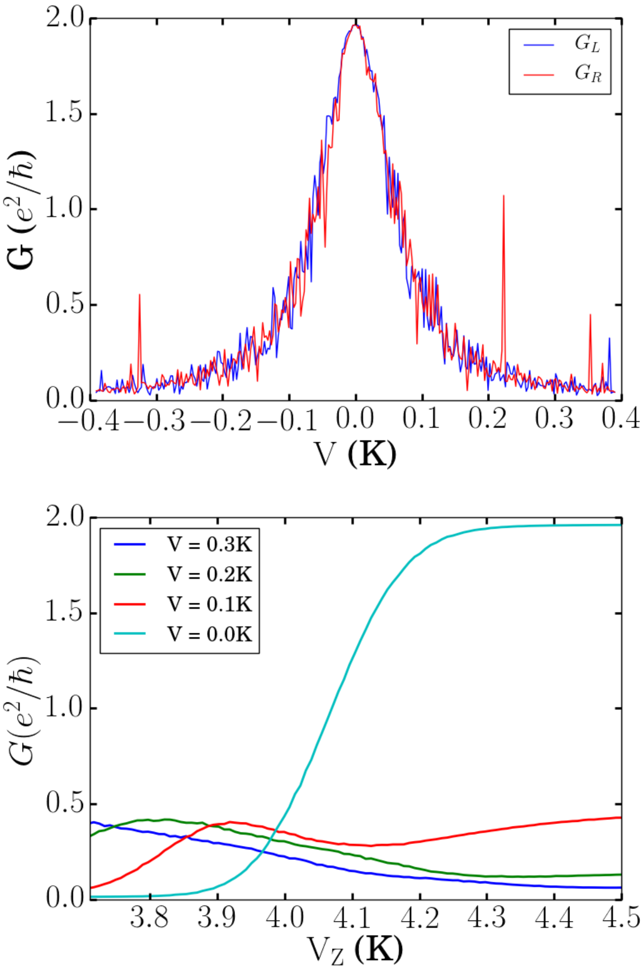

FIGURE 4.2: (top) Plot of tunneling conductance as a function of voltage bias through the left and the right lead as shown in the key, for length $L = 3\mu\mathrm{m}$ and width $W = 0.4\mu\mathrm{m}$ nanowire obtained for a typical disorder realization corresponding to mean free path $L_{mf} = 1.1\mu\mathrm{m}$ at $\mathrm{V_Z} = 4.4\mathrm{K}$. The value of V_z corresponds to the nanowire being the topological phase in the corresponding clean system. For a typical disorder realization fluctuation in left and right conductance is manifest, however the expectation values of left conductance, G_L and the right conductance, G_R are same upon averaging over disorder realizations. (bottom) Plot of disorder-averaged conductance for the system parameters used for the top panel as a function of Zeeman field strength at different voltage biases shown in the key. The zero voltage conductance transitions from 0 to 2 $e^2/\hbar$ over 3.8-4.3 K Zeeman field strength pointing to a topological phase transition in the vicinity of $V_z = 4\mathrm{K}$. The low and high Zeeman field zero-bias-conductance saturation values are consistent with non-topological and topological phase zero-bias-conductance values in a clean system. The appearance of large difference in conductance values between zero voltage and the rest at higher Zeeman field strength values establishes appearance of a zero-bias-conductance-peak.

parallel to the wire [26, 29]. The nanowire is effectively described by the Hamiltonian

$$H_{sys} = \left(-\frac{1}{2m^*}\partial_x^2 + i\alpha_R\sigma_y\partial_x - \mu\right)\tau_z + V_Z\sigma_x + \Delta_0\tau_x \tag{4.3}$$

where, m^*, α_R, μ, V_Z and Δ_0 are the effective mass, the strength of Rashba SOC, the chemical potential, Zeeman field strength and the proximity-induced superconducting gap, respectively. The Hamiltonian in Eq. (4.3) describes an idealized, clean single subband system. However, the semiconductor nanowire samples that are used to experimentally detect and study the MZMs are known to possess multiple subbands and disorder [31, 35]. Further theoretical studies have established the presence of MZMs in disordered multi-subband systems [40, 43, 57, 106, 107]. For disordered multi-subband system, the Hamiltonian is given by,

$$H_{sys} = \left(-\frac{1}{2m^*}\nabla^2 + i\alpha_R\sigma_y\partial_x + i\beta_R\sigma_x\partial_y - \mu + V_{dis}(\boldsymbol{r})\right)\tau_z + V_Z\sigma_x + \Delta_0\tau_x, \tag{4.4}$$

where α_R and β_R are Rashba coupling constants. The Hamiltonian acts on 2-dimensional real space and belongs to symmetry class D. We assume independent and identical distribution of disorder potential V_{dis} in position space. We model the distribution of disorder strength by a Gaussian where its variance (σ) is related to disorder strength through mean scattering rate $\tau^{-1} \approx 2\pi\frac{\sigma^2 D(\mu)}{N_c}$ where $D(\mu)$ is the density of states at the chemical potential and N_c is the number of fully occupied subbands.

A key signature of MZMs is tunneling conductance quantization at zero bias at a value of $2e^2/h$ [9, 20–22]. Experimentally tunneling conductance is measured by coupling the system to a normal lead through a tunnel barrier. The normal lead is modeled by the Hamiltonian,

$$H_{lead} = \left(-\frac{1}{2m^*}\nabla^2 - \mu_{lead} + i\alpha_R\sigma_y\partial_x\right)\tau_z + V_Z^{lead}\sigma_x. \tag{4.5}$$

To compute conductance numerically, we discretize H_{lead} and H_{sys} and couple the lead to the system system through a tunable hopping amplitude to simulate the barrier potential. Furthermore, for simplicity we assume the limiting case $\beta_R \to 0$. While when β_R is strictly zero, the symmetry classification for the Hamiltonian changes from class D to class BDI [108] where the systems in class BDI could have multiple Majorana modes at each end of the nanowire as opposed to class D systems where only a single Majorana mode can exist at each end of the nanowire. However, this subtle distinction within their respective topological phases is unimportant for our purpose as we restrict our analysis in the vicinity of the topological phase transition where only a single Majorana mode pair exists in the topological phase.

The tight binding form of lead and system Hamiltonian is given by

$$\begin{aligned} H^{TB}_{\text{lead}} = \sum_{i}\sum_{j=1}^{N_y} & [-t\left(|i+1,j\rangle\langle i,j| + |i,j+1\rangle\langle i,j| + \text{H.c.}\right)\tau_z \\ & + i\alpha\left(|i+1,j\rangle\langle i,j| - \text{H.c.}\right)\sigma_x\tau_z + (2t-\mu_{lead})|i,j\rangle\langle i,j|\tau_z + V_Z^{lead}|i,j\rangle\langle i,j|\sigma_z \end{aligned} \tag{4.6}$$

$$\begin{aligned} H^{TB}_{sys} = \sum_{i=2}^{N_x}\sum_{j=1}^{N_y} & [-t\left(|i+1,j\rangle\langle i,j| + |i,j+1\rangle\langle i,j| + \text{H.c.}\right)\tau_z \\ & + i\alpha\left(|i+1,j\rangle\langle i,j| - \text{H.c.}\right)\sigma_x\tau_z + (-\mu+2t)|i,j\rangle\langle i,j|\tau_z + V_Z|i,j\rangle\langle i,j|\sigma_z \\ & + \Delta_0|i,j\rangle\langle i,j|\tau_x] - \left(t'|2,j\rangle\langle 1,j| + \text{H.c.}\right)\tau_z + i\alpha'\left(|2,j\rangle\langle 1,j| - \text{H.c.}\right)\sigma_x\tau_z \end{aligned} \tag{4.7}$$

where, i, j run along x,y directions respectively. V_n^{dis} is the random onsite disorder whose strength (value) is chosen from a Gaussian distribution having σ standard deviation. The tight binding parameters σ, α, total sites in x and y directions N_x,N_y are chosen to match estimates for mean free path, spin-orbit splitting, length of wire and number of participating channels. The parameter t' controls the strength of hopping between the lead and the system. The left and the right leads have identical Hamiltonians and are coupled to the two ends of the nanowire as shown in the Fig. 4.1. When concerned with transport characteristics involving the left(right) lead, the right(left) act as an dissipative bath. This lead dissipation broadens the conductance profile. To fine-tune dissipative broadening, we introduce a parameter J that controls the strength of an on-site imaginary term to the system Hamiltonian, i.e. $H_{sys}^{TB} \to H_{sys}^{TB} + b$ with

$$b = \sum_{n=2}^{N} (-Ji)|i,j\rangle\langle i,j|. \tag{4.8}$$

The experiments on Majorana nanowires [31, 109] estimate the effective mass of electron $m^* = 0.015 m_e$, $\Delta = 250\mu$eV and $E_{so} = 50\mu$eV, where m_e , E_{so} are the mass of the electron and the energy of spin orbit coupling, respectively. The tight binding parameters can be expressed in terms of measurable quantities $t = 1/(2m^* a)$ in the units $\hbar = 1$ and $\alpha = \sqrt{(tE_{so})}$. For ϵ_n being the energy of the n^{th} conducting channel, the density of states at the chemical potential μ is given by $D(\mu) = \sum_{\epsilon_n} \frac{1}{\pi t \sqrt{1-\left(\frac{\epsilon_n}{2t}\right)^2}}$ where, the sum runs over all the states occupied below the chemical potential μ. Then, the standard deviation of the disorder potential can be estimated by the Born approximation $\sigma = \sqrt{N_c v_f/(2\pi D(\mu) L_{mf})}$ [48]. Throughout this chapter we have chosen the following tight binding parameters: $t = 12.5$K, $\alpha = 1.79$K, $\Delta_0 = 3$K, $N_c = 4$, lattice constant $a = 50$nm and $\mu = 8$K and disorder strength that corresponds to the mean free path $L_{mf} = 1.1\mu$m. . The lead-nanowire hopping amplitude, $t' = 2.5$K and dissipation broadening parameter, $J = 0.001$K. The conductance and the TV are numerically calculated using 'KWANT' [84]

For a system with a typical disorder realization, Fig. 4.2(top) is a plot of left and

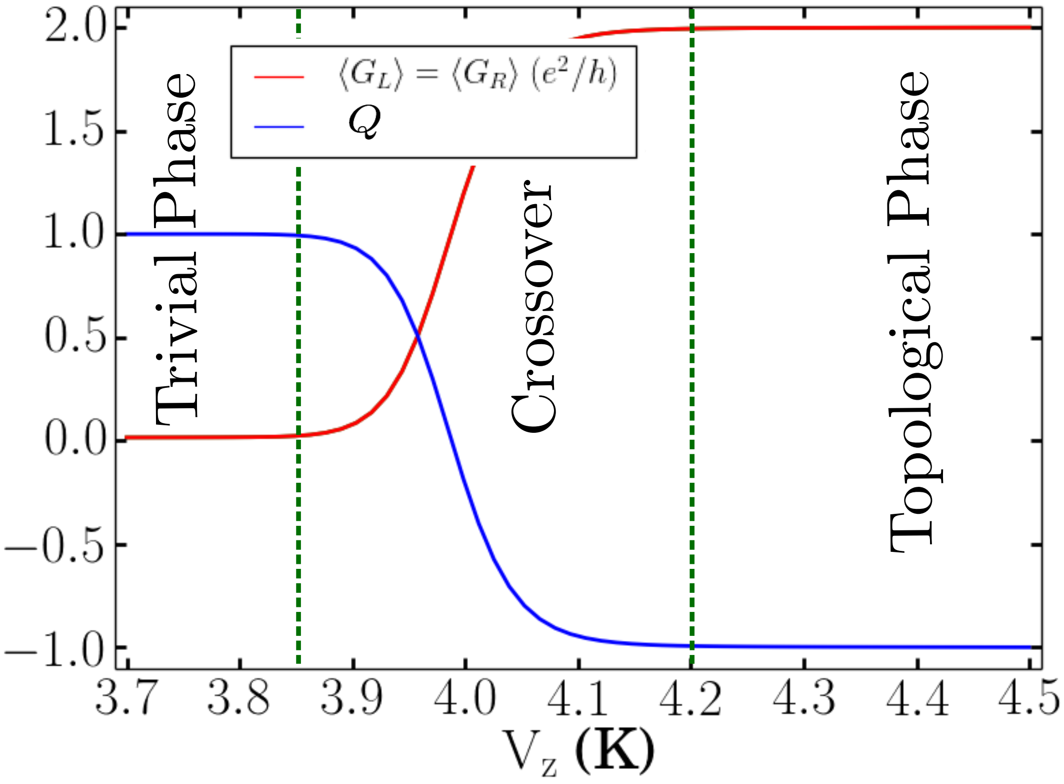

FIGURE 4.3: The conductance, $G \equiv G_L = G_R$ (in units of e^2/h) (red curve) and TV (blue curve) plotted for a clean nanowire of length 3μm as a function of Zeeman field strength to demonstrate 3 distinct regions in the phase diagram.

right conductance in the vicinity of zero bias. Fig. 4.2 (bottom) establishes the existence of a zero-bias peak across the TPT. The topological nature of the transition ensures that at zero bias left and right conductance peaks appear simultaneously as the system enters the topological regime. This is the result of highly correlated zero-bias fluctuations of left and right conductance.

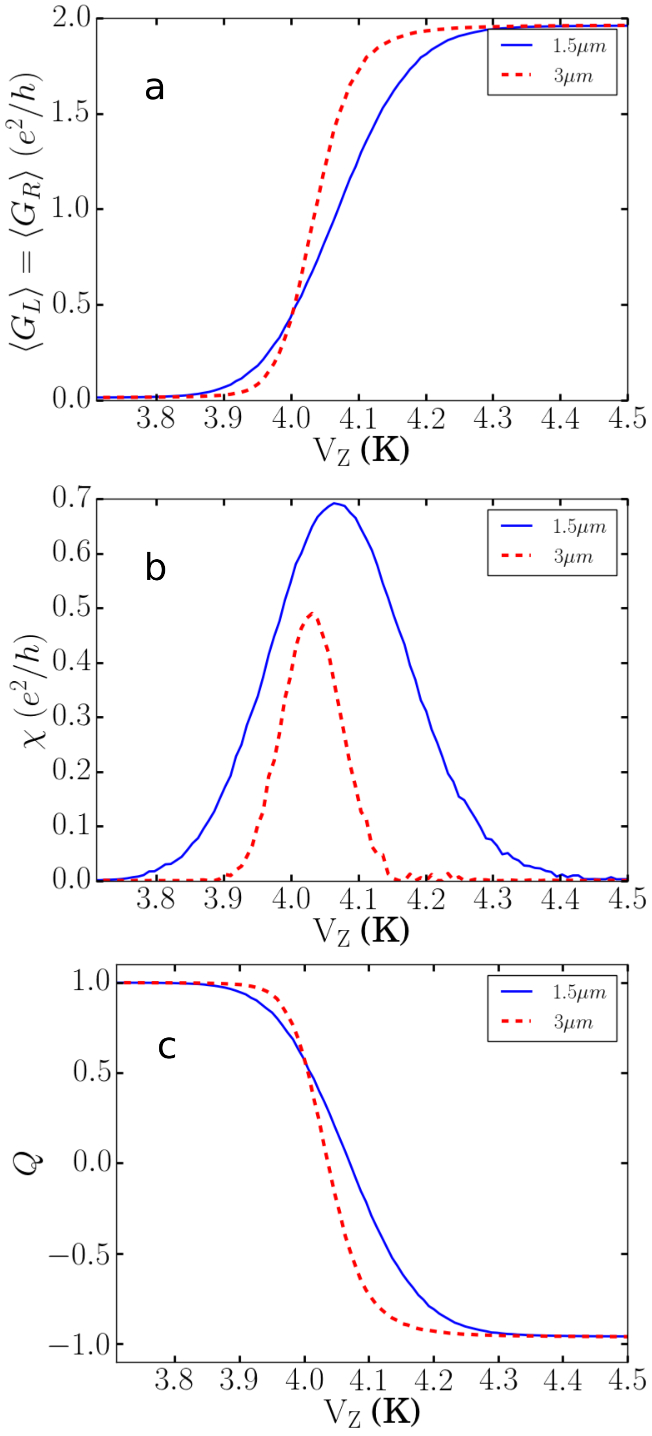

FIGURE 4.4: Plot of certain transport characteristics for the semiconductor nanowire system across TPT for L = 1.5 and 3 μm nanowire with disorder strength corresponding to mean free path $L_{mf} = 1.1\mu$m. Deep in the topological(non-topological) phase, the conductance and the TV saturate to $2e^2/h(0)$ and -1(+1) respectively. The CC (χ) exhibits a peak in the crossover region. For the longer nanowire, the crossover region is narrower compared to the shorter nanowire.

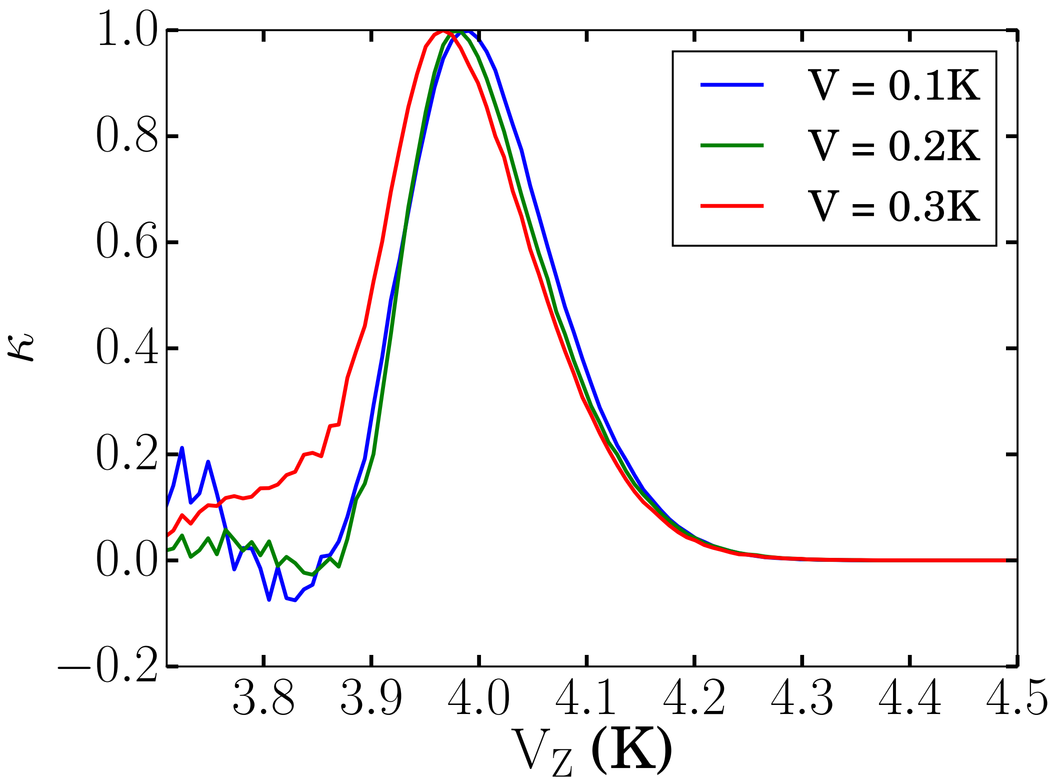

FIGURE 4.5: ZBPC between left and right conductance peaks as a function of V_Z for the same system parameters used to obtain Fig. 4.4 for varying voltages, V. The peak in ZBPC at the TPT shows that Majorana peaks appear in a correlated way.

4.2 Conductance fluctuations in superconductor

In the previous section we showed that for a typical disordered system left and right zero-bias conductance peaks appear simultaneously. One way to quantify such correlated appearance of the zero-bias peak is by calculating the statistical covariance of the left and right conductance over random disordered samples of a given disorder strength. Let us introduce such a measure to quantify conductance correlation(CC) between left and right conductance,

$$\chi = \sqrt{\langle G_L G_R \rangle - \langle G_L \rangle \langle G_R \rangle}. \tag{4.9}$$

The angular brackets represent the average over disorder configurations, and G_L and G_R are calculated zero-frequency left and right conductance values respectively. An experimental signature of the existence of Majorana zero modes is presence of a ZBCP. While the CC defined above quantifies the correlation between left and right conductance, it does not necessarily capture the simultaneous appearance of a conductance *peak* associated with the Majorana modes at the boundary of the nanowire in the topological phase. Thus, we define a quantity that captures the extent of conductance correlation as well as the existence of ZBCP associated with the MZMs as zero-bias-peak-correlation (ZBPC),

$$\kappa(\mathrm{V}) = 1 - \frac{\langle (G_L(0) - G_L(\mathrm{V})) \rangle \langle (G_R(0) - G_R(\mathrm{V})) \rangle}{\langle (G_L(0) - G_L(\mathrm{V}))(G_R(0) - G_R(\mathrm{V})) \rangle}. \tag{4.10}$$

The disorder average is denoted by angular brackets. The ZBPC (κ) as defined depends on the voltage V. Notice, $\kappa \sim 0$ as $\mathrm{V} \to 0$. On the other hand, $\mathrm{V} \ll \Delta$ must be satisfied to ensure ZBPC is sensitive only to correlation present in ZBCPs and has no contribution from the continuum set of states present at energies $\gtrsim \Delta$ where Δ is the induced superconducting gap. Hence an appropriate choice for V is $\mathrm{V} \sim \Gamma$, where Γ is the conductance broadening.

A finite clean nanowire system endowed with dissipative broadening has three distinct regions in the parameter space: a topological phase, a trivial phase and a crossover region intermediate between the topological and the trivial phase as shown in Fig. 4.3. For sufficiently high barrier in the lead-nanowire junction, the conductance deep in the topological phase is $2e^2/h$, whereas deep in the trivial phase it is 0. For every point in parameter space in the crossover region, the conductance evaluates to an intermediate value between 0 and $2e^2/h$.

Disorder introduces sample-to-sample conductance fluctuation. In Fig. 4.4 we have plotted the TV, the disordered averaged conductance and CC for nanowires with two different physical lengths. We observe that for weak disorder (mean-free-path $\sim 1.1\mu\mathrm{m}$) the phase diagram is only weakly different from the clean case. Upon disorder averaging, three distinct regions namely, topological, trivial and crossover can be identified in weakly disordered systems as well. Deep in the topological phase the disorder averaged conductance saturates to $2e^2/h$, whereas deep in the trivial phase, the disorder averaged result saturates to 0. This can be understood based on the fact that, since for every disorder configuration only a slight modification of the phase diagram is allowed, weak disorder does not affect either the deep topological or the trivial region. However, the crossover region is prone to disorder fluctuations. Moreover, notice that a nanowire with a longer physical length has a smaller crossover region. In Fig. 4.5 we plot ZBPC (κ) against Zeeman field for varying voltages V of the order of ZBCP broadening. Observe that ZBPC shows a peak in the crossover region and saturates to 0 in both the trivial and the topological phase. It can be concluded from Fig. 4.4 and 4.5 that the appearance of MZMs at the TPT is linked to the appearance of correlated ZBCPs.

Conductance correlation at the TPT can be understood in terms of statistical properties tunneling conductance of disordered system undergoing a TPT. The reflection matrix appearing at the two ends of the nanowire can be expressed as (see Appendix E)

$$\begin{aligned} r_{maj} &= O_1 \tanh \Lambda O_3 \\ r'_{maj} &= -O_2 \tanh \Lambda O_4 \end{aligned} \tag{4.11}$$

where $O_i \in \mathrm{SO(2N)}$ with N being the number of conducting electron channels in the lead at zero energy and Λ is a real diagonal $2\mathrm{N} \times 2\mathrm{N}$ matrix. The eigenvalues λ_n of Λ matrix are called Lyapunov exponents. For a disordered system, $O_i^\prime s$ are random matrices and the Lyapunov exponents perform a random walk with probability distribution [110]

$$P(\lambda) = \frac{1}{\sqrt{2\pi \tilde{L}\sigma}} e^{-\frac{(\lambda-\xi L)^2}{2\sigma^2 \tilde{L}}} \tag{4.12}$$

where $\tilde{L}$ is some dimensionless parameter proportional to the physical length of the nanowire and ξ is some dimensionless parameter which encodes all physical parameters which can drive the topological phase transition viz. if all parameters in Eq. 4.4 are fixed but only the magnetic field is varied then to drive topological transition then $\xi \sim (V_Z - V_Z^c)/V_Z^c$, where V_Z^c is the critical Zeeman field where the phase transition takes place. Unless otherwise stated we fix the constant parameter controlling the width of the distribution as $\sigma = 1$. A minimal model to understand TPT in the nanowire could begin by the assuming all but at-most one Lyapunov exponents are positive and they can be expected to be much larger than zero. This implies that the λ_n's can be ordered as $|\lambda_1| < \lambda_2 < ..... < \lambda_{2N}$. Thus all but one transmission eigenvalues are close to zero. The crossover of the smallest Lyapunov exponent λ_1 from negative to positive is the signature of phase transition as the topological invariant given by $\mathrm{sgn}(\det(r))$ is solely dependent on $\mathrm{sgn}(\lambda_1)$.

Substituting the expression (4.11) in the Eq. (4.1), the left conductance G_L is obtained in terms of the elements of Λ matrix,

$$\begin{aligned} G_L &= N - \frac{1}{2}\mathrm{Tr}[r_M \tau_y r_M^T \tau_y] \\ &= N - \frac{1}{2}\mathrm{Tr}[\tanh \Lambda O_3 \tau_y O_3^T \tanh \Lambda O_1^T \tau_y O_1] \\ &= N - \frac{1}{2}\sum_{i<j} \zeta_{i,j} R_{i,j}^{(1,3)}. \end{aligned} \tag{4.13}$$

where, $\zeta_{i,j} = \tanh\Lambda_i \tanh\Lambda_j$ and $R_{i,j}^{(1,3)} = [O_3(i\tau_y)O_3^T]_{i,j}[O_1^T(i\tau_y)O_1]_{i,j}$ are random variables independent of Λ_i. Similarly $G_R = N - \sum_{i<j} \tanh\Lambda_i \tanh\Lambda_j R_{i,j}^{(2,4)}$. Since $O_{1,3}$ and $O_{2,4}$ perform random walks in a compact space they can be expected to become uncorrelated at long lengths $\tilde{L} >> 1$. In this limit $R_{i,j}^{1,3}$ and $R_{i,j}^{2,4}$ are uncorrelated random variables and the correlated function of the end conductance can be written as

$$\Delta G_{L,R} = \langle G_L G_R\rangle - \langle G_L\rangle\langle G_R\rangle \tag{4.14}$$

$$= \frac{1}{4}\sum[\langle\zeta_{i,j}\zeta_{k,l}\rangle - \langle\zeta_{i,j}\rangle\langle\zeta_{k,l}\rangle]\langle R_{i,j}^{(1,3)}\rangle\langle R_{k,l}^{(2,4)}\rangle. \tag{4.15}$$

Assuming all Lyapunov exponents λ_i are large positive numbers except at-most one, λ_1. Near the phase transition λ_1 fluctuates near 0 and the conductance becomes correlated as

$$\tilde{\chi} \equiv \sqrt{\Delta G_{L,R}} = \frac{1}{2}\sqrt{\sum_{i,j}(\langle\tanh\lambda_1^2\rangle - \langle\tanh\lambda_1\rangle^2)R_{i,1}^{1,3}R_{j,1}^{2,4}}. \tag{4.16}$$

And the TV can be written as,

$$\tilde{Q} \equiv \det(r_M) = \det(r'_M) = \tanh(\lambda_1). \tag{4.17}$$

4.3 Conductance correlation and topological visibility using random matrix model

Plot of average conductance and CC of the composite *barrier-nanowire-barrier* (see App. E.1 for computing composite S-matrix) as a function of Lyapunov exponent is shown in Fig. 4.6. The average conductance and conductance correlation is obtained by averaging over random orthogonal matrices, $O_i's$ appearing in Eq. (4.14). As the Lyapunov exponent transitions across 0, the find our model calculations show similar trend as exhibited by the nanowire transitioning through the TPT presented in Fig. 4.4.

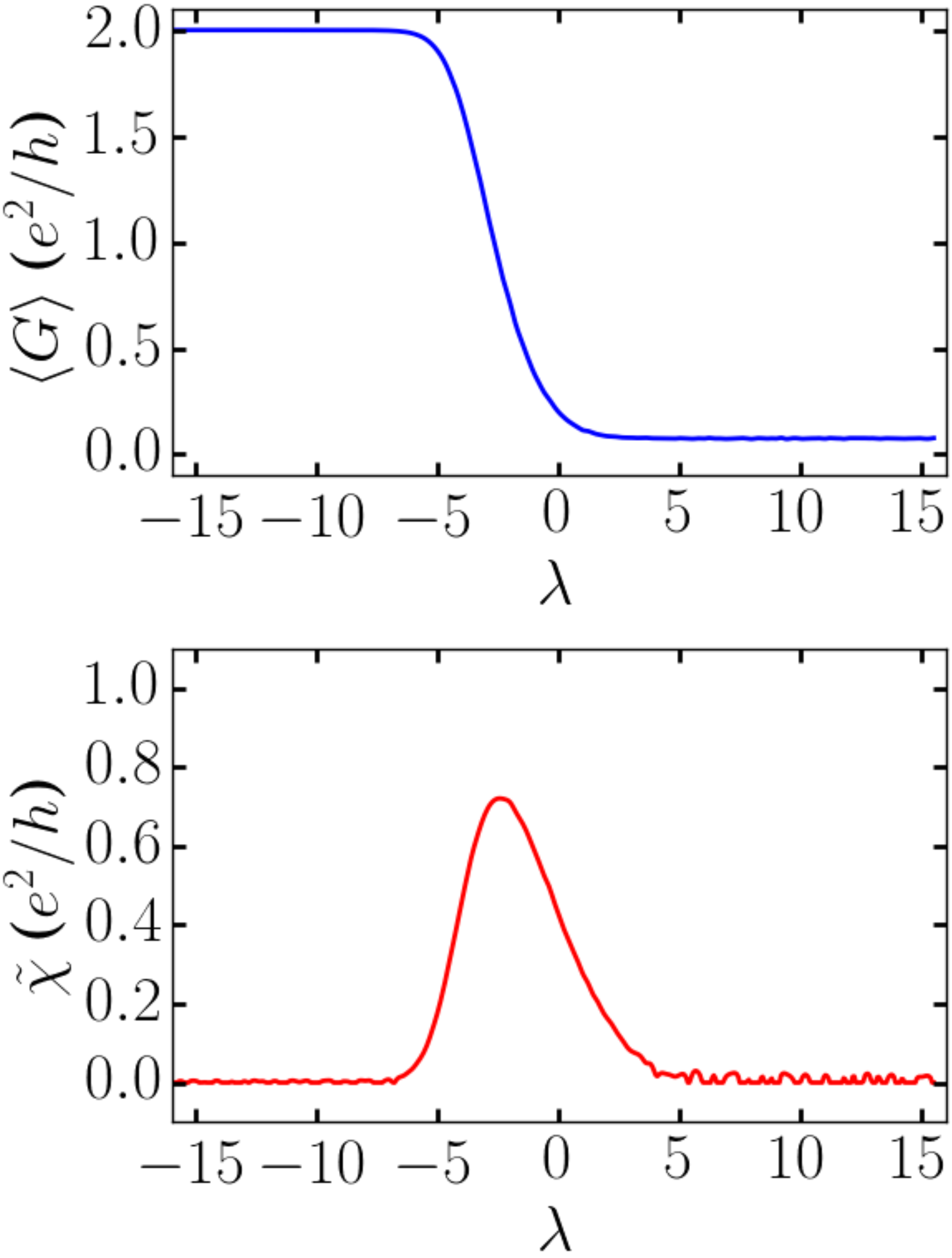

FIGURE 4.6: Average conductance, $\langle G\rangle \equiv \langle G_L\rangle = \langle G_R\rangle$ (top panel) and average CC, $\tilde{\chi}$ (bottom panel) as a function of Lyapunov exponent. Average is calculated over ensemble of random orthogonal matrices (Eq. 4.11). Conductance correlation ($\tilde{\chi}$) peak is associated with the sign change of λ with topological(non-topological) conductance quantization associated with $\lambda < 0$ ($\lambda < 0$).

Specifically, observe that the conductance falls to 0 from $2e^2/h$ as the Lyapunov exponent changes sign. This is consistent with the discussion in Sec. 4.2, where we had concluded that system transitions from topological phase to a trivial phase as the sign of Lyapunov exponent changes from negative to positive.

In this section, we obtain CC, average conductance and the TV using the random matrix model discussed in the previous section. To make comparisons to the numerical results obtained for the nanowire in Sec. 4.1, we keep the number of channels the same, i.e. $N_c = 4$. Accordingly, $O_i \in \mathrm{SO}(8)$ appearing in the Eq. (4.11) and Λ is a real diagonal matrix with eigenvalues $(\lambda, 1, 1, 1, 1, 1, 1, 1)$, where λ is sampled according to the probability distribution appearing in Eq. (4.12). For all the obtained results, $\sigma = 1$ (Eq. (4.12)) is held fixed. Next, we consider a barrier region at the two ends of the nanowire and form a composite *barrier-nanowire-barrier* system. The corresponding composite S-matrix, S_{com} is calculated following the recipe outlined in Appendix E, which is used to obtain the corresponding composite reflection matrix, r_{com} to calculate conductance and CC.

Fig. 4.7 is a plot of conductance and CC ($\tilde{\chi}$) of the composite *barrier-nanowire-barrier* system as a function of drift for different $\tilde{L}$. Since the probability distribution of λ is centered around ξ (Eq. 4.12), qualitative behavior of conductance and CC as a function of ξ and λ are similar. However, unlike λ, ξ is a tunable parameter in an experiment that can drive a system in and out of the topological phase. The width and the height of the correlation peak tend to decrease as a function $\tilde{L}$. This is consistent with the narrower and shorter CC peak observed in Fig. 4.4 for the longer nanowire. In other words, the longer system has a narrower crossover region (Fig. 4.3) at the phase transition. We find that the theoretical model described in Sec. 4.2 captures the qualitative behavior of transport properties across TPT quite well.

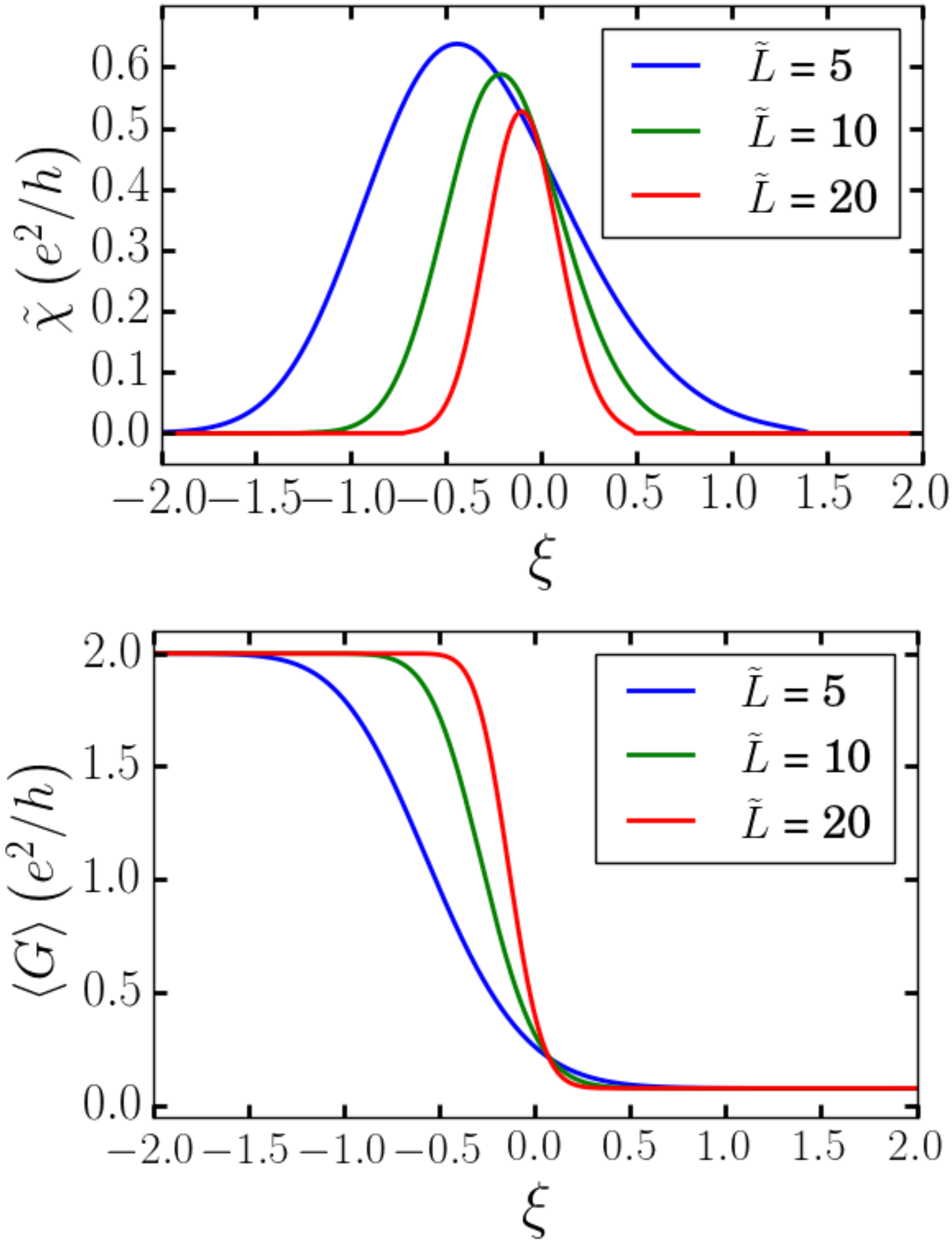

FIGURE 4.7: CC, $\tilde{\chi}$ (top panel) and conductance, G (bottom panel) of the composite *barrier-nanowire-barrier* system as a function of drift, ξ for various length parameter $\tilde{L}$. This result is obtained by averaging CC and conductance (Fig. 4.6) over Lyapunov exponents sampled from the probability distribution given by Eq. (4.12) for a given ξ and $\sigma = 1$. The width and the height of conductance correlation peak is a decreasing function of $\tilde{L}$.

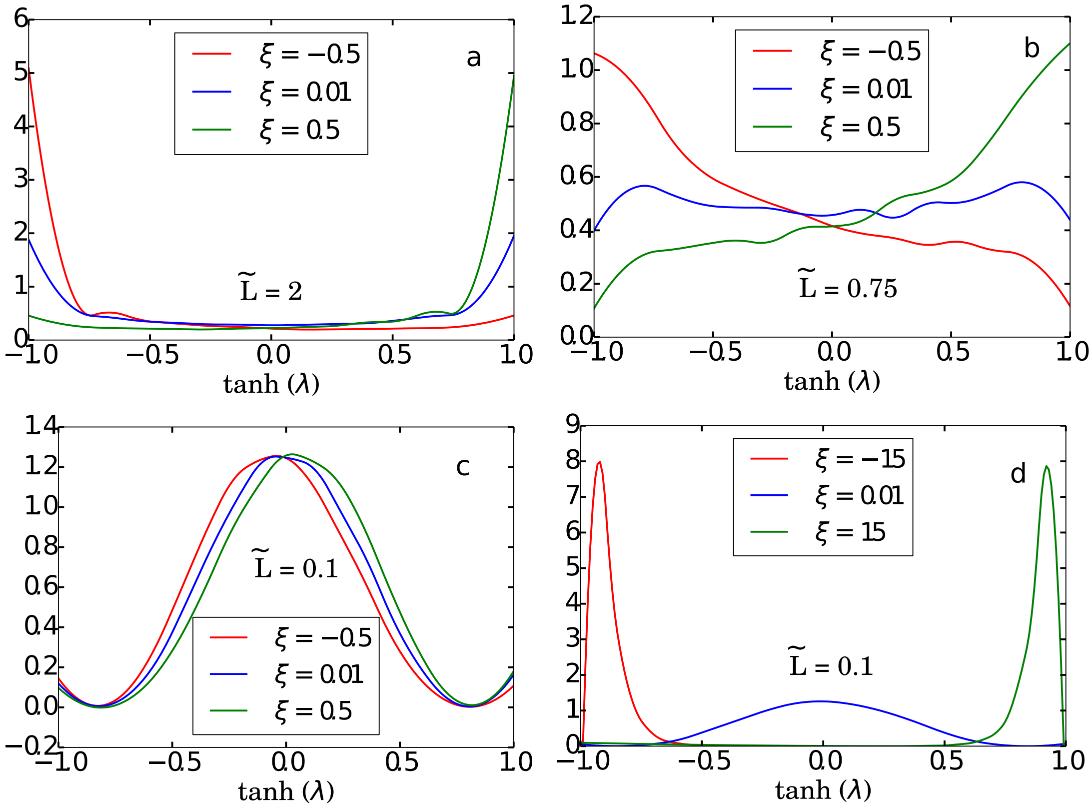

FIGURE 4.8: Probability of distribution of tanh(λ) for λ sampled from the distribution in Eq. (4.12) for various drift (ξ) and length ($\tilde{L}$) parameters. In the theoretical model discussed in Sec. 4.2 tanh(λ) equals TV. For fixed set of drift parameter values, ξ, as the system size decreases (panel a-c), the distribution of TV de-localizes. The distribution of TV close to TPT is bimodal for $\tilde{L} = 2$ and unimodal for $\tilde{L} = 0.1$

The characteristics of a topological phase transition in a finite disordered nanowire can be understood by studying the probability distribution of topological visibility $Q = \tanh(\lambda)$ across the phase transition for varying nanowire length ($\tilde{L}$) and drift (ξ) parameters.

Probability distribution of tanh(λ), where the Lyapunov exponent λ follows the probability distribution in Eq. 4.12, is plotted in Fig. 4.8 for various drift (ξ) and length ($\tilde{L}$) parameters. In each panel of Fig. 4.8 the probability distribution is studied for a fixed length parameter $\tilde{L}$ across the TPT as ξ changing sign (tanh(λ) equals TV in our model). In Fig. 4.8a, for $\xi = -0.5(\xi = 0.5)$, tanh(λ) is sharply localized at -1(+1) suggesting the $\xi = -0.5(\xi = 0.5)$ corresponds to a well-defined (non-)topological phase. As $\xi \sim 0$ the transition from sharp localization at -1 to sharp localization +1 occurs through the formation of a bimodal distribution peaked at ± 1. As $\tilde{L}$ is reduced in Fig. 4.8b, the localized peaks of the distribution broadens leading to complete vanishing of distinctions between the two phases for $\tilde{L} = 0.1$ in Fig. 4.8c. This implies that the size of the cross-over region (Fig. 4.3) increases as $\tilde{L}$ (which is proportional to physical length L) decreases. Notice, as $\tilde{L}$ decreases in Fig. 4.3a-c, the bimodal distribution of tanh(λ) at $\xi \sim 0$ in Fig. 4.3a turns into a unimodal distribution centered at 0 in Fig. 4.3c. The sharply localized distribution of tanh(λ) is recovered $\tilde{L} = 0.1$ when $|\xi| \gg 0$ shown in Fig. 4.3d.

4.4 Summary

The topological transition in nanowire heterostructures discussed in this thesis is associated with simultaneous appearance of a pair of Majorana zero modes. Thus, both left and right conductance should show signatures of perfect Andreev reflection associated with the Majorana modes, simultaneously. We propose that measurement of such conductance correlation can be used as a general diagnostic tool to detect topological phase transition in nanowire systems. By considering a realistic system within experimentally relevant parameters- a disordered quasi one-dimensional nanowire, we quantitatively established that an appropriately defined conductance correlation shows a peak in the crossover region of the phase transition, where the phase transition itself was monitored by calculating topological visibility.

Theoretically, within a very general minimal model that respects the symmetry properties of a multi-channel disordered nanowire system (class D), we were able to qualitatively demonstrate that indeed conductance correlation can be used as a probe to detect topological phase transitions. Our model was able to reproduce the qualitative features of the nature of the topological phase transition in detail.

Chapter 5: Discussion

In chapter 2 we found that while a Bosonic bath does not directly interfere with topological protection of quantum information, Bosonic baths can lead to powerlaw in time diabatic errors that might limit the speed of topologically protected operations. We ignored finite temperature effects despite the fact that a finite temperature is needed to justify the Markovian approximation. Such finite temperature effects can be expected to be negligible for temperatures substantially below the gap. Moreover, such finite temperature excitations are expected to only increase the excitation probability and thus the error rate.

In chapter 3 we quantitatively related the observed non-ideal characteristics of a zero-bias conductance-peak, in terms of height and width of the peak controlled by Majorana splitting and dissipation, to topological visibility. This connection shed light on the possibility of observing the topological nature of MZMs (in terms of non-Abelian exchange statistics) in future braiding experiments carried out in the same (or similar) samples as the ones currently manifesting non-ideal ZBCPs. This takes on special significance because direct braiding experiments, which are typically very hard, establishing the non-Abelian nature of MZMs have not yet been carried out in semiconductor nanowires (such experiments do exist in the fractional quantum Hall context, but the results are difficult to interpret and have remained controversial (see Ref. [111] and references therein). Note that we have neglected finite temperature and disorder effects in our theory, assuming clean nanowires at zero temperature. However, our conclusion remains completely unaffected by finite temperature and disorder. Finite temperature only reduces the visibility, thus further reducing the magnitude of the ZBCP and the TV. Thus, the braiding experiment should be performed at the lowest possible temperatures to maximize the visibility. Disorder complicates matters only because it shifts the condition for obtaining the topological phase (i.e. the TPT point), but it cannot affect the basic physics at all since the induced topological superconductivity arises from an interplay among the s-wave superconductivity, spin-orbit coupling, and Zeeman splitting—all of which are immune to disorder. The situation with very strong disorder is, however, disastrous for the manifestation of topological properties since the strongly disordered nanowire will manifest Griffiths phase physics with many MZMs localized randomly along the wire [90, 112], and this situation must obviously be avoided at all costs for all braiding experiments. Similarly, multisubband occupancy of the nanowire [106, 113] does not change any of our conclusions either as long as an odd number of spin-split subbands are occupied in the system, and the appropriate microscopic parameters (i.e. δ, Γ, Γ_L, Δ, chemical potential) are all modified to take into account the multisubband occupancy in the nanowire. Of course, the relative values of the various parameters may be modified by multi-subband occupancy, which must be incorporated in the theory appropriately, but the theory itself remains exactly the same as long as an odd number of subbands are occupied in the nanowire and various parameters are appropriately modified to reflect the multi-subband occupancy of the system.

In chapter 4, we demonstrated that correlation calculated between independent left and right tunneling conductance measurement shows a peak in the vicinity of topological phase transition associated with simultaneous appearance of Majorana mode at each edge of the nanowire. Therefore, such a measurement of correlation can be used as a tool diagnose topological phase transition and thereby decide whether or not the observed zero-bias conductance-peak in the experimental measurements are due to underlying Majorana modes.

Appendix A: Reduced master equation from parity conservation

In this section we discuss the consequence of parity conservation on the master equation(Eq. 2.13). Using Eq. 2.2, Fermionic parity operator, $\hat{P} = i\gamma_0\gamma_x\gamma_y\gamma_z$ can be written as,

$$\hat{P} = \tau_z. \tag{A.1}$$

Clearly, $[P, H] = 0$. Therefore, in absence of system-bath coupling, the system dynamics is entirely governed by the effective Hamiltonian,

$$H_{2Level} = \mathbf{B}(t).\sigma.$$

Hence, the Hamiltonian is reduced to a matrix in $SU(2)$ space from $SU(2) \otimes SU(2)$. However, it is not obvious if such dimensional reduction is well-defined for the master equation in presence of a bath even if the thermal bath conserves parity (i.e. H_{SB} and H_B commute with the parity operator, P). In what follows, we show that indeed the system dynamics can be studied solely in $SU(2)$ space rather that $SU(2)\otimes SU(2)$. Without loss of generality we focus on the first step, i.e. $t \in [0, T]$.To proceed we use the standard stochastic wavefunction interpretation of the master equation. We refer the reader to literature [114, 115] for a detailed exposition while we outline the basic idea here. Expanding the density matrix as an ensemble of pure states, $\rho_S(t) = \sum_j p_j |\psi_j(t)\rangle\langle\psi_j(t)|$, the master equation can be expressed as

$$\begin{aligned}\dot{\rho_S}(t) = &\sum_j p_j \Big[-i(H_{eff}|\psi_j\rangle\langle\psi_j| - |\psi_j\rangle\langle\psi_j|H^\dagger_{eff}) \\ &+ \sum_{k,\nu} \eta_k(\nu) J_k(\nu)|\psi_j\rangle\langle\psi_j|J_k(\nu)^\dagger\Big],\end{aligned}$$

where $H_{eff} = H - i\sum_{k,\nu}\frac{\eta_k(\nu)}{2}J^\dagger_k(\nu)J_k(\nu)$. Thus, ρ can constructed from an ensemble average of pure states $|\psi_j(t)\rangle$ evolving under the influence of an effective non-unitary Hamiltonian H_{eff}, while at each time t, there is a probability proportional to $\eta_k(\nu)$ to *jump* to a different state $J_k(\nu)|\psi_j(t)\rangle$. Diagonalize the Hamiltonian in the parity basis such that the degenerate ground states are given by $|0\rangle$ and $|0'\rangle$ and the degenerate excited states be given by $|1\rangle$ and $|1'\rangle$, with,

$$\begin{aligned}\hat{P}|0\rangle = 1 \quad &; \quad \hat{P}|0'\rangle = -1 \\ \hat{P}|1\rangle = 1 \quad &; \quad \hat{P}|1'\rangle = -1. \end{aligned} \tag{A.2}$$

Let any two arbitrary ground states be given by,

$$\begin{aligned}|G\rangle &= \alpha|0'\rangle + \beta|0\rangle \\ |G'\rangle &= \alpha'|0'\rangle + \beta'|0\rangle\end{aligned} \tag{A.3}$$

We show that there is no sequence of jump operators that lead to $|G\rangle \to |G'\rangle$ transition. Since a similar result extends to excited states, combined with $\langle G|H_{eff}|G'\rangle = 0$, the condition implies that the system can be effectively studied in $SU(2)$ space as a two-level system.

H commutes with the Majorana operator, γ_z. In the Pauli matrix notation, it can be expressed as,

$$\gamma_z = \sigma_z \tau_x. \tag{A.4}$$

Notice,

$$\{\hat{P}, \gamma_z\} = 0. \tag{A.5}$$

Let the system-bath Hamiltonian given by $H_{sb} = \sum_i \hat{A}_i \hat{\Gamma}_i$ with $\hat{A}_i$ and $\hat{\Gamma}_i$ being the system and bath operators respectively, such that

$$\begin{aligned} &[H, \hat{P}] = [H, \gamma_z] = 0 \\ &[\hat{A}_i, \hat{P}] = [\hat{A}_i, \gamma_z] = 0 \quad \forall i. \end{aligned} \tag{A.6}$$

Consider zero energy jump operators,

$$J_i(0) = \Pi_g \hat{A}_i \Pi_g + \Pi_e \hat{A}_i \Pi_e \tag{A.7}$$

where, Π_g and Π_e are projection operators to ground and excited state eigenspace, respectively. Note that $\langle G'|\hat{A}_i|G\rangle = 0$ is sufficient to show that $\langle G'|J_i(0)|G\rangle = 0$.

$$\begin{aligned} \langle G'|\hat{A}_i|G\rangle = &(\alpha')^*\alpha\langle 0|\hat{A}_i|0\rangle + (\alpha')^*\beta\langle 0|\hat{A}_i|0'\rangle \\ &+ (\beta')^*\alpha\langle 0'|\hat{A}_i|0\rangle + (\beta')^*\beta\langle 0'|\hat{A}_i|0'\rangle. \end{aligned} \tag{A.8}$$

Using $\{\hat{P}, \gamma_z\} = 0$ and $[\gamma_z, H] = 0$, we conclude $\gamma_z|0\rangle = |0'\rangle$. Hence, sum of first and the last term of the above equation reduce to $(\alpha')^*\alpha + (\beta')^*\beta = 0$ (using $\langle G'|G\rangle = 0$). Now consider $\langle 0'|\hat{A}_i|0\rangle = \langle 0'|\hat{A}_i\hat{P}|0\rangle = \langle 0'|\hat{P}\hat{A}_i|0\rangle = -\langle 0'|\hat{A}_i|0\rangle$. Thus $\langle 0'|\hat{A}_i|0\rangle =$

$\langle 0|\hat{A}_i|0'\rangle = 0$. Therefore,

$$|G\rangle \xrightarrow{J_i(0)} |G\rangle \quad \forall i. \tag{A.9}$$

Similarly we can show,

$$|E\rangle \xrightarrow{J_i(0)} |E\rangle \quad \forall i, \tag{A.10}$$

where $|E\rangle$ is some excited state.

Consider a positive energy jump operator that takes the system from ground state eigenspace to excited eigenspace,

$$J_i = \Pi_e \hat{A}_i \Pi_g. \tag{A.11}$$

Consider the process,

$$|G\rangle \xrightarrow{J_i}\xrightarrow{J_j^\dagger} \tag{A.12}$$

for any two i and j possibly being the same. In general these operators can be expressed as,

$$\begin{aligned} J_i &= A_i'|1'\rangle\langle 0'| + A_i|1\rangle\langle 0| \\ J_j &= A_j'|1'\rangle\langle 0'| + A_j|1\rangle\langle 0|, \end{aligned} \tag{A.13}$$

with

$$\begin{aligned} A_i &\equiv \langle 1|\hat{A}_i|0\rangle \quad ; \quad A_i' \equiv \langle 1'|\hat{A}_i|0'\rangle \\ A_j &\equiv \langle 1|\hat{A}_j|0\rangle \quad ; \quad A_j' \equiv \langle 1'|\hat{A}_j|0'\rangle. \end{aligned} \tag{A.14}$$

Then the process is described by the operator,

$$J_j^\dagger J_i = A_j^* A_i |0\rangle\langle 0| + (A_j')^* A_i' |0'\rangle\langle 0'|. \tag{A.15}$$

However, using $\gamma_z|0\rangle = |0'\rangle$ and $\gamma_z|1\rangle = |1'\rangle$ we find $A_i = A_i'$ and $A_j = A_j'$. Thus,

$$J_j^\dagger J_i \propto \Pi_g. \tag{A.16}$$

Thus we have shown that there is no sequence of jump processes that mix orthogonal states in an energy eigenspace.

Appendix B: Diabatic expansion of Bloch vector

Expanding the Bloch vector $R(s)$ in powers of $\epsilon = 1/T$,

$$R(s) = R_0(s) + \epsilon R_1(s) + \dots \tag{B.1}$$

we seek solution to

$$\epsilon \dot{R} = MR \tag{B.2}$$

for initial condiction $R(0) = R_0(0) \equiv \mathbf{B}(0)$ where, $M = 2(A+S)$ and $S = (\alpha - \beta)A^2$ (A being the matrix representation of $\mathbf{B}\times$ operation) with α and β being the time-dependent functions defined by Eq. 2.20. The presentation here follows the work of Hagedorn *et. al.* in Ref. [76].

A, being the anti-symmetric matrix representation of $\mathbf{B}\times$ operator has eigenvalues $0, i, -i$. Consequently, the instantaneous eigenvalues of M are given by $0, \lambda_1 \text{and} \lambda_2$ with,

$$\begin{aligned} \lambda_1 &= 2(i - (\alpha - \beta)) \\ \lambda_2 &= 2(-i - (\alpha - \beta)). \end{aligned} \tag{B.3}$$

Denote $R_0(s) = -\mathbf{B}(s)$ and thereby, $R_0(s)$ is the zero eigenvector with 0 eigenvalue. M can be inverted in the eigenvector subspace with non-zero eigenvalues,

$$M^{-1} = \frac{1}{2(1 + (\alpha - \beta)^2)}(-A - (\alpha - \beta)\mathbb{1}). \tag{B.4}$$

Expanding $R = R_0 + \epsilon R_1 + \ldots$ and substituting in $\epsilon\dot{R} = MR$, we get,

$$\begin{aligned} MR_j &= \dot{R}_{j-1} \\ \implies R_j &= f_{j-1}R_0 + M^{-1}\dot{R}_{j-1} \end{aligned} \tag{B.5}$$

with $f_{j-1}(s)$ evaluated using the condition $R_0^{\mathrm{T}}\dot{R}_j = 0$ which follows from $MR_j = \dot{R}_{j-1}$,

$$f_{j-1}(s) = \int_0^s ds\, \dot{R}_0^T M^{-1}\dot{R}_{j-1}. \tag{B.6}$$

Now we show that the series expansion is well-defined in small epsilon limit. Consider the partial sum of the series expansion,

$$R^N(s) = \sum_{j=0}^{N} \epsilon^j R_j. \tag{B.7}$$

If the series expansion is well-defined, the partial sum (as defined above) must converge to the actual solution R. Let the actual solution $R(s) = V(s)R(0)$. Consider,

$$\begin{aligned} \left\|R^N(s) - R(s)\right\| &= \left\|R^N(s) - V(s)R(0)\right\| \\ &= \|V(s)\| \left\|V(s)^{-1}R^N(s) - R(0)\right\| \\ &= \|V(s)\| \left\| \int_0^s ds' \frac{d}{ds'} V^{-1}(s')R^N(s') \right\|, \end{aligned} \tag{B.8}$$

where we have used $\dot{V}^{-1}(0) = 0$ which follows from $\dot{\mathbf{B}}(0) = 0$. Now,

$$\begin{aligned} \dot{R}^N(s) &= \sum_{j=0}^{N} \epsilon^j \dot{R}_j = \sum_{j=0}^{N} \epsilon^j M R_{j+1} \\ \implies \epsilon \dot{R}^N(s) &= M \sum_{j=0}^{N} \epsilon^{j+1} R_{j+1} + M R_0 - M R_0 \\ &= M R^{N+1} = M R^N + \epsilon^{N+1} \dot{R}_N, \end{aligned} \tag{B.9}$$

where we simply used the definition given in Eq. B.7 and the relation given in Eq. B.5 to arrive at the second line above. Using the above relation we get,

$$\frac{d}{ds'}(V^{-1}(s')R^N(s')) = \dot{V}^{-1}R^N + V^{-1}\dot{R}^N = \epsilon^N \dot{R}_N. \tag{B.10}$$

Therefore it follows from Eq. B.8,

$$\begin{aligned} \left\|R^N(s) - R(s)\right\| &= \|V(s)\| \left\| \int_0^s ds' \epsilon^N \dot{R}_N \right\| \\ &\le \epsilon^N \|V(s)\| \int_0^s ds' \left\| \dot{R}_N \right\|. \end{aligned} \tag{B.11}$$

We conclude that R^N converges to the actual solution R provided $\left\|\dot{R}_N\right\|$ and $\|V(s)\|$ are bounded. We refer the reader to Ref. [76] for the proof of boundedness of $\left\|\dot{R}_N\right\|$ in absence of bath. It seems likely that a similar proof holds for boundedness of $\left\|\dot{R}_N\right\|$ in presence of bath. In the limiting $\alpha(s) = \beta(s) = 0$, $V(s)$ is unitary, so clearly when for $\alpha(s) > \beta(s) \forall s$, $\|V(s)\|$ is bounded by 1. Without speculating about $\alpha(s) < \beta(s)$ case, we restrict our following discussion to $\alpha(s) > \beta(s)$ that corresponds to $\eta_0 \geq \eta$ provided $s_x \sim s_y$.

Our goal now is to arrive at a bound for the diabatic error defined by,

$$\mathcal{E} = \|R(1) - R_0(1)\|, \tag{B.12}$$

where $R_0(s=1) = -\mathbf{B}(s=1)$ is the Bloch vector that corresponds to instantaneous zero eigenvector of M at $s=1$. Note as consistency check that $R(1) \to R_0(1)$ when $\epsilon = 1/T \to 0$ follows from the series expansion of R, Eq. 2.29. Since we have shown that the series expansion of R is well defined, we can replace R in $\|R(1) - R_0(1)\|$ by its corresponding series expansion. However to make progress towards arriving at a bound for $\mathcal{E}$ we need a useful result stated and proved below.

We how that if all derivative of M (k^{th} derivative denoted by $M^{(k)}$), $M^{(k)}(s_0) = 0 \forall\, k$ for some s_0 then $(R_0^{\perp})^T R_j^{(k)} = 0 \forall\, k, j$ where $R_0^{\perp}$ is any vector such that $(R_0^{\perp})^T R_0 = 0$. The proof follows in three steps:

- We first show that $(R_0^{\perp})^T R_0^{(k)} = 0 \forall\, k$.
  Let k be a positive integer. $MR_0 = 0 \implies (MR_0)^{(k)} = \sum_{j=0}^{k} \binom{k}{j} M^{(j)} R_0^{(k-j)} = MR_0^k = 0$. Therefore, it must be $(R_0^{\perp})^T R_0^{(k)} = 0 \forall\, k$.

- Next we show that $[M^{-1}]^{(k)}(s_0) = 0 \forall\, k$.
  Again, let k be a positive integer. $M^{-1}M = 1 \implies (M^{-1}M)^{(k)} = \sum_{j=0}^{k} \binom{k}{j} [M^{-1}]^{(j)} A^{(k-j)} = [M^{-1}]^{(k)} M = 0$. Therefore, it must be $[M^{-1}]^{(k)}(s_0) = 0 \forall\, k$.

- Finally we prove our original assertion, $(R_0^{\perp})^T R_j^{(k)} = 0 \forall\, k, j$.
  We will prove this assertion by induction. Assume $(R_0^{\perp})^T R_{j-1}^{(k)} = 0 \forall\, k$. Now,

$$\begin{aligned} R_j &= f_{j-1} R_0 + M^{-1} \dot{R}_{j-1} \\ \implies R_j^{(k)} &= (f_{j-1} R_0)^{(k)} + (M^{-1} \dot{R}_{j-1})^{(k)} \\ &= M^{-1} \dot{R}_{j-1}^{(k)} = M^{-1} R_{j-1}^{(k+1)}. \end{aligned}$$

Using the the induction hypothesis it follows, $(R_0^{\perp})^T R_j^{(k)} = 0 \forall\, k, j$.

Since $M^{(k)}(s_0) = 0; \quad s_0 \in \{0,1\} \forall k$ on account of $\frac{d^k}{ds^k}\mathbf{B}(s_0) = 0; \quad s_0 \in \{0,1\} \forall k$, the above result implies $R(1)||R_0(1)$ and $R(0)||R_0(0)$. Armed with this result, we use to Eq. B.11 to arrive at a bound for $\mathcal{E}$ for two different cases, i.e, in absence and in presence of a thermal bath.

B.0.1 Absence of thermal bath

In absence of thermal bath M is anti-symmetric and consequently V is unitary. Thus, Eq. B.11 reduces to

$$\left\|R^M(s) - R(s)\right\| \leq \epsilon^M \int_0^s ds' \left\|\dot{R}_M\right\|. \tag{B.13}$$

Consider the expression $\|R(1) - R_0(1)\|$, using triangle inequality we can express,

$$\|R(1) - R_0(1)\| \leq \|R(1) - R^M(1)\| + \|R^M(1) - R_0(1)\|. \tag{B.14}$$

Using $R^M(1) \parallel R_0(1)$ on account of all derivatives of $M(s)$ vanishing at $s = 1$,

$$\begin{aligned} \|R^M(1) - R_0(1)\| &= \|R_0\|R^M(1)\| - R_0(1)\| \\ &= |\|R^M(1)\| - 1| \\ &\leq \|R^M(1) - R(1)\|, \end{aligned} \tag{B.15}$$

where crucially, we have used $\|R(1)\| = 1$ as time-evolution is unitary for anti-symmetric M to go from the second to the last line on the LHS above.

Using Eq. B.13 we get,

$$\|R(1) - R_0(1)\| \leq 2\epsilon^M \int_0^1 ds' \left\| \dot{R}_M \right\|. \tag{B.16}$$

B.0.2 Presence of thermal bath

Again, using triangle inequality,

$$\|R(1) - R_0(1)\| \leq \|R(1) - R^N(1)\| + \|R^N(1) - R_0(1)\|. \tag{B.17}$$

Using $R^N(1) \parallel R_0(1)$ on account of all derivatives of $M(s)$ vanishing at $s = 1$,

$$\begin{aligned} \|R^N(1) - R_0(1)\| &= \|R_0(1)\|R^N(1)\| - R_0(1)\| \\ &= |\|R^N(1)\| - 1| \\ &= |\epsilon f_0(1) + \epsilon^2 f_1(1) + \dots| \\ &\simeq \epsilon |f_0(1)| \\ \implies \|R(1) - R_0(1)\| &\simeq \epsilon |f_0(1)|. \end{aligned} \tag{B.18}$$

Appendix C: Asymptotic behavior of diabatic error

We consider the error $\mathcal{E}$ in the presence of small but finite relaxation. To proceed it is useful to consider a matrix $V(s)$ with initial condition $V(0) = \mathbb{1}$, that satisfies

$$\dot{V} = \frac{1}{\epsilon} M V, \tag{C.1}$$

where M is the matrix appearing in Bloch equation (Eq. 2.22). Using V we change to change to a new variable ξ,

$$\xi(s) = V^{-1}(s) R(s), \tag{C.2}$$

that satisfies,

$$\epsilon \dot{\xi} = -4\beta \xi + 4\beta V^{-1} R_0. \tag{C.3}$$

The solution to this equation is written as,

$$\begin{aligned} \xi(s) &= e^{-\frac{1}{\epsilon}\int_0^s 4\beta(s')ds'} \\ &\left(\int_0^s \frac{4\beta(s')}{\epsilon} e^{\frac{1}{\epsilon}\int_0^{s'} 4\beta(s'')ds''} V^{-1}(s') R_0(s') ds' + R(0) \right) \end{aligned} \tag{C.4}$$

which in conjunction with Eq. C.2, formally (i.e. contingent on having a solution for $V(s)$ in Eq. C.1) solves the Bloch equation (Eq. 2.22). Note that Eq. C.4 is completely consistent with our discussion in the previous sections since setting $\beta = 0$ in Eq. C.4

and using Eq. C.2 leads to the solution $R(s) = V(s)R(0)$ where using Eq. C.1 we find that R satisfies the same Bloch equation, Eq. 2.26 as used in previous section.

For finite relaxation, the first term in the parenthesis in Eq. C.4 is non-zero and hence the matrix $V(s)$ (or equivalently $V^{-1}(s)$) must be known to calculate $R(1)$. However, $V(s)$ satisfying Eq. C.1 with initial condition $V(0) = \mathbb{1}$ does not lend itself to a power series expansion in ϵ parallel to Eq. 2.27, invalidating the method used to obtain analytical solution for the Bloch vector in the previous section. Though there is no clear way to calculate the matrix $V(s)$ by solving Eq. C.1, computing $\bar{R}$, the action of matrix $V(s)$ on the initial Bloch vector $R_0(0)$,

$$\bar{R} = VR_0(0) \tag{C.5}$$

is analytically tractable. The solution for the vector $\bar{R}$ through Eq. 2.26 allows us to make an ansatz for $V(s)$ that leads to results consistent with numerics.

While a direct solution of V in Eq. C.1 is difficult, we observe that the introduction of a finite relaxation does not change the solution for $\bar{R}$ in Eq. 2.26 except replacing $\alpha \to \alpha - \beta$. Therefore generalizing Eq. 2.32 we get, $\bar{R}(1) = f(s)R_0(1)$ where $f(s)$ is given by Eq. 2.33 but unlike previous section β is no longer assumed to be zero. Using Eq. C.5, this relation can be used to constrain $V(s)$ according to the relation

$$V(1)R_0(0) = f(1)U_0(1)R_0(0) \tag{C.6}$$

where we have used the relation $R_0(s) = U_0(s)R_0(0)$ where U_0 is defined in Eq. 2.37.This motivates our anstaz

$$V(s) \approx f(s)U_0(s) \tag{C.7}$$

in Eq. C.4 which interpolates correctly, satisfying the initial condition $V(0) = \mathbb{1}$ at $s = 0$ as well as Eq. C.6 at $s = 1$. Note that, the above approximation satisfies $V(s) \to U_0(s)$ as $T \to \infty$.

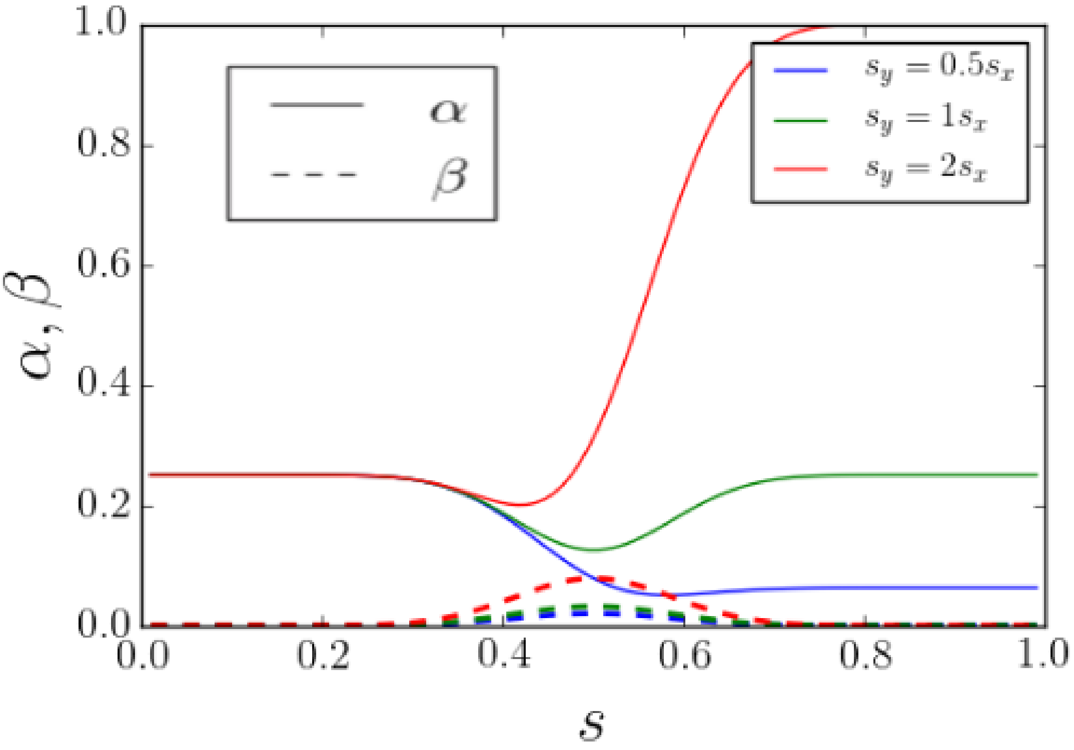

FIGURE C.1: Plot of effective dephasing (α) and relaxation (β) as a function of scaled time, s for system-bath coupling strength $s_x = 0.5$ and s_y given in the key. The dashed curve corresponds to effective relaxation, β and the solid curve corresponds to effective dephasing, α. The dephasing parameter, η_0 and the relaxation parameter η are chosen equal to each other and set to 1.

Substituting Eq. C.7 in Eq. C.4, we make the the following ansatz,

$$\begin{aligned} R(1) &= U_0 f(1) e^{-\frac{4}{\epsilon}\int_0^1 \beta} \left(\frac{4}{\epsilon} \int_0^1 \beta e^{\frac{4}{\epsilon}\int_0^s \beta} f^{-1}(s) + 1 \right) R(0) \\ &= \left(1 + f(1) \int_0^1 \left(\frac{d}{ds} f^{-1} \right) e^{-\frac{4}{\epsilon}\int_s^1 \beta} ds \right) R_0(1). \end{aligned} \tag{C.8}$$

Restricting f and f^{-1} in the above formula to lowest order in ϵ , we get $\|R(1)\| = 1 + \int_0^1 \left(\frac{d}{ds} f_0^{-1}\right) e^{-\frac{4}{\epsilon}\int_s^1 \beta} ds$ where

$$f_0(s) = -\int_0^s \frac{(\alpha-\beta)\omega^2}{2(1+(\alpha-\beta)^2)}. \tag{C.9}$$

As a consistency check note that Eq.C.8 reduces to Eq, 2.32 in the limit $\beta \to 0$. Moreover, since R must be bounded in norm $\|R(1)\| \leq 1$, $\frac{(\alpha-\beta)\omega^2}{2(1+(\alpha-\beta)^2)} > 0$ must hold. This condition suggests the requirement $\alpha > \beta$ for the ansatz offered in Eq. C.8 to hold. We point out that $\alpha > \beta$ condition can be satisfied provided the two system-bath coupling parameters have same order of magnitude, $s_x \sim s_y$ and dephasing strength is stronger than relaxation, $\eta_0 \geq \eta$. This is clear from the Fig. C.1, where we plot effective relaxation and effective dephasing as defined in Eq. 2.20. The dephasing parameter, η_0 and the relaxation parameter, η are chosen as, $\eta_0 = \eta = 1$. For all the curves, $s_x = 0.5$. We have chosen to vary just s_y because both α and β are invariant under combined effect of reflection about $s = 0.5$ and $s_x \rightleftarrows s_y$ exchange. We see that for wide-ranging values of s_y, $\alpha(s) > \beta(s) \forall s \in [0,1]$. Thus we conclude, for comparable values of system-bath coupling strengths, $s_x \sim s_y$, $\eta_0 > \eta$ is a good criterion to ensure $\alpha(s) > \beta(s) \forall s \in [0,1]$.

Using Eq. C.8, the error may be computed as

$$\mathcal{E}(T) = \|R(1) - R_0(1)\| \approx -\frac{1}{T}\int_0^1 \dot{f}_0 e^{-4T\int_s^1 \beta} ds, \tag{C.10}$$

with $\dot{f}_0 = \frac{(\alpha-\beta)\omega^2}{2(1+(\alpha-\beta)^2)}$ and α,β being defined according to Eq. 2.20.

Now, we estimate the exponent of T which governs the power-law dependence of $\|R(1) - R_0(1)\| = \mathcal{E}$ for large T. For our convenience we will restrict ourselves to the special case $s_x = s_y$, (see Eq. 2.22-2.21) essentially allowing the system bath coupling

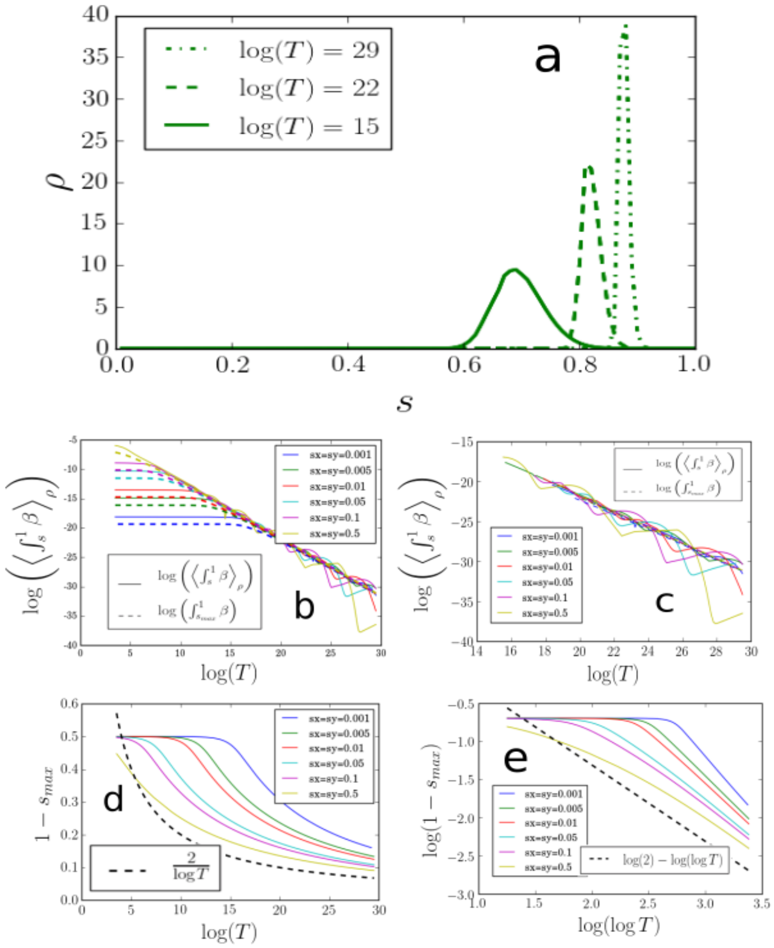

FIGURE C.2: (Panel a) Plot of ρ (Eq.C.13) for different values of time T. Peak-height and the width of the probability density ρ is an increasing and a decreases function of T, respectively. The probability densities look identical at this scale for values of $s_x = s_y$ varied from 0.005 to 0.5. (Panels b and c) Comparison of $\left\langle \int_s^1 \beta \right\rangle_\rho$ (defined by Eq. C.14) , plotted in solid curves, versus its approximate estimate given by values of $\int_{s_{max}}^1 \beta$ as a function of total time T, plotted in dashed curves, for different values of dephasing, α and relaxation strength, β characterized by the shown values of $s_x = s_y$ (see Eq. 2.22-2.21). Relaxation and dephasing parameters, η and η_0 are both set to $\eta = \eta_0 = 1$. There exists a region, for small values of T, over which T dependence of $\left\langle \int_s^1 \beta \right\rangle_\rho$ vanishes (panel c). This region is well captured by the approximate formula $\int_{s_{max}}^1 \beta$, however the value of $\left\langle \int_s^1 \beta \right\rangle_\rho$ itself is underestimated by the formula. For large values of T, $\left\langle \int_s^1 \beta \right\rangle_\rho$ values tend to oscillate, however, the average slope is again well captured by the approximate formula $\int_{s_{max}}^1 \beta$ (panel b).
(Panels d and e) Plot of $1 - s_{max}$ as a function of $\log T$ (bottom right panel) and the same plot in log-log scale is shown in bottom left panel. Notice that T independent region of $\left\langle \int_s^1 \beta \right\rangle_\rho$ corresponds to $s_{max} \approx 0.5$. This region ends in a kink beyond which $1 - s_{max}$ decreases zero, asymptotically approaching $\frac{1}{\log T}$. This asymptotic dependence is verified by the log-log plot in the panel e.

to be governed by a single parameter. Using Eq. C.10,

$$\begin{aligned}\mathcal{E}(T) &= f(1)\int_0^1 (\dot{f^{-1}})e^{-4T\int_s^1\beta}ds \\ &\approx -\frac{1}{T}\int_0^1 \dot{f}_0 e^{-4T\int_s^1\beta}ds. \end{aligned} \tag{C.11}$$

Taking the derivative of $\log(\mathcal{E})$with respect to T, (let $'$ denotes derivative with respect to scaled time parameter s),

$$\frac{d}{dT}\log(\mathcal{E}) \approx -\frac{1}{T} - \frac{4\int_0^1 ds\dot{f}_0 e^{-4T\int_s^1\beta}\int_s^1\beta}{\int_0^1 ds\dot{f}_0 e^{-4T\int_s^1\beta}}. \tag{C.12}$$

Defining,

$$\rho \equiv \frac{\dot{f}_0 e^{-4T\int_s^1\beta}}{\int_0^1 \dot{f}_0 e^{-4T\int_s^1\beta}} \tag{C.13}$$

as a probability density defined over $[0,1]$, the second term in the equation above is interpreted as

$$\left\langle 4\int_s^1 \beta\right\rangle_\rho \equiv \frac{4\int_0^1 ds\dot{f}_0 e^{-4T\int_s^1\beta}\int_s^1\beta}{\int_0^1 ds\dot{f}_0 e^{-4T\int_s^1\beta}}. \tag{C.14}$$

The function $f_0'(s) = -\frac{(\alpha-\beta)\omega^2}{2(1+(\alpha-\beta)^2)}$ (Eq. C.9), is symmetric about $s = 0.5$ (when $s_x = s_y$) and exponentially goes to zero at $s = 1$, while, the function $e^{-4T\int_s^1\beta}$ is an increasing function over $[0,1]$ where, it decreases exponentially from the value 1 at $s = 1$ to the value $e^{-4T\int_0^1\beta}$ at $s = 0$ with exponent being proportional to T. These properties imply that ρ is a sharply peaked (see Fig. C.2a) distribution for large T (defining large T when $1/T \ll \int_0^1\beta$ holds) with the maximum value $\rho_{max} = \rho(s_{max})$ for $s_{max} \in \big(0.5, 1\big)$. Moreover, $s_{max} \to 1$ as $T \to \infty$. Hence for large value of T, we approximate (see

Fig. C.2),

$$\left\langle \int_s^1 \beta \right\rangle_\rho \simeq \int_{s_{max}}^1 \beta. \tag{C.15}$$

s_{max} is the solution to the equation $\rho'(s)|_{s_{max}} = 0$,

$$0 = \frac{\Omega'}{\Omega} + 2\frac{\omega'}{\omega} + 4T\beta\bigg|_{s_{max}} \tag{C.16}$$

where, we defined $\Omega \equiv \frac{(\alpha-\beta)}{2(1+(\alpha-\beta)^2)}$ and $\omega = \dot{\theta}$ (see Eq. 2.5) for brevity. Since $\Omega(s \to 1) \neq 0$ and $\Omega'(s \to 1) = 0$, we conclude $\left|\frac{\Omega'}{\Omega}\right| \ll \left|\frac{\omega'}{\omega} = -\frac{2s-1}{s^2(1-s)^2}\right|$ for $s \to 1$. Thus, neglecting $\frac{\Omega'}{\Omega}$ term in the Eq. C.16, the equation for s_{max} in the $T \to \infty$ limit is given by

$$\frac{2s_{max} - 1}{4T} \simeq \frac{1}{2}s_{max}^2(1 - s_{max})^2\beta(s_{max}). \tag{C.17}$$

This result immediately leads to two conclusions. First, using the asymptotic form of β,

$$\beta \overset{s\to 1}{\simeq} \eta \left(\frac{\pi}{4C}\right)^2 (s_x^2 + s_y^2)s^4(1-s)^4 e^{-\frac{2}{1-s}}, \tag{C.18}$$

where $C \equiv \int_0^1 ds' e^{-1/s'(1-s')}$, one finds $\log(T) \sim \frac{2}{1-s_{max}} + O(\log(1 - s_{max}))$, and thus,

$$s_{max} \sim 1 - \frac{2}{\log(T)}. \tag{C.19}$$

Second, using asymptotic dependence of $\int_s^1 \beta$ on s given by,

$$\int_s^1 \beta ds \overset{s\to 1}{\simeq} \frac{1}{2}s^2(1-s)^2\beta(s). \tag{C.20}$$

Taken together with Eq. C.17, we get

$$\frac{2s_{max}-1}{4T} \simeq \int_{s_{max}}^{1} \beta ds. \tag{C.21}$$

Thus,

$$\begin{aligned}\frac{\dot{\mathcal{E}}}{\mathcal{E}} &\approx -\frac{1}{T} - \left\langle 4\int_{s}^{1} \beta ds \right\rangle \\ &\simeq -\frac{1}{T} - 4\int_{s_{max}}^{1} \beta ds \\ &\simeq -\frac{2s_{max}}{T}. \end{aligned} \tag{C.22}$$

In conclusion, $\|R(1) - R_0(1)\|$ is given by

$$\|R(1) - R_0(1)\| \sim T^{-2s_{max}}. \tag{C.23}$$

Defining the exponent at time T as

$$m(T) \equiv -2s_{max} \sim -2 + \frac{4}{\log T}, \tag{C.24}$$

where we have used the asymptotic dependence of s_{max} on T (see Eq. C.19). Since $s_{max}(T) \in (0.5, 1)$, the exponent $m(T) \in (1, 2)$ with $m(T \to \infty) = 2$. All assumptions leading upto this result are verified against exact numerical results in Fig. C.2.

Appendix D: Tunneling conductance and topological visibility from S-matrix

Tunneling conductance is a local measurement at the normal lead -superconducting nanowire (see Fig. 1.4) junction, and one may calculate it theoretically by assuming both the lead and nanowire to extend semi-infinitely and coupled together at the so-called Normal metal-Superconductor (NS) junction via a tunnel barrier.

The knowledge of the reflection matrix at the NS junction is sufficient to calculate the tunneling conductance. The reflection matrix has the form

$$r = \begin{pmatrix} r_{ee} & r_{eh} \\ r_{he} & r_{hh} \end{pmatrix}, \tag{D.1}$$

where r_{ee} and r_{eh} are the normal and Andreev reflection amplitudes, respectively. Here, the reflection matrix is expressed in the basis of electron and hole scattering channels, which is called the particle-hole basis. Such a convenient decomposition in normal and Andreev reflection amplitudes is possible whenever the lead Hamiltonian, H_{lead} (see Eq. (3.7)) is diagonal in the particle hole basis- i.e. $[H_{\text{lead}}, \tau_z] = 0$. For a single conducting channel, the tunneling conductance to a superconductor in the NS junction is given by the Blonder-Tinkham-Klapwijk (BTK) formula [24] (in the units of e^2/h)

$$G = 1 - |r_{ee}|^2 + |r_{eh}|^2. \tag{D.2}$$

With N conducting modes in the lead, r_{ee} and r_{eh} acquire a matrix structure and the BTK formula is generalized to,

$$G = N - \mathrm{Tr}(r_{ee}r_{ee}^{\dagger} - r_{eh}r_{eh}^{\dagger})$$

For a periodic translationally invariant spinless *p*-wave superconductor described by a Hamiltonian $H(k)$ in *k*-space, Kitaev [4] defined the TI as

$$Q_{\mathrm{Kitaev}} = \mathrm{sgn}(\mathrm{Pf}(iH(0))\mathrm{Pf}(iH(\pi))), \tag{D.3}$$

where Pf denotes Pfaffian operation on a matrix. Q_{Kitaev} is completely equivalent TI introduced in the Eq. 1.19 when calculated for 1-D spinless p-wave superconductor. superconductor in the introduction is $Q_{\mathrm{Kitaev}} = -1$ implies that the system is in a topological phase i.e. if the same Hamiltonian were to describe a finite chain with an open boundary condition, the system edges will host non-Abelian Majorana zero modes. For an open finite wire geometry, Akhmerov *et. al.* [25] provided the following generalization for the TI in terms of the reflection matrix:

$$Q_0 = \mathrm{sgn}(\det(r)). \tag{D.4}$$

It was argued in the main body of the chapter that in presence of dissipation, a more useful quantity to characterize topological properties of the system is TV– a quantity closely related to scattering matrix TI (D.4), defined as

$$Q = \det(r). \tag{D.5}$$

To justify this expression for the TV, which we use in our numerical work, consider the particle-hole symmetry of the superconducting Bogoliubov-de Gennes (BdG) Hamiltonian i.e.,

$$\Pi H_{\mathrm{BdG}} \Pi^{-1} = -H_{\mathrm{BdG}}, \tag{D.6}$$

where $\Pi = \tau_x C$ with C being the complex conjugation operator. This leads to the following constraint on the reflection matrix,

$$\tau_x r \tau_x = r^*, \tag{D.7}$$

which implies

$$\det(r) = \det(r)^*. \tag{D.8}$$

Note that we have implicitly assumed the voltage bias, V, to be zero. For finite V, the particle-hole constraint on the voltage-dependent reflection matrix $r(V)$ takes the form $\tau_x r(V) \tau_x = r(-V)^*$. When the voltage bias is less than the superconducting gap ($eV < \Delta$), the transmission through the nanowire is zero as there are no extended states. Therefore the reflection matrix r is unitary i.e., $rr^\dagger = 1$. This implies

$$\mathrm{Tr}(r_{ee} r_{ee}^\dagger + r_{eh} r_{ee}^\dagger) = \mathrm{Tr}(r_{hh} r_{hh}^\dagger + r_{he} r_{he}^\dagger) = N \tag{D.9}$$

and that the absolute value of the determinant of reflection matrix satisfies

$$|\det(r)| = 1. \tag{D.10}$$

Combined with the particle-hole symmetry constraint of r, we get $\det(r) = \pm 1$. In other words we have shown that whenever reflection matrix r respects unitarity and particle-hole symmetry, the TI (defined as $\mathrm{sgn}(\det(r))$) is equal to TV (defined as $\det(r)$), i.e. $Q_0 = Q$. An ideal system with MZMs is characterized by $\det(r) = -1$ (and non-topological trivial phase is characterized by $\det(r) = 1$) and also is associated with quantized ZBCP at $2e^2/h$. The only way to change the value of $\det(r)$ is to break the unitarity by closing the topological gap. Note that by substituting Eq. (D.9) in Eq. (E.6) and using the unitarity of the reflection matrix one can show,

$$G = 2\mathrm{Tr}(r_{eh}r_{eh}^{\dagger}), \tag{D.11}$$

$$\mathrm{Tr}(r_{eh}r_{eh}^{\dagger}) = \mathrm{Tr}(r_{he}r_{he}^{\dagger}). \tag{D.12}$$

Moreover, particle-hole symmetry of r implies

$$r_{eh}(V) = r_{he}^{\dagger}(-V). \tag{D.13}$$

Finally, using Eqs. (D.13) and (D.12) we arrive at

$$G(V) = G(-V). \tag{D.14}$$

So the unitarity and particle-hole symmetry of r guarantee that the in-gap conductance is symmetric about zero bias. For a finite system, any MZM would be split in energy by δ because of the inevitable MZM overlap from the two ends (which could be exponentially small, but never zero for a finite wire). Strictly at zero energy there would be no BdG eigenstate in the nanowire rendering an incoming electron to be totally reflected with $\det(r) = 1$. We would infer, based on this argument, that all finite systems irrespective of whether they host MZMs or not are non-topological. This is similar to the statement in an entirely different context that no finite system can have a phase transition, which is only a property of the infinite volume thermodynamic limit. In reality, other (nonuniversal) cut-offs in energy and length scales of the problem become important as the system size increases, and eventually finite and infinite systems behave in the same manner. For the nanowire MZM problem, this arises from the energy broadening inherent in any realistic system, which renders the split hybridized nonzero energy peaks into a broadened midgap peak with a finite weight at zero energy. Thus, the split resonances at sharp nonzero energies become a broad peak around zero energy with a finite width. Without such a dissipative broadening process, the splitting of the MZMs invariably present in any real system with finite wire length will always lead to precisely zero conductance at zero energy since the MZMs are now always shifted from zero energy due to Majorana splitting.

We account for finite lifetime of the quasiparticle due to various inelastic scattering mechanisms such as phonons and magnetic moments through an onsite imaginary term in the Hamiltonian. We emphasize that without this broadening, a finite wire can never have a true zero energy mode, and the system is by definition always in the trivial phase! The resultant broadening due to the onsite imaginary term in the Hamiltonian is given by Γ.

Appendix E: S matrix in Majorana representation

The S-matrix of the nanowire can be written in terms of reflection and transmission matrices as

$$S = \begin{pmatrix} r & t' \\ t & r' \end{pmatrix} \tag{E.1}$$

where, r, r' are $2N \times 2N$ reflection matrices at the two wire ends and t, t' are transmission $2N \times 2N$ matrices for N conducting channels in the nanowire. The system Hamiltonian 4.4 endows particle-hole symmetry to the S matrix of the system, which at zero-bias reads

$$\begin{gathered} \tau_x S \tau_x = S^* \\ \tau_x \begin{pmatrix} r & t' \\ t & r' \end{pmatrix} \tau_x = \begin{pmatrix} r^* & t'^* \\ t^* & r'^* \end{pmatrix} \end{gathered} \tag{E.2}$$

Specifically, the reflection matrix obeys the constraint

$$\tau_x r \tau_x = r^*. \tag{E.3}$$

Particle-hole symmetric reflection matrix r can be expanded into conventional and Andreev reflection amplitudes,

$$r = \begin{pmatrix} r_{ee} & r_{eh} \\ r_{he} & r_{hh} \end{pmatrix}. \tag{E.4}$$

Such a representation is said to be in *particle-hole* basis. For brevity we label r as r_{ph} whenever it is expressed in particle-hole representation. The particle-hole symmetry relates particle and hole components of r_{ph}, $r_{ee} = r^*_{hh}$ and $r_{eh} = r^*_{he}$.

Tunneling conductance through a single channel normal lead-superconductor junction in given by Blonder-Tinkham-Klapwijk (BTK) formula [24] (in the units of e^2/h)

$$G = 1 - |r_{ee}|^2 + |r_{eh}|^2. \tag{E.5}$$

Generalizing BTK conductance formula (Eq. (E.5)) for multichannel transport, we arrive at

$$\begin{aligned} G &= N - \mathrm{Tr}[r_{ee}r^\dagger_{ee} - r_{eh}r^\dagger_{eh}] \\ &= N - \mathrm{Tr}[r\tau_z r^\dagger \tau_z]. \end{aligned} \tag{E.6}$$

One can perform an unitary transformation on reflection and transmission matrices

$$r_{maj} = U r_{ph} U^\dagger \tag{E.7}$$

such that $r_{maj} = r^*_{maj}$. This real representation of S matrix is called majorana representation. The U is given by

$$U = \begin{pmatrix} -i & i \\ 1 & 1 \end{pmatrix}. \tag{E.8}$$

In majorana representation the expression for the conductance becomes

$$G = N - \mathrm{Tr}[r_{maj}\tau_y r^\dagger_{maj}\tau_y]. \tag{E.9}$$

E.1 Polar decomposition of S-matrix and S-matrix of the composite system

Let S_{sys} be the S-matrix of a class D [51, 54] system at zero energy. Then, S_{sys} admits a polar decomposition, [80]

$$S_{sys} = \begin{pmatrix} O_1 & 0 \\ 0 & O_2 \end{pmatrix} \begin{pmatrix} \tanh\Lambda & \cosh\Lambda^{-1} \\ \cosh\Lambda^{-1} & -\tanh\Lambda \end{pmatrix} \begin{pmatrix} O_3 & 0 \\ 0 & O_4 \end{pmatrix} \tag{E.10}$$

where $O_i \in \mathrm{SO(2N)}$ with N being the number of conducting electron channels in the lead at zero energy and Λ is a real diagonal $2\mathrm{N} \times 2\mathrm{N}$ matrix. Comparing it to Eq. E.1, the reflection and the transmission matrices can be read off as,

$$\begin{aligned} r &= O_1 \tanh\Lambda O_3 \\ r' &= -O_2 \tanh\Lambda O_4 \\ t &= O_2 \cosh\Lambda^{-1} O_3 \\ t' &= O_1 \cosh\Lambda^{-1} O_4. \end{aligned} \tag{E.11}$$

As discussed in the main body of the chapter, our system of interest has a class D superconductor coupled to the left(right) lead through left(right) barrier. The composite S-matrix of system+barrier can evaluated in terms of transfer matrix (T-matrix) of the composite system. Let $T^L_{bar}, T^R_{bar}, T_{sys}$ denote the T-matrix of the left barrier, right barrier and the system, respectively. The composite T-matrix of the coupled system is given by,

$$T_{com} = T^L_{bar} T_{sys} T^R_{bar}. \tag{E.12}$$

Let $\begin{pmatrix} t_1 & t_2 \\ t_3 & t_4 \end{pmatrix}$ denote a generic T-matrix. Comparing the defining equations of S-matrix and the T-matrix,

$$\begin{pmatrix} R_o \\ L_o \end{pmatrix} = \begin{pmatrix} r & t' \\ t & r' \end{pmatrix} \begin{pmatrix} R_i \\ L_i \end{pmatrix}$$
$$\begin{pmatrix} L_o \\ L_i \end{pmatrix} = \begin{pmatrix} t_1 & t_2 \\ t_3 & t_4 \end{pmatrix} \begin{pmatrix} R_i \\ R_o \end{pmatrix} \tag{E.13}$$

where, $R(L)$ denote the amplitude in right(left) lead and subscripts $i(o)$ denote the incoming(out-going) modes, elements of S-matrix can be expressed in terms of T-matrix and vice-versa using,

$$t_1 = t - r't'^{-1}r; \quad t_2 = r't'^{-1}$$
$$t_3 = -t'^{-1}r; \quad t_4 = t'^{-1}$$

$$r = -t_4^{-1}t_3; \quad t' = t_4^{-1}$$
$$t = t_1 - t_2t_4^{-1}t_3; \quad r' = t_2t_4^{-1} \tag{E.14}$$

For our calculations in chapter 4 we use symmetric barrier such that $T_{bar}^L = T_{bar}^R \equiv T_{bar}$. The S-matrix of the barrier S_{bar} (which is related to T_{bar} through Eq. E.14) was chosen in a generic fashion. The particular choice for barrier S-matrix S_{bar} in the particle-hole basis used in our calculations is as follows. $S_{bar} = \begin{pmatrix} R & T \\ T & -R \end{pmatrix}$, T is assumed to be diagonal with (0.15,0.15,0.075,0.075,0.15,0.15,0.075,0.075) as its eigenvalues. The eigenvalues $r_i's$ of R are related to eigenvalues $t_i's$ of T by the relation, $r_i = \sqrt{1 - t_i^2}$.

Bibliography

[1] E. Majorana. *Nuovo Cimento*, 5:171, 1937.

[2] Steven R Elliott and Marcel Franz. Colloquium: Majorana fermions in nuclear, particle, and solid-state physics. *Reviews of Modern Physics*, 87(1):137, 2015.

[3] Palash B Pal. Dirac, majorana, and weyl fermions. *American Journal of Physics*, 79(5):485–498, 2011.

[4] A Yu Kitaev. Unpaired majorana fermions in quantum wires. *Phys. Usp.*, 44 (10S):131, 2001.

[5] N. Read and Dmitry Green. Paired states of fermions in two dimensions with breaking of parity and time-reversal symmetries and the fractional quantum hall effect. *Phys. Rev. B*, 61:10267–10297, Apr 2000.

[6] D. A. Ivanov. Non-abelian statistics of half-quantum vortices in p-wave superconductors. *Phys. Rev. Lett.*, 86:268–271, Jan 2001.

[7] N. B. Kopnin and M. M. Salomaa. Mutual friction in superfluid $^3\mathrm{He}$: Effects of bound states in the vortex core. *Phys. Rev. B*, 44:9667–9677, Nov 1991.

[8] G. E. Volovik. Fermion zero modes on vortices in chiral superconductors. *Journal of Experimental and Theoretical Physics Letters*, 70(9):609–614, 1999.

[9] K. Sengupta, Igor Žutić, Hyok-Jon Kwon, Victor M. Yakovenko, and S. Das Sarma. Midgap edge states and pairing symmetry of quasi-one-dimensional organic superconductors. *Phys. Rev. B*, 63:144531, 2001.

[10] Chetan Nayak, Steven H. Simon, Ady Stern, Michael Freedman, and S. Das Sarma. Non-abelian anyons and topological quantum computation. *Rev. Mod. Phys.*, 80:1083, 2008.

[11] Sankar Das Sarma, Michael Freedman, and Chetan Nayak. Majorana zero modes and topological quantum computation. *Npj Quantum Information*, 1:15001, Oct 2015.

[12] Jason Alicea. New directions in the pursuit of majorana fermions in solid state systems. *Reports on progress in physics*, 75(7):076501, 2012.

[13] Martin Leijnse and Karsten Flensberg. Introduction to topological superconductivity and majorana fermions. *Semiconductor Science and Technology*, 27(12): 124003, 2012.

[14] C W J Beenakker. Search for Majorana fermions in superconductors. *Annual Review of Condensed Matter Physics*, 4, 2013. URL `https://arxiv.org/pdf/1112.1950.pdf`.

[15] B Van Heck, AR Akhmerov, F Hassler, M Burrello, and CWJ Beenakker. Coulomb-assisted braiding of majorana fermions in a josephson junction array. *New Journal of Physics*, 14(3):035019, 2012.

[16] Jay D Sau, David J Clarke, and Sumanta Tewari. Controlling non-abelian statistics of majorana fermions in semiconductor nanowires. *Physical Review B*, 84 (9):094505, 2011.

[17] Jason Alicea, Yuval Oreg, Gil Refael, Felix Von Oppen, and Matthew PA Fisher. Non-abelian statistics and topological quantum information processing in 1d wire networks. *Nature Physics*, 7(5):412, 2011.

[18] Bauer, Bela and Karzig, Torsten and Mishmash, Ryan V. and Antipov, Andrey E. and Alicea, Jason. Dynamics of Majorana-based qubits operated with an array of tunable gates. *arXiv:1803.05451*, 2018.

[19] Torsten Karzig, Yuval Oreg, Gil Refael, and Michael H Freedman. Universal geometric path to a robust majorana magic gate. *Physical Review X*, 6(3):031019, 2016.

[20] Karsten Flensberg. Tunneling characteristics of a chain of majorana bound states. *Physical Review B*, 82(18):180516, 2010.

[21] K T Law, Patrick A Lee, and T K Ng. Majorana fermion induced resonant andreev reflection. *Phys. Rev. Lett.*, 103(23):237001, 2009.

[22] Michael Wimmer, A R Akhmerov, J P Dahlhaus, and C W J Beenakker. Quantum point contact as a probe of a topological superconductor. *New Journal of Physics*, 13(5):053016, 2011.

[23] Jay D. Sau F. Setiawan, P. M. R. Brydon and Sankar Das Sarma. Conductance spectroscopy of topological superconductor wire junctions. *Phys. Rev. B*, 91(21): 214513, 2015.

[24] G E Blonder, M Tinkham, and T M Klapwijk. Transition from metallic to tunneling regimes in superconducting microconstrictions: Excess current, charge imbalance, and supercurrent conversion. *Phys. Rev. B*, 25(7):4515, 1982.

[25] A. R. Akhmerov, J. P. Dahlhaus, F. Hassler, M. Wimmer, and C. W. J. Beenakker. Quantized conductance at the majorana phase transition in a disordered superconducting wire. *Phys. Rev. Lett*, 106:057001, 2011.

[26] Roman M. Lutchyn, Jay D. Sau, and Sankar Das Sarma. Majorana fermions and a topological phase transition in semiconductor-superconductor heterostructures. *Phys. Rev. Lett.*, 105:077001, 2010.

[27] Jay D. Sau, Roman M. Lutchyn, Sumanta Tewari, and Sankar Das Sarma. Generic new platform for topological quantum computation using semiconductor heterostructures. *Phys. Rev. Lett.*, 104:040502, 2010.

[28] Jason Alicea. Majorana fermions in a tunable semiconductor device. *Phys. Rev. B*, 81:125318, 2010.

[29] Yuval Oreg, Gil Refael and Felix von Oppen. Helical liquids and majorana bound states in quantum wires. *Phys. Rev. Lett.*, 105:177002, 2010.

[30] Tudor D Stanescu and Sumanta Tewari. Majorana fermions in semiconductor nanowires: fundamentals, modeling, and experiment. *Journal of Physics: Condensed Matter*, 25(23):233201, 2013.

[31] V. Mourik, K. Zuo, S. M. Frolov, S. R. Plissard, E. P. A. M. Bakkers and L. P. Kouwenhoven. Signatures of majorana fermions in hybrid superconductor-semiconductor nanowire devices. *Science*, 336:1003, 2012.

[32] Leonid P Rokhinson, Xinyu Liu, and Jacek K Furdyna. The fractional ac josephson effect in a semiconductor-superconductor nanowire as a signature of majorana particles. *Nat. Phys.*, 8:795, 2012.

[33] M. T. Deng, C. L. Yu, G. Y. Huang, M. Larsson, P. Caroff, and H. Q. Xu. Anomalous zero-bias conductance peak in a nbinsb nanowirenb hybrid device. *Nano Lett.*, 12:6414, 2012.

[34] Anindya Das, Yuval Ronen, Yonatan Most, Yuval Oreg, Moty Heiblum and Hadas Shtrikman. Zero-bias peaks and splitting in an al-inas nanowire topological superconductor as a signature of majorana fermions. *Nat. Phys.*, 8:887, 2012.

[35] H. O. H. Churchill, V. Fatemi, K. Grove-Rasmussen, M. T. Deng, P. Caroff, H. Q. Xu, and C. M. Marcus. Superconductor-nanowire devices from tunneling to the multichannel regime: Zero-bias oscillations and magnetoconductance crossover. *Phys. Rev. B*, 87:241401, 2013.

[36] Hao Zhang, Önder Gül, Sonia Conesa-Boj, Michał P Nowak, Michael Wimmer, Kun Zuo, Vincent Mourik, Folkert K De Vries, Jasper Van Veen, Michiel WA De Moor, et al. Ballistic superconductivity in semiconductor nanowires. *Nature communications*, 8:16025, 2017.

[37] MT Deng, S Vaitiekėnas, Esben Bork Hansen, Jeroen Danon, M Leijnse, Karsten Flensberg, Jesper Nygård, P Krogstrup, and Charles M Marcus. Majorana bound state in a coupled quantum-dot hybrid-nanowire system. *Science*, 354(6319): 1557–1562, 2016.

[38] Jun Chen, Peng Yu, John Stenger, Moïra Hocevar, Diana Car, Sébastien R Plissard, Erik PAM Bakkers, Tudor D Stanescu, and Sergey M Frolov. Experimental phase diagram of a one-dimensional topological superconductor. *arXiv preprint arXiv:1610.04555*, 2016.

[39] Tudor D Stanescu, Roman M Lutchyn, and S Das Sarma. Soft superconducting gap in semiconductor-based majorana nanowires. *Physical Review B*, 90(8): 085302, 2014.

[40] Jay D Sau and S Das Sarma. Density of states of disordered topological superconductor-semiconductor hybrid nanowires. *Physical Review B*, 88(6): 064506, 2013.

[41] Chun-Xiao Liu, Jay D Sau, and S Das Sarma. Role of dissipation in realistic majorana nanowires. *Physical Review B*, 95(5):054502, 2017.

[42] So Takei, Benjamin M Fregoso, Hoi-Yin Hui, Alejandro M Lobos, and S Das Sarma. Soft superconducting gap in semiconductor majorana nanowires. *Physical review letters*, 110(18):186803, 2013.

[43] Chien-Hung Lin, Jay D Sau, and S Das Sarma. Zero-bias conductance peak in majorana wires made of semiconductor/superconductor hybrid structures. *Physical Review B*, 86(22):224511, 2012.

[44] Philip W Anderson. Theory of dirty superconductors. *Journal of Physics and Chemistry of Solids*, 11(1-2):26–30, 1959.

[45] Eduardo J. H. Lee, Xiaocheng Jiang, Manuel Houzet, Ramon Aguado, Charles M. Lieber, and Silvano De Franceschi. Spin-resolved andreev levels and parity crossings in hybrid superconductor-semiconductor nanostructures. *Nat Nano*, 9: 79, 2013.

[46] G. Kells, D. Meidan, and P. W. Brouwer. Low-energy subgap states in multichannel p-wave superconducting wires. *Phys. Rev. B*, 85:060507, 2012.

[47] Falko Pientka, Graham Kells, Alessandro Romito, Piet W. Brouwer and Felix von Oppen. Enhanced zero-bias majorana peak in the differential tunneling conductance of disordered multisubband quantum wire/superconductor junctions. *Phys. Rev. Lett.*, 109:227006, 2012.

[48] Jie Liu, Andrew C. Potter, K. T. Law, and Patrick A. Lee. Zero-bias peaks in the tunneling conductance of spin-orbit-coupled superconducting wires with and without majorana end-states. *Phys. Rev. Lett.*, 109:267002, 2012.

[49] Dmitry Bagrets and Alexander Altland. Class d spectral peak in majorana quantum wires. *Phys. Rev. Lett.*, 109:227005, 2012.

[50] Patrick Neven, Dmitry Bagrets, and Alexander Altland. Quasiclassicaltheory of disordered multi-channel majorana quantum wires. *New J. Phys.*, 15:055019, 2013.

[51] Alexander Altland and Martin R. Zirnbauer. Nonstandard symmetry classes in mesoscopic normal-superconducting hybrid structures. *Phys. Rev. B*, 55:1142, 1997.

[52] B. J. van Wees, P. de Vries, P. Magnée, and T. M. Klapwijk. Excess conductance of superconductor-semiconductor interfaces due to phase conjugation between electrons and holes. *Phys. Rev. Lett.*, 69:510, 1992.

[53] D I Pikulin, J P Dahlhaus, M Wimmer, H Schomerus, and C W J Beenakker. A zero-voltage conductance peak from weak antilocalization in a majorana nanowire. *New J. Phys.*, 14:125011, 2012.

[54] Andreas P Schnyder, Shinsei Ryu, Akira Furusaki, and Andreas WW Ludwig. Classification of topological insulators and superconductors in three spatial dimensions. *Physical Review B*, 78(19):195125, 2008.

[55] S. Mi, D. I. Pikulin, M. Marciani, and C. W. J. Beenakker. X-shaped and Y-shaped andreev resonance profiles in a superconducting quantum dot. *ArXiv e-prints*, 2014.

[56] İnanç Adagideli, Michael Wimmer, and Aykut Teker. Effects of electron scattering on the topological properties of nanowires: Majorana fermions from disorder and superlattices. *Phys. Rev. B*, 89(14):144506, 2014.

[57] Piet W Brouwer, Mathias Duckheim, Alessandro Romito, and Felix von Oppen. Topological superconducting phases in disordered quantum wires with strong spin-orbit coupling. *Phys. Rev. B*, 84(14):144526, 2011.

[58] Elsa Prada, Pablo San-Jose, and Ramón Aguado. Transport spectroscopy of n s nanowire junctions with majorana fermions. *Phys. Rev. B*, 86(18):180503, 2012.

[59] Meng Cheng, Victor Galitski, and S Das Sarma. Nonadiabatic effects in the braiding of non-abelian anyons in topological superconductors. *Physical Review B*, 84(10):104529, 2011.

[60] Torsten Karzig, Gil Refael, and Felix von Oppen. Boosting majorana zero modes. *Physical Review X*, 3(4):041017, 2013.

[61] Mathias S Scheurer and Alexander Shnirman. Nonadiabatic processes in majorana qubit systems. *Physical Review B*, 88(6):064515, 2013.

[62] Christina Knapp, Michael Zaletel, Dong E Liu, Meng Cheng, Parsa Bonderson, and Chetan Nayak. The nature and correction of diabatic errors in anyon braiding. *Physical Review X*, 6(4):041003, 2016.

[63] Fabio L Pedrocchi and David P DiVincenzo. Majorana braiding with thermal noise. *Physical review letters*, 115(12):120402, 2015.

[64] Meng Cheng, Roman M Lutchyn, and S Das Sarma. Topological protection of majorana qubits. *Physical Review B*, 85(16):165124, 2012.

[65] Garry Goldstein and Claudio Chamon. Decay rates for topological memories encoded with majorana fermions. *Physical Review B*, 84(20):205109, 2011.

[66] Diego Rainis and Daniel Loss. Majorana qubit decoherence by quasiparticle poisoning. *Physical Review B*, 85(17):174533, 2012.

[67] François Konschelle and Fabian Hassler. Effects of nonequilibrium noise on a quantum memory encoded in majorana zero modes. *Physical Review B*, 88(7): 075431, 2013.

[68] Fabio L Pedrocchi, N.E. Bonesteel, and David P DiVincenzo. Monte carlo studies of the self-correcting properties of the majorana quantum error correction code under braiding. *Physical Review B*, 92:120402, 2015.

[69] Andrew M Childs, Edward Farhi, and John Preskill. Robustness of adiabatic quantum computation. *Physical Review A*, 65(1):012322, 2001.

[70] Wang Yao, Ren-Bao Liu, and LJ Sham. Restoring coherence lost to a slow interacting mesoscopic spin bath. *Physical review letters*, 98(7):077602, 2007.

[71] Anthony J Leggett, Sudip Chakravarty, AT Dorsey, Matthew PA Fisher, Anupam Garg, and W Zwerger. Dynamics of the dissipative two-state system. *Reviews of Modern Physics*, 59(1):1, 1987.

[72] Ulrich Weiss. *Quantum dissipative systems*, volume 13. World scientific, 2012.

[73] E Brian Davies. Markovian master equations commun. *Math. Phys*, 39:91–110, 1974.

[74] Heinz-Peter Breuer and Francesco Petruccione. *The theory of open quantum systems*. Oxford University Press on Demand, 2002.

[75] John Preskill. Lecture notes for physics 219: Quantum computation. *Lecture notes for Physics 219: Quantum computation*, 1999.

[76] George A Hagedorn and Alain Joye. Elementary exponential error estimates for the adiabatic approximation. *Journal of mathematical analysis and applications*, 267(1):235–246, 2002.

[77] Jay D Sau, Sumanta Tewari, and S Das Sarma. Universal quantum computation in a semiconductor quantum wire network. *Physical Review A*, 82(5):052322, 2010.

[78] T Hyart, B Van Heck, IC Fulga, M Burrello, AR Akhmerov, and CWJ Beenakker. Flux-controlled quantum computation with majorana fermions. *Physical Review B*, 88(3):035121, 2013.

[79] David J Clarke, Jay D Sau, and Sankar Das Sarma. A practical phase gate for producing bell violations in majorana wires. *Physical Review X*, 6(2):021005, 2016.

[80] I. C. Fulga, F. Hassler, A. R. Akhmerov and C. W. J. Beenakker . Scattering formula for the topological quantum number of a disordered multimode wire. *Phys. Rev. B*, 83:155429, 2011.

[81] D I Pikulin and Yu V Nazarov. Topological properties of superconducting junctions. *JETP letters*, 94(9):693–697, 2012.

[82] A. D. K. Finck, D. J. Van Harlingen, P. K. Mohseni, K. Jung, and X. Li. Anomalous modulation of a Zero-Bias peak in a hybrid Nanowire-Superconductor device. *Phys. Rev. Lett*, 110:126406, 2013.

[83] W. Chang, S. M. Albrecht, T. S. Jespersen, F. Kuemmeth, P. Krogstrup, J. Nygrd and C. M. Marcus. Hard gap in epitaxial semiconductorsuperconductor nanowires. *Nature Nanotechnology*, 10:232, 2015.

[84] Christoph W Groth, Michael Wimmer, Anton R Akhmerov, and Xavier Waintal. Kwant: a software package for quantum transport. *New Journal of Physics*, 16 (6):063065, 2014.

[85] Meng Cheng, Roman M. Lutchyn, Victor Galitski and S. Das Sarma. Splitting of Majorana modes due to intervortex tunneling in a p + ip superconductor. *Phys. Rev. Lett.*, 103:107001, 2009.

[86] Meng Cheng, Roman M. Lutchyn, Victor Galitski, S. Das Sarma. Tunneling of anyonic Majorana excitations in topological superconductors. *Phys. Rev. B*, 82: 094504, 2010.

[87] S. Das Sarma, Jay D Sau and Tudor D Stanescu. Splitting of the zero-bias conductance peak as smoking gun evidence for the existence of the majorana mode in a superconductor-semiconductor nanowire. *Phys. Rev. B*, 86:220506, 2012.

[88] Diego Rainis, Luka Trifunovic, Jelena Klinovaja and Daniel Loss. Towards a realistic transport modeling in a superconducting nanowire with majorana fermions. *Phys. Rev. B*, 87:024515, 2013.

[89] Subir Sachdev. *Quantum phase transitions*. Cambridge University Press, 2011.

[90] Olexei Motrunich, Kedar Damle, and David A. Huse. Griffiths effects and quantum critical points in dirty superconductors without spin-rotation invariance: One-dimensional examples. *Phys. Rev. B.*, 63:224204, 2001.

[91] Supriyo Datta. *Electronic transport in mesoscopic systems*. Cambridge university press, 1997.

[92] Jay D Sau, Sumanta Tewari, and S Das Sarma. Probing non-abelian statistics with majorana fermion interferometry in spin-orbit-coupled semiconductors. *Phys. Rev. B*, 84(8):085109, 2011.

[93] David J Clarke, Jay D Sau, and Sumanta Tewari. Majorana fermion exchange in quasi-one-dimensional networks. *Phys. Rev. B*, 84(3):035120, 2011.

[94] Cássio Sozinho Amorim, Kazuto Ebihara, Ai Yamakage, Yukio Tanaka, and Masatoshi Sato. Majorana braiding dynamics in nanowires. *Phys. Rev. B*, 91 (17):174305, 2015.

[95] Qi-Feng Liang, Zhi Wang, and Xiao Hu. Manipulation of majorana fermions by point-like gate voltage in the vortex state of a topological superconductor. *EPL (Europhysics Letters)*, 99(5):50004, 2012.

[96] Alessandro Romito, Jason Alicea, Gil Refael, and Felix von Oppen. Manipulating majorana fermions using supercurrents. *Physical Review B*, 85(2):020502, 2012.

[97] Bertrand I Halperin, Yuval Oreg, Ady Stern, Gil Refael, Jason Alicea, and Felix von Oppen. Adiabatic manipulations of majorana fermions in a three-dimensional network of quantum wires. *Physical Review B*, 85(14):144501, 2012.

[98] Panagiotis Kotetes, Gerd Schön, and Alexander Shnirman. Engineering and manipulating topological qubits in 1d quantum wires. *Journal of the Korean Physical Society*, 62(10):1558–1563, 2013.

[99] David J Clarke, Jay D Sau, and S Das Sarma. Bell violations in majorana wires. *arXiv preprint arXiv:1510.00007*, 2015.

[100] Xiong-Jun Liu and Alejandro M Lobos. Manipulating majorana fermions in quantum nanowires with broken inversion symmetry. *Phys. Rev. B*, 87(6): 060504, 2013.

[101] Ching-Kai Chiu, MM Vazifeh, and M Franz. Majorana fermion exchange in strictly one-dimensional structures. *EPL (Europhysics Letters)*, 110(1):10001, 2015.

[102] A.R. Akhmerov, Johan Nilson and C.W.J. Beenakker. Electrically detected interferometry of majorana fermions in a topological insulator. *Phys. Rev. Lett*, 102: 216404, 2009.

[103] Benjamin M. Fregoso, Alejandro M. Lobos, and S. Das Sarma. Electrical detection of topological quantum phase transitions in disordered majorana nanowires. *Phys. Rev. B*, 88:180507, 2013.

[104] Sumanta Tewari, J. D. Sau, V. W. Scarola, Chuanwei Zhang, and S. Das Sarma. Probing a topological quantum critical point in semiconductor-superconductor heterostructures. *Phys. Rev. B*, 85:155302, 2012.

[105] S Das Sarma, Amit Nag, and Jay D Sau. How to infer non-abelian statistics and topological visibility from tunneling conductance properties of realistic majorana nanowires. *Physical Review B*, 94(3):035143, 2016.

[106] Roman M Lutchyn, Tudor D Stanescu, and S Das Sarma. Search for majorana fermions in multiband semiconducting nanowires. *Physical review letters*, 106 (12):127001, 2011.

[107] Andrew C Potter and Patrick A Lee. Multichannel generalization of kitaevs majorana end states and a practical route to realize them in thin films. *Physical review letters*, 105(22):227003, 2010.

[108] Sumanta Tewari and Jay D Sau. Topological invariants for spin-orbit coupled superconductor nanowires. *Physical review letters*, 109(15):150408, 2012.

[109] S.Nadj-Perge, V.S. Pribiag, J.W.G. van den Berg, K. Zuo, S. R. Plissard, E. P. A. M. Bakkers, S. M. Frolov and L. P. Kouwenhoven. Spectroscopy of spin-orbit quantum bits in indium antimonide nanowires. *Phys. Rev. Lett.*, 108:166801, 2012.

[110] Piet W. Brouwer, Mathias Duckheim, Alessandro Romito, and Felix von Oppen. Probability distribution of majorana end-state energies in disordered wires. *Phys. Rev. Lett.*, 107:196804, 2011.

[111] R.L. Willet. The quantum hall effect at 5/2 filling factor. *Reports on Progress in Physics*, 76(7):076501, 2013.

[112] William S Cole, Jay D Sau, and S Das Sarma. Proximity effect and majorana bound states in clean semiconductor nanowires coupled to disordered superconductors. *Physical Review B*, 94(14):140505, 2016.

[113] Tudor D Stanescu, Roman M Lutchyn, and S Das Sarma. Majorana fermions in semiconductor nanowires. *Physical Review B*, 84(14):144522, 2011.

[114] Jean Dalibard, Yvan Castin, and Klaus Mølmer. Wave-function approach to dissipative processes in quantum optics. *Physical review letters*, 68(5):580, 1992.

[115] Howard Carmichael. *An open systems approach to quantum optics: lectures presented at the Université Libre de Bruxelles, October 28 to November 4, 1991*, volume 18. Springer Science & Business Media, 2009.